UNIVERSITY OF OKLAHOMA

GRADUATE COLLEGE

ELECTRON TRANSPORT IN MESOSCOPIC DEVICES FABRICATED FROM InSb/$Al_xIn_{1-x}Sb$ HETEROSTRUCTURES GROWN BY MOLECULAR BEAM EPITAXY

A Dissertation

SUBMITTED TO THE GRADUATE FACULTY

in partial fulfillment of the requirements for the

degree of

Doctor of Philosophy

By

NITI GOEL
Norman, Oklahoma

2004

ELECTRON TRANSPORT IN MESOSCOPIC DEVICES FABRICATED FROM InSb/$Al_xIn_{1-x}Sb$ HETEROSTRUCTURES GROWN BY MOLECULAR BEAM EPITAXY

A Dissertation APPROVED FOR THE DEPARTMENT OF PHYSICS AND ASTRONOMY

BY

Michael Santos (chair)

Matthew Johnson

Bruce Mason

Gregory Parker

Zhisheng Shi

To my parents

ACKNOWLEDGEMENTS

I would like to express my sincere gratitude to my thesis advisor, Dr. M.B. Santos, who guided and helped me in shaping my research project. I value his suggestions, comments and questions. I am grateful to him for providing me the opportunity to advertise my work in various conferences and to interact with the scientists from all around the world.

Thanks to all the committee members Dr. M.B. Johnson, Dr. Z. Shi, Dr. B. Mason and Dr. G.A. Parker for valuable guidance and insightful inputs in completing this thesis. The growth of samples for experiments in this thesis would not have been possible without the help of Joel Keay. I am grateful for his help and guidance in the maintenance of and work on all the parts and equipments in MBE lab and for providing AFM images. I also thank him for being an understanding and patient friend. Special thanks to Seokjae Chung for the initial training and guidance in MBE system.

I would like to acknowledge Dr. Y. Hirayama, Dr. K. Suzuki and Mr. S. Miyashita of NTT Basic Research Laboratories, Japan, for allowing me to use the research facility and for helping me with device fabrication and magneto-transport experiments. I would like to thank Dr. S.Q. Murphy for allowing me to use her laboratory and for helping me with experiments on the low temperature magneto-transport measurements on the quantum point contacts of the second type of geometry. Thanks to all the faculty members in the condensed matter physics group in our department.

I would like to thank Charles Kelley for help with the maintenance of equipments, post docs Tetsuya Mishima for TEM work and Xinhui Zhang for magneto-optical experiments and graduate students Giti Khodaparast, Jim Hicks, Jean Claude Chokomakoua, Robert Meyer, Preston Larson and Taroshani Kasturiarachchi for their assistance in various experiments. Special thanks to REU and undergraduate students who worked in Hall lab during this thesis work.

I am deeply thankful to my parents, Sharda and Jai Bhagwan Goel for their love, support and care. Their hard work and dedication are continued source of inspiration for me. I would like to thank my brother, Naval, for opening a world of opportunities for me, for guiding me through life and for making this thesis possible. I am thankful for his unselfish love, true concern and help. I will remember long drives and driving lessons forever. I cherish my dear sisters, Nidhi and Priti, who bring joy and happiness in my life.

Table of Contents

LIST OF TABLES

LIST OF FIGURES

ABSTRACT

Among all binary III-V semiconductors, InSb has the highest intrinsic electron mobility, the narrowest band gap, and the smallest electron effective mass ($m^* = 0.0139m_0$). These characteristics make InSb quantum wells (QWs) with remotely doped $Al_xIn_{1-x}Sb$ barriers promising for several novel devices. The promise of InSb QWs for spin transistors has been shown recently by experiments that demonstrate ballistic transport and a large zero-field spin splitting. Mesoscopic magnetoresistors that take advantage of the high electron mobility in InSb QWs at room temperature are currently being developed for read head applications. In order to realize such devices, InSb quantum wells were grown using molecular beam epitaxy. For some applications, the carriers are required to travel ballistically through the channel. We fabricated four-terminal structures and quantum point contacts to explore the unique effects of narrow-gap properties on ballistic transport. There is also an ongoing effort to increase the room and low temperature mobilities in these quantum well structures. The structures, so far, have been optimized to obtain room and low temperature mobilities of nearly $36{,}000\ cm^2/Vs$ and $200{,}000\ cm^2/Vs$ respectively. An attempt is also made to estimate and decrease the parallel conduction through these structures at room temperature.

INTRODUCTION

This thesis work focuses on the magneto-transport properties of electrons in quantum wells based on InSb material system. Magneto-optical properties of InSb system are also briefly discussed. Among all binary III-V semiconductors, InSb has the highest intrinsic electron mobility, the narrowest band gap, and the smallest electron effective mass. These characteristics make InSb quantum wells (QWs) with remotely doped $Al_xIn_{1-x}Sb$ barriers promising for several novel devices.

Chapter 1: Semiconductor Transport The basics of classical and quantum Hall effects are introduced in this chapter. The chapter also covers the various methods to evaluate conduction due to the presence of more than one type of carrier in the system.

Chapter 2: Molecular Beam Epitaxy The samples are grown by the state of the art technique called molecular beam epitaxy, MBE. This chapter describes the III-V MBE system at the University of Oklahoma. The quality of the surface of the wafer during the growth can be monitored *in situ* by the technique called Reflection High Energy Electron Diffraction. The MBE growth of InSb quantum wells is described in detail. To grow InSb-based structures for electronic devices, semi-insulating GaAs is used as a substrate material in spite of the large lattice mismatch (~14.6%). Atomic Force Microscopy, AFM, studies have previously reported three kinds of surface defects on the InSb QW samples: hillocks, oriented abrupt steps (OASs) and square mounds. Chapter 2 also describes the further structural information on OASs formed on our InSb quantum samples as observed by transmission electron microscopy, TEM. Finally, new buffer layer designs that give higher mobility at lower temperatures are discussed.

Chapter 3: Ballistic Transport: Negative Bend Resistance The first observation of ballistic transport in an InSb based device is presented in a study of bend resistance. The samples for this study were grown at OU. The fabrication of four terminal cross structures on the Hall bars and the magneto-transport measurements were performed at NTT Basic Research Laboratories (NTT BRL) in Japan. A diffusive component caused by a leakage path at higher temperatures is also estimated.

Chapter 4: Ballistic Transport: Quantum Point Contact The first observation of quantized conductance in InSb based structures is reported in a study of point contacts. The large *g*-factor and low effective mass of InSb makes it attractive for quantum point contact experiments. For our experiment, the samples were grown at OU while in-plane gates in Hall bars were fabricated and magneto-transport measurements were performed at NTT BRL. The conductance in the presence of parallel and perpendicular magnetic fields are presented.

Chapter 5: Mesoscopic Magnetoresistors, Spin Effects in InSb Quantum Well Our quantum well samples have been used to study mesoscopic magnetoresistors, based on an effect called "extraordinary magnetoresistance". The high room temperature mobility of InSb makes it useful material for this research on read heads for ultrahigh density magnetic storage. The first part of this chapter describes the fabrication of devices and experiments performed by researchers at NEC research labs in New Jersey and Japan.

The second part of the chapter describes zero field spin splitting in our InSb quantum well samples as extrapolated by magneto-optical measurements performed at OU.

Chapter 6: Growth of InSb on GaAs (111) Substrates The growth of InSb on higher index GaAs substrates was also studied experimentally. This chapter gives preliminary results of growth of GaAs and InSb on GaAs (111)A,B substrates. The quality of the grown samples and the defect density as seen by AFM are shown.

Chapter 7: Conclusions and Recommendations for Future Work The last chapter summarizes the results obtained in the experiments performed for this thesis. Various observations, shortcomings and the possible future directions to better understand the transport properties in InSb material system are also discussed.

Chapter 1
SEMICONDUCTOR TRANSPORT

The fundamentals of semiconductor transport are given in this chapter. The characterization of important parameters like electron density and mobility by classical and quantum Hall effects are briefly discussed. Since samples grown for this thesis were mainly single quantum wells, a introduction to two-dimensional electron gases (2DEGs) is also given. Due to the presence of more than one type of carriers in a heterostructure, like carriers in more than one subband, intrinsic carriers etc., it is possible to have a leakage path parallel to the 2DEG channel. Different techniques available to estimate the parallel conduction are summarized.

1.1 Classical Hall Effect

1.1.1 Introduction

In the Drude Model [1], a free electron gas consisting of valence electrons of the individual atoms in a crystal is considered. When atoms of an element are brought closer together, the valence electrons move freely through the crystal whereas the positive ions are stationary. As these electrons travel in all directions, the net velocity in the absence of electric field is zero. The electrons are accelerated in the electric field and there is a net drift of electrons. The main assumptions of the Drude model are that between the collisions, the electron-electron and electron-ion interactions are neglected. The electrons experience collisions with a probability per unit time $1/\tau$. The average drift velocity of the electron and hence the current density are given as

$$v_d = -eE\tau / m \tag{1.1}$$

$$j = -nev_d = \sigma_0 E \tag{1.2}$$

where E is the electric field and m is the mass of electron. The main assumption of Drude model is that carriers are scattered on an average time scale τ. The transport equation is given by

$$\frac{d\vec{p}}{dt} = -e\left(\vec{E} + \frac{\vec{p}\, x\, \vec{B}}{m^*}\right) - \frac{\vec{p}}{\tau} \tag{1.3}$$

In steady magnetic field applied in the z-direction, current density becomes

$$\boldsymbol{j} = \boldsymbol{\sigma E} \tag{1.4}$$

$$\begin{pmatrix} j_x \\ j_y \end{pmatrix} = \frac{\sigma_0}{1+\mu^2 B^2}\begin{pmatrix} 1 & -\mu B \\ \mu B & 1 \end{pmatrix}\begin{pmatrix} E_x \\ E_y \end{pmatrix} \tag{1.5}$$

where $\mu = e\tau / m^*$, $\omega_c\tau = \mu B$ and dc conductivity in absence of magnetic field is $\sigma_0 = 1/\rho_0 = ne^2\tau/m^*$ where ρ_0 is the resistivity for vanishing magnetic field. The conductivity becomes a tensor. Eq. (1.4) can also be written as

$$\boldsymbol{E} = \boldsymbol{\rho j} \tag{1.6}$$

where resistivity tensor, $\boldsymbol{\rho}$ and magnetoresistance, ρ, are

$$\boldsymbol{\rho} = \begin{pmatrix} \rho & -R_H B \\ R_H B & \rho \end{pmatrix} = \boldsymbol{\sigma}^{-1} = \begin{pmatrix} \rho_{xx} & \rho_{yx} \\ \rho_{xy} & \rho_{yy} \end{pmatrix} \tag{1.7}$$

For long, thin samples when the current is injected in the x-dir, j_y is zero in the steady state. Hall resistivity or transverse magnetoresistance, ρ and Hall coefficient, R_H are

$$\rho_y = \frac{E_y}{j_x} = -\rho_0 \, \mu B = -\frac{1}{en} B \tag{1.8}$$

$$R_H = -\frac{1}{ne} \tag{1.9}$$

The sign of Hall coefficient indicates whether electrons or holes are dominant carriers in the conduction. From Eq. (1.7)

$$\rho_{xx} = \rho_{yy} = \rho \tag{1.10}$$

$$\rho_{xx} = \frac{\sigma_{xx}}{\sigma_{xx}^2 + \sigma_{yx}^2} \tag{1.11}$$

$$\rho_{xy} = \frac{\sigma_{yx}}{\sigma_{xx}^2 + \sigma_{yx}^2} \tag{1.12}$$

In the Hall experiment, Hall resistivity as a function of magnetic field is determined. The inverse of the slope of the resulting plot gives the carrier density. The longitudinal resistance for a single carrier type is not affected by the magnetic field. But if more than one type of carrier is present in the system, a longitudinal magnetoresistance appears (Sec.1.4.1). If the assumption of energy independent scattering is relaxed, then Hall coefficient given in Eq. (1.9) becomes

$$R_H = \frac{-r}{en} \tag{1.13}$$

where, the scattering factor r is defined as

$$r = \frac{\langle \tau^2 \rangle}{\langle \tau \rangle^2} \tag{1.14}$$

Here, τ is the time between collisions. The scattering factor depends on the scattering mechanism in the semiconductor, which may depend on magnetic field and temperature.

For high magnetic fields, r approaches 1. But such high fields are difficult to achieve, therefore $r > 1$ for most Hall measurements.

1.1.2 Van der Pauw Technique and Hall Bar for 2DEGs

Semiconductor samples are characterized widely using Hall effect measurements to determine the resistivity, carrier concentration and mobility. Figure 1.1 shows (a) a Hall bar and (b) a sample with a van der Pauw geometry. In a Hall bar, when current flows from contact 1 to 4 and magnetic field is applied perpendicular to the plane of the sample, Hall voltage can be measured across contacts 2 and 6 or 3 and 5. Resistivity is determined by measuring the voltage between 2 and 3 or 6 and 5 at 0 T. Sheet resistance, $\rho_s\ (\Omega/\square)$, and mobility μ are then given by

$$\rho_s = \frac{W}{L}\frac{V_{23}}{I_{14}} \tag{1.15}$$

$$\mu = \frac{1}{ne\rho_s} \tag{1.16}$$

where W is the width of the channel and L is the length of the Hall bar between leads 2 and 3. The number of carriers per unit area is n.

Since the sample preparation for a Hall bar is time consuming process, usually a 3 mm square sample is used. Van der Pauw geometry can be used to measure carrier density and mobility if a) the contacts are at the edges of the sample, b) the contacts are small, c) the sample is of uniform carrier density, and d) the sample is singly connected [2]. For van der Pauw geometry, resistivity is

$$\rho_s = \frac{\pi}{ln2}\frac{(R_{12,34} + R_{23,41})}{2}F \tag{1.17}$$

where, $R_{12,34} = V_{34}/I$, $V_{34} = V_4 - V_3$, I = current from lead 1 to 2. Here, F is

$$\frac{R_{12,34} - R_{23,41}}{R_{12,34} - R_{23,41}} = \frac{F}{ln2} Cosh^{-1}\left(\frac{e^{\frac{ln2}{F}}}{2} \right) \qquad (1.18)$$

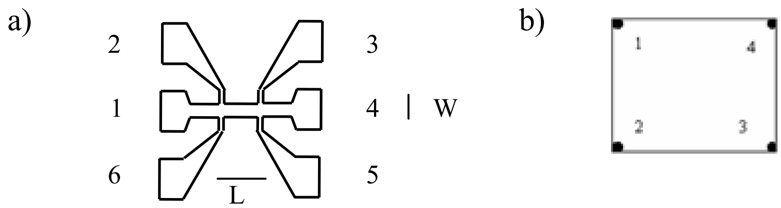

Figure 1.1: a) Hall Bar, b) van der Pauw geometry.

For symmetric samples where contacts are equally spaced, $R_{12,34} = R_{23,41}$ and F=1. So the correction factor in Eq. (1.17) is neglected. For mobility, $R_{24,13}$ with and without magnetic field is measured. The Hall mobility and carrier density are given by

$$\mu_H = \frac{\Delta R_{24,13}}{\Delta B \rho_s} \qquad (1.19)$$

$$n = \frac{1}{\rho_s e \mu_H} \qquad (1.20)$$

where $\Delta R_{24,13}$ is the change in the resistance due to the magnetic field.

1.1.3 Geometrical and Extraordinary Magnetoresistance

Typically the structure for measuring the Hall effect has a van der Pauw geometry. The injection of current at zero magnetic field makes the current density, ***j***, parallel to the electric field, ***E***. The diagonal components of conductivity tensor are non zero, Eq. (1.5). As the magnetic field is increased, ***j*** starts to make an angle to the direction of ***E*** and the non diagonal components start to contribute to the conductivity. The carriers take longer paths, as a result the resistance increases. The change between the resistance at some B field compared to the resistance at zero field is called the geometrical magnetoresistance [3]. This change in resistance is considerable for the case of a short and wide device in which the longer sides are the contacts.

If a metallic shunt is placed inside the semiconductor, the electric field will be normal to the interface between the shunt and the semiconductor. At zero magnetic field, $\vec{\boldsymbol{j}} \parallel \vec{\boldsymbol{E}}$ (only diagonal components of σ are non zero) and the carriers will go through the metal making it a short circuit. On increasing *B*, the current density starts to make an angle with *E* as off-diagonal components of σ start to contribute. With infinite *B*, $\vec{\boldsymbol{j}} \perp \vec{\boldsymbol{E}}$ and the carriers would go around the metal and hence it is an open circuit. The resistance of the sample increases as the carriers take a longer path across the interface. The change *R(B)*-*R(0)* (and hence magnetoresistance) is enhanced as the shunt changes from short circuit to open circuit. This change depends on the shape of the device, and the placement and shape of the contacts and shunt. This mechanism called “Extraordinary magnetoresistance” [4] is described further in Ch. 5, on mesoscopic magnetoresistors for read-head applications.

1.2 Quantum Transport

Free electron theory as given by Drude described conduction electrons in terms of classical statistical mechanics. It failed to consider the quantum mechanical picture which is included in Bloch theorem [5]. The Bloch theorem considers ions to be arranged in a regular periodic array with electrons moving through this periodic potential. The periodicity of the potential due to the ion lattice is

$$U(\mathbf{r}+\mathbf{R}) = U(\mathbf{r}) \tag{1.21}$$

where, **R** is a Bravais lattice vector. The electrons not only interact with the ions but among each other, too. In the independent electron approximation, however electron-electron interaction is neglected. The independent electrons satisfying the one electron Schrödinger equation with a periodic potential are called "Bloch electrons". From the Schrödinger equation for a single electron,

$$H\psi = \left(-\frac{\hbar^2}{2m}\nabla^2 + U(\mathbf{r}) \right)\psi = \varepsilon\psi \tag{1.22}$$

The eigenstate of the Hamiltonian can be chosen to have the form of a plane wave times a function with the periodicity of the lattice.

$$\psi_{n\mathbf{k}}(\mathbf{r}) = e^{i\mathbf{k}.\mathbf{r}} u_{n\mathbf{k}}(\mathbf{r}) \tag{1.23}$$

Here, **k** is not proportional to the electron momentum. It is a quantum number characteristic of the translational symmetry of a periodic potential. The band structure is determined by the dependence of electron energy on **k**.

1.2.1 Landau Levels

In quantum mechanics, the Schrödinger equation for a particle in electric and magnetic fields is

$$\left(\frac{1}{2m}(\vec{p} - e\vec{A})^2 + e\phi\right)\psi = \varepsilon\psi \tag{1.24}$$

In a uniform magnetic field (applied in z-dir) this equation is solved by considering the Landau gauge with ***A*** *= (0, Bx, 0)*. Since the vector potential is independent of y, the wave function is a product of a plane wave in y with some function of x. Using the wavefunction $u(x)e^{iky}$ gives Schrödinger equation for 1D harmonic oscillator [1, 5, 6].

$$(\frac{-\hbar^2}{2m}\frac{d^2}{dx^2}+\frac{1}{2}m\omega_c^2(x-\frac{\hbar k}{eB})^2)u(x)=\varepsilon u(x) \tag{1.25}$$

The cyclotron frequency appears like in the classical case but the vertex of the parabolic potential is displaced to $x_k = \hbar k / eB$. The magnetic length or the radius of the lowest orbit is

$$l_B = \sqrt{\frac{\hbar}{eB}} \tag{1.26}$$

As the magnetic field is increased, the radius of orbit decreases. Energy for the motion in xy plane is independent of k and is given as

$$\varepsilon = (n+\frac{1}{2})\hbar\omega_c \qquad\qquad n = 0,\ 1,\ 2,\ldots\ldots \tag{1.27}$$

The different oscillator levels are called Landau levels. States with same n but different k are degenerate.

1.2.2 Electrons in 3-dimensions

For a isotropic system in zero magnetic field, the Fermi surface is spherical in ***k*** space. The density of states (number of electronic states per unit energy range per unit volume) of a free electron gas in three dimensions [5] is proportional to the square root of the energy,

$$D(E) = \frac{1}{2\pi^2}\left(\frac{2m}{\hbar^2}\right)^{3/2}\sqrt{E} \tag{1.28}$$

In the presence of a magnetic field, the electron states condense into coaxial cylinders of axis k_z and radii $k_x^2 + k_y^2 = 2m^*(n+1/2)\hbar\omega_c/\hbar^2$ (where $n = 0, 1, 2\ldots$). As k_z can take any value, k^2 is continuous.

1.2.3 Two-dimensional Electron Gas

In a quantum well structure, an electron is confined in one dimension. For example, a layer of InSb is grown sandwiched between two lattice matched barrier layers of $Al_xIn_{1-x}Sb$. As conduction band edge of InSb lies below that of AlInSb, an electron is essentially confined to the InSb layer. The 2D density of states of a free electron gas, 2DEG, is independent of the energy

$$D(E) = \frac{m^*}{\pi\hbar^2} \tag{1.29}$$

On application of a B-field, the constant density of state changes to δ-functions called Landau levels, as discussed in Sec. 1.2.1. These levels each contain a large number of degenerate states. For such 2D system in the magnetic field (applied perpendicular to the heterointerface in z-dir), the 3D cylinders change to concentric rings because k_z is quantized. There are gaps in the values of k^2. The total energy of the electron is the sum of quantized energy, E_z and the kinetic energy in *x-y* plane.

$$E = E_z + \frac{\hbar^2}{2m^*}\left(k_x^2 + k_y^2\right) \tag{1.30}$$

The band structure near the bottom of the conduction band is parabolic with the energy of the electron given as

$$E = \frac{\hbar^2 k^2}{2m^*} \tag{1.31}$$

For narrow band gap semiconductors, like InSb, the interaction between the conduction band, light and heavy holes and spin-orbit split-off bands causes the dispersion relation for the conduction band to become non-parabolic. These interactions are modeled as **k.p** theory [7]. Because of the non-parabolicity, the effective mass is dependent on the energy and the energy of the electron becomes

$$E(k) = \frac{\hbar^2 k^2}{2m^*(E)} \tag{1.32}$$

Now we can consider the electron spin. There is a magnetic moment associated with the spin in the presence of B-field. The spin up or down electrons have moments either parallel or antiparallel to the field. These configurations have different energies. The total energy of the electron in the magnetic field is

$$E = E_Z + (n + \frac{1}{2})\hbar\omega_c \pm \frac{1}{2} g\mu_B B \qquad n = 0, 1, 2 \ldots \tag{1.33}$$

In this equation, E_z is the energy of the standing wave in *z*-direction, the second term is the cyclotron energy and the last term is the Zeeman energy of the electron. The *g*-factor is nearly 2 for free electrons. But *g* may take different values in a solid depending on the band structure. For bulk InSb, the *g*-factor is negative and is equal to -51.

1.2.4 One-dimensional Electron Gas

A 2DEG gas can be confined additionally to form a 1D system. This is achieved by etching the material containing the 2DEG so that only a thin strip of the 2DEG remains. The electrons are now confined in two directions and are free to move in the third direction. This is a quantum wire. An example of a quantum wire is a quantum point contact. On the surface of the structure which contains the 2DEG, a layer of metallic gate is deposited (split-gate) or an in-plane gate is etched. When a negative voltage is applied to the gate, the electrons are repelled from under the gate (in the split-gate) or from the sides of the gate (in the in-plane gate geometry). The width of the 2DEG varies as the gate potential is changed.

The quantum wire can thus be produced electrostatically. If the confinement is in z- and x-directions, the energy is given by

$$E = E_z + E_x + \frac{\hbar^2 k_y^2}{2m^*} \tag{1. 34}$$

For square box confinement,

$$E_x = \frac{\hbar^2 \pi^2 (i+1)^2}{2m^* L^2} \qquad i = 0, 1, 2, \ldots. \tag{1.35}$$

where L is the width of the well. For parabolic confinement (as in split gates), $U(x) = (½)m\omega_0^2 x^2$ and the energy is

$$E_x = \hbar\omega_0 (i + 1/2) \qquad i = 0, 1, 2, \ldots. \tag{1.36}$$

The 1D density of state for free electrons is

$$D(E) = \frac{1}{\pi}\left(\frac{2m}{\hbar^2}\right)^{1/2} \frac{1}{\sqrt{E}} \tag{1.37}$$

1.2.5 Shubnikov-de Haas Effect

As the perpendicular magnetic field is applied in 2D heterostructures, the states coalesce into Landau levels, which are delta spikes in the absence of impurities in the system. If a Landau level is only partially full, the Fermi level will be in that Landau state. The magnetic field changes the number of energy states per unit area in a Landau level

$$N_L = \frac{eB}{h} \tag{1.38}$$

Changing either the magnetic field or the electron concentration can change the number of occupied Landau levels. When the last occupied landau level is completely filled, the next electron will lie in the next higher Landau level, making the Fermi level to jump to that energy. Thus the physical quantities that depend on the Fermi level, oscillate with the magnetic field or the electron density. Shubnikov-de Haas effect is the oscillatory dependence of longitudinal resistivity (magnetoresistance) on the magnetic field. Carrier density can be deduced from the minima due to two adjacent Landau levels,

$$n = \frac{e}{h\Delta(1/B)} \tag{1.39}$$

If i number of Landau levels are filled, then from Eq. (1.38), carrier concentration is

$$n = \frac{ieB}{h} \tag{1.40}$$

1.2.6 Quantum Hall Effect

When the magnetic field is high and the temperature is low, there is a change from the linear variation in the Hall voltage and the oscillations in longitudinal resistance as a function of magnetic field. A series of steps appear in the Hall resistance. The values at which these steps appear is precisely the same in any material system. Resistance is quantized in units of $h/(ie^2)$, where i is an integer. The longitudinal resistance is zero at B corresponding to the well defined plateaus in Hall resistance. This is the Quantum Hall Effect, QHE. Figure 1.2 shows the quantum Hall plateaus and zero longitudinal resistance observed in an $InSb/Al_{0.15}In_{0.85}Sb$ heterostructure (s939) at 5 K. The value of integer i is listed for two plateaus seen in the plot. The density and mobility calculated from the data are $4.5 \times 10^{11}\ cm^{-2}$ and $100{,}000\ cm^2/Vs$ respectively.

The conductivity tensor components are

$$\sigma_{xy} = \frac{ie^2}{h} = \frac{1}{\rho_{xy}} \tag{1.41}$$

$$\sigma_{xx} = 0 \tag{1.42}$$

The Hall resistivity does not change when Fermi level lies in the gap between two Landau levels. As a result, a plateau is seen. This quantization appears only near *B* values at which the Landau level is completely filled. When the Fermi level lie in a Landau level, the Hall voltage changes and the longitudinal resistance has a finite value. The two main points of integer quantum Hall effect, IQHE, are Eq. (1.41) and $\rho_{xx} = 0$ near integer filling factors.

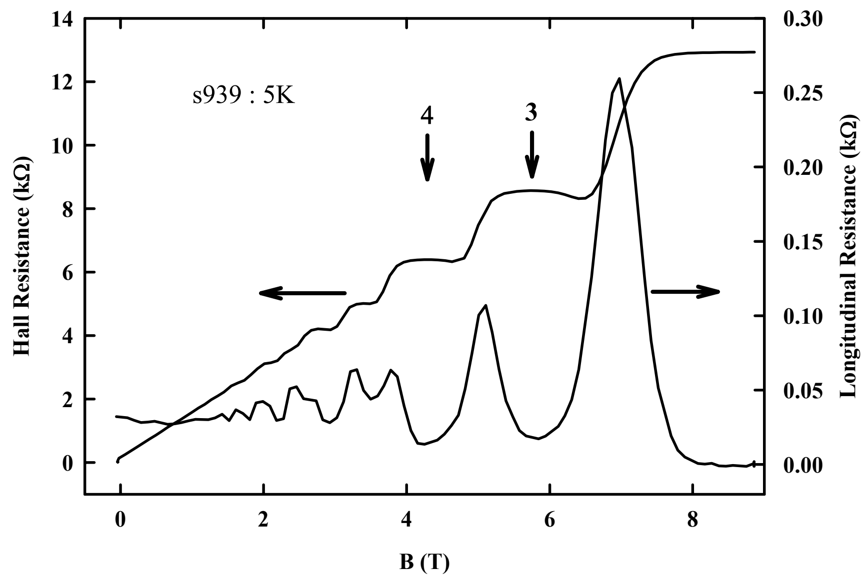

Figure 1.2: Hall resistance and longitudinal resistance as functions of temperature for $Al_{0.15}In_{0.85}Sb$/ InSb single quantum well (s939, 11.5 nm wide square well with 29.5 nm wide $Al_{0.15}In_{0.85}Sb$ barriers) at 5 K. The density and mobility are *4.5* x 10^{11} cm^{-2} and *100,000* cm^2/Vs respectively.

Due to the presence of disorder like impurities, interface roughness etc. in the real system, the delta spikes of the Landau levels broaden. The states present in the tails of the broadened levels are localized in space. The zero value of the longitudinal resistivity can also be understood by considering these localized states. On changing the number of carriers or the magnetic field, the Fermi level can lie either in the delocalized conducting Landau states, where $\rho_{xx} \neq 0$ due to the presence of scattering, or in the localized states where carriers require finite energy to scatter to an empty state. In the localized states, $\rho_{xx} = 0$ and ρ_{xy} is constant. This explains the observation of plateaus in Hall resistance and zero longitudinal resistance at certain magnetic fields.

1.3 Cyclotron and Spin Resonance

In the classical picture, if a magnetic field is applied perpendicular to the plane of the sample, the carriers move in a circular orbit in the plane with cyclotron frequency. The resonance absorption due to these carriers when light is present, is called cyclotron resonance. Quantum mechanically, the transition between Landau levels with same spin is called cyclotron resonance. The cyclotron resonance (CR) transitions can occur between a filled or a partially filled state to the empty or partially empty state with change in Landau level index of 1. Spin resonance (SR) is the transition in a Landau level between up and down spin states with the same Landau level index. The CR and SR studies performed on InSb quantum wells are described in Ch. 5.

1.4 Parallel Conduction

1.4.1 Multi-carrier System

For n carrier types present, the induced current is related to the field by

$$\boldsymbol{E}_n = \boldsymbol{\rho}_n \boldsymbol{j} \tag{1.43}$$

$$\boldsymbol{\rho}_n = (\sum \rho_n{}^{-1})^{-1} \tag{1.44}$$

Equations of the Hall coefficient and magnetoresistance in two carriers system are given in Appendix 1. For m carriers, conductivity tensors are given as,

$$\sigma_{xx}(B) = \sum_{i=1}^{m} \frac{e n_i \mu_i}{1 + (\mu_i B)^2} \tag{1.45}$$

$$\sigma_{xy}(B) = \sum_{i=1}^{m} S_i \frac{e n_i \mu_i^2 B}{1 + (\mu_i B)^2} \tag{1.46}$$

Here, the density and mobility for the i^{th} carrier are n_i and μ_i. For holes and electrons, S_i is $+1$ or -1 respectively. Figure 1.3 (a) shows the Hall resistance and longitudinal resistance in InSb / $Al_{0.12}In_{0.88}Sb$ single quantum well sample (s936) at 4.2 K. The well width is 25 nm and the barriers thickness is 39 nm. As seen in Figure 1.3 (a), the non linear Hall resistance and the longitudinal resistance plot point towards more than one type of carrier contributing to the charge transport. The conduction band diagram for this structure is given in Figure 1.3 (b). Considering non-parabolicity, the first two subbands levels are E_0 = 20 meV and E_1 = 70 meV. For the given well width, the maximum number density of carriers in the first subband level without populating the second subband is estimated to be $4 \times 10^{11}\ cm^{-2}$. The parallel conduction due to low mobility carriers in the heterostructures can significantly affect the transport. To estimate parallel conduction through the structures, various techniques are being used in literature. A few of these are summarized in the next few subsections.

1.4.2 Multi-carrier Fitting

Equations for conductivity tensors in multi-carrier system are given by Eq. (1.45, 1.46). These equations are used to fit experimental data for Hall coefficient and resistivity. This is called multi-carrier fitting (MCF). The disadvantage of this technique is that the type of carriers and number of carriers are guessed and their respective mobilities are assumed.

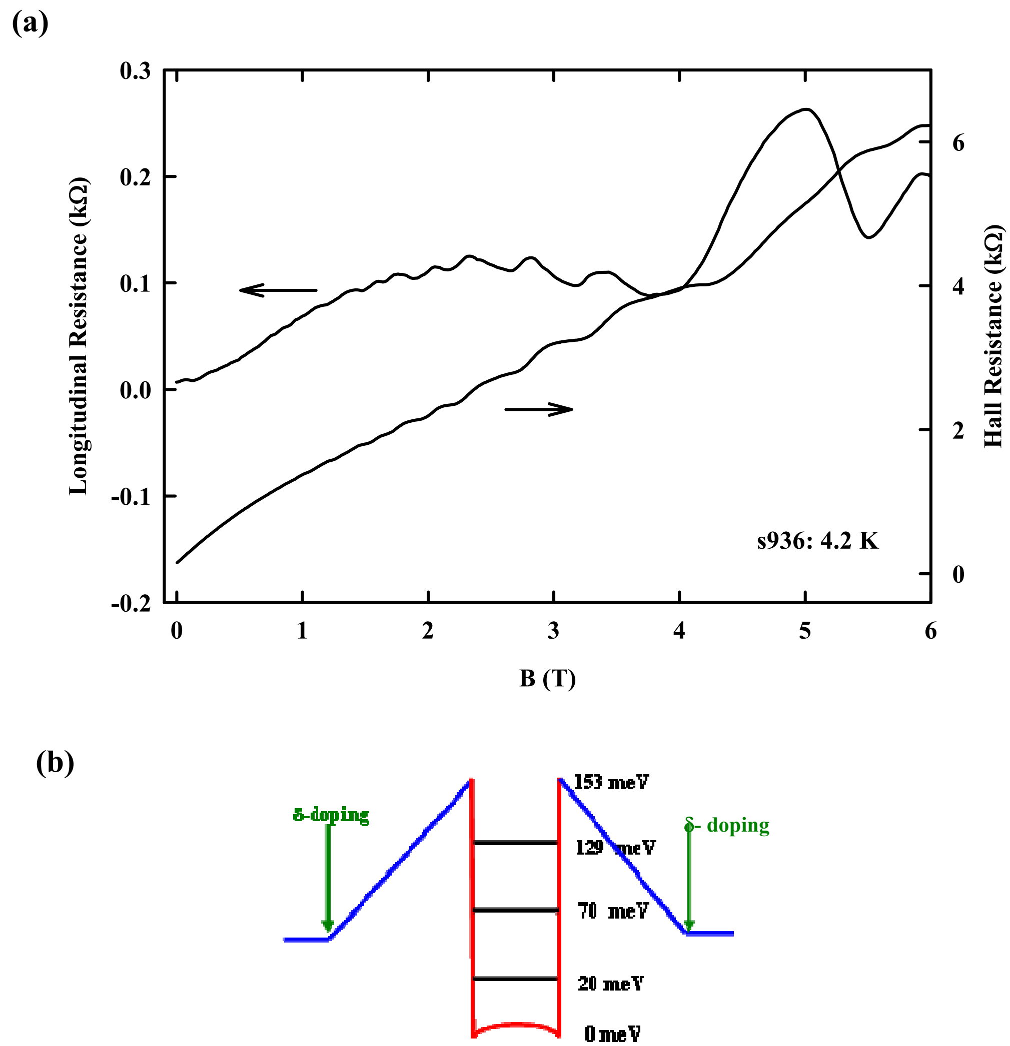

Figure 1.3: a) Hall resistance and longitudinal resistance for s936 at 4.2 K. The density and mobility of electrons in the quantum well as deduced at small B values are *4.1* x *10^{11} cm^{-2}* and *200,000 cm^2/Vs* respectively. b) The conduction band diagram for s936 (25 nm wide well, $Al_{0.12}In_{0.88}Sb$ barriers, non-parabolicity considered).

1.4.3 Mobility Spectrum Analysis

Mobility spectrum analysis [8] is the transformation of the electrical conduction vs magnetic field into electrical conduction density vs mobility. If it is assumed that there is a continuous distribution of electrons and holes of any mobility within the sample then, conductivity tensor components are given as,

$$\sigma_{xx}(B) = \int_{-\infty}^{\infty} d\mu \frac{s^p(\mu)+s^n(\mu)}{1+\mu^2 B^2} \tag{1.47}$$

$$\sigma_{xy}(B) = \int_{-\infty}^{\infty} d\mu \frac{(s^p(\mu)-s^n(\mu))\mu B}{1+\mu^2 B^2} \tag{1.48}$$

Here hole and electron conductivity density functions are given by,

$$s^p(\mu)=ep(\mu)\mu \tag{1.49}$$

$$s^n(\mu)=en(\mu)\mu \tag{1.50}$$

where, $p(\mu)$ and $n(\mu)$ are the hole and electron density functions respectively. Beck and Anderson [8] obtained the unique envelopes $s^p(\mu)$ and $s^n(\mu)$ which are δ-like amplitudes at μ. The carrier species can be identified from the peaks in the envelope spectrum. Although, this does not provide quantitative information as finding unique values for functions $s^p(\mu)$ and $s^n(\mu)$ would, but various species can be still be identified.

1.4.4 Dziuba and Gorska Technique

The Dziuba and Gorska (DG) approach calculates a more accurate mobility distribution instead of just an upper bound envelope [9]. The integrals in Eq. (1.47, 1.48) are approximated by sums of partial contribution by carriers having a grid of discrete mobilities.

$$\sigma_{xx}(B) = \sum_{m}^{i=1} \frac{S_i^{xx} \Delta\mu_i}{1+\mu_i^2 B_j^{\ 2}} \tag{1.51}$$

$$\sigma_{xy}(B) = \sum_{m}^{i=1} \frac{S_i^{xy} \mu_i B_j \Delta\mu_i}{1+\mu_i^2 B_j^{\ 2}} \tag{1.52}$$

Here m is the number of points in the final mobility spectrum and,

$$S_i^{xx} = s^p(\mu_i)+s^n(\mu_i) \tag{1.53}$$

$$S_i^{xy} = s^p(\mu_i)-s^n(\mu_i) \tag{1.54}$$

S_i^{xx} and S_i^{xy} contain partial conductions from electrons S_i^n and holes S_i^p,

$$S_i^{xx} = S_i^n + S_i^p \tag{1.55}$$

$$S_i^{xy} = S_i^n - S_i^p \tag{1.56}$$

where,

$$s^n(\mu) = S_i^n \ \delta(\mu-\mu_i) \tag{1.57}$$

$$s^p(\mu) = S_i^p \ \delta(\mu-\mu_i) \tag{1.58}$$

and δ is the Dirac delta function. This gives,

$$s^n(\mu_i) \approx S_i^n/\Delta\mu_i \tag{1.59}$$

$$s^p(\mu_i) \approx S_i^p/\Delta\mu_i \tag{1.60}$$

The electrical conduction density functions $s^n(\mu)$ and $s^p(\mu)$ or (S_i^n,μ), (S_i^p,μ) are therefore estimated.

The DG technique involves obtaining the mobility spectrum by iterative approach. The steps involved are as follows. First the test function is obtained. Then using the test function, the first trial function for iteration is obtained. To obtain the initial spectrum (first trial function), Dziuba and Gorska employed a simpler technique [9] compared to the one given by Beck and Anderson [8], Sec. 1.4.3. Further iterations are carried out to estimate the trial functions such that there is a good agreement between the theoretical and experimental conduction tensor components. In their procedure, they chose a set of mobilities, μ_i, and calculated the partial conductions (S_i^{xx}, μ_i) and (S_i^{xy}, μ_i) for $\sigma_{xx}(B)$ and

σ_{xy} *(B)*. The test functions for σ_{xx} *(B)* and σ_{xy} *(B)* are functions $S_{xx}(\mu)$ and $S_{xy}(\mu)$. The first trial functions are calculated using the test functions obtained by the method given in Ref. 9. The first trial functions are defined as,

$$S_{i,0}^{xx} = c_{xx} S^{xx}(\mu_i) \tag{1.61}$$

$$S_{i,0}^{xy} = c_{xy} S^{xy}(\mu_i) \tag{1.62}$$

where c_{xx} and c_{xy} are normalizing constants. Using the above equations,

$$\sigma_{xx}(B) = c_{xx} \sum_{\mu_{min}}^{\mu_{max}} \frac{S^{xx}(\mu_i)}{1+(\mu_i B)^2} \tag{1.63}$$

$$\frac{\sigma_{xy}(B)}{B} = c_{xy} \sum_{\mu_{min}}^{\mu_{max}} \frac{\mu_i S^{xy}(\mu_i)}{1+(\mu_i B)^2} \tag{1.64}$$

$$\mu_{min} = 1/B_{max} \tag{1.65}$$

$$\mu_{max} = 1/B_{min} \tag{1.66}$$

Normalizing constants are calculated from

$$c_{xx} = \frac{\sum_{B_{min}}^{B_{max}} \sigma_{xx}^{exp}(B_i)}{\sum_{\mu_{min}}^{\mu_{max}} \frac{S^{xx}(\mu_i)}{1+(\mu_i B)^2}} \tag{1.67}$$

$$c_{xy} = \frac{\sum_{B_{min}}^{B_{max}} \sigma_{xy}^{exp}(B_i)}{\sum_{\mu_{min}}^{\mu_{max}} \frac{\mu_i S^{xy}(\mu_i)}{1+(\mu_i B)^2}} \tag{1.68}$$

1.4.5 Quantitative Mobility Spectrum Analysis

One of the disadvantages of Dziuba and Gorska iteration method is that the shape of the mobility spectrum cannot be determined uniquely. The quantitative mobility spectrum analysis (QMSA [10, 11]) is based on DG approach with some modification. It involves the mobility spectrum to determine the number and type of carriers and to roughly estimate their densities and mobilities. This information is then used in multi-carrier fit to obtain the final values which agree reasonably with the experimental results. Here, $s^p(\mu)$ and $s^n(\mu)$ are constrained to be non-negative at each iteration step. In this technique, the MSA envelope is used as the initial trial function. First of all, S_i^{xx} and S_i^{xy} are solved for.

$$S_i^{xx} = (1+\mu_i^2 B_i^2)[\sigma_{xx}^{exp}(B_i) - \sum_{j\neq i}^{m} \frac{S_j^{xx}}{1+\mu_j^2 B^2}] \tag{1.69}$$

$$S_i^{xy} = \frac{(1+\mu_i^2 B_i^2)}{\mu_i B_i}[\sigma_{xy}^{exp}(B_i) - \sum_{j\neq i}^{m} \frac{S_j^{xy}\mu_j B_i}{1+\mu_j^2 B_i^2}] \tag{1.70}$$

The values of S_i^{xx} and S_i^{xy} are used in Eq. (1.69, 1.70) in the next iteration step as soon as they are calculated. The new sets of S_i^{xx} *(k+1)* and S_i^{xy} *(k+1)* can thus be calculated using Gauss-Seidel iterative approach.

$$S_i^{xx}(k+1) = (1+\mu_i^2 B_i^2)[\sigma_{xx}^{exp}(B_i) - \sum_{j=1}^{i-1} \frac{S_j^{xx}(k+1)}{1+\mu_j^2 B_i^2} - \sum_{j=i+1}^{m} \frac{S_j^{xx}(k)}{1+\mu_j^2 B_i^2}] \tag{1.71}$$

$$S_i^{xy}(k+1) = \frac{(1+\mu_i^2 B_i^2)}{\mu_i B_i}[\sigma_{xy}^{exp}(B_i) - \sum_{j=1}^{i-1} \frac{S_j^{xy}(k+1)\mu_j B_i}{1+\mu_j^2 B_i^2} - \sum_{j=i+1}^{m} \frac{S_j^{xy}(k)\mu_j B_i}{1+\mu_j^2 B_i^2}] \tag{1.72}$$

To control the convergence speed factor ω_{xx} and ω_{xy} are introduced to the above equations giving overrelaxed iteration algorithm, Eq. (1.73, 1.74). In order to exclude the uncertainty in the experimental data, only a few experimental points that define the experimental conductivity curves are considered. Using spline interpolation technique, more data points are generated in between the experimental points. The number of data points defines the resolution of the mobility spectrum.

$$S_i^{xx}(k+1) = (1-\omega_{xx})S_i^{xx}(k) + \omega_{xx}\{(1+\mu_i^2 B_i^2)[\sigma_{xx}^{exp}(B_i) - \sum_{j=1}^{i-1}\frac{S_j^{xx}(k+1)}{1+\mu_j^2 B_i^2}$$

$$-\sum_{j=i+1}^{m}\frac{S_j^{xx}(k)}{1+\mu_j^2 B_i^2}]\}$$

(1.73)

$$S_i^{xy}(k+1) = (1-\omega_{xy})S_i^{xy}(k) + \omega_{xy}\{\frac{(1+\mu_i^2 B_i^2)}{\mu_i B_i}[\sigma_{xy}^{exp}(B_i) - \sum_{j=1}^{i-1}\frac{S_j^{xy}(k+1)\mu_j B_i}{1+\mu_j^2 B_i^2}$$

$$-\sum_{j=i+1}^{m}\frac{S_j^{xy}(k)\mu_j B_i}{1+\mu_j^2 B_i^2}]\}$$

(1.74)

The net carrier concentration for a given species is obtained by summing over all the contributions under the peak corresponding to that carrier,

$$n = \sum_i \frac{\sigma_i}{e\mu_i} \tag{1.75}$$

The convergence is measured as the error between the experimental and QMSA values,

$$\Delta E^2(k) = \frac{\sum_i [\sigma_i^{exp} - \sigma_i^{QMSA}(k)]^2}{\sum_i [\sigma_i^{exp}]^2} \tag{1.76}$$

where, σ_i is either σ_{xx} or σ_{xy}. The QMSA is employed to accurately estimate the parallel conduction through our quantum well structures in Ch. 3.

Chapter 2
MOLECULAR BEAM EPITAXY

Over the years, various techniques like Liquid Phase Epitaxy (LPE), Metal Organic Chemical Vapor Deposition (MOCVD) and Molecular Beam Epitaxy (MBE) have been developed to grow semiconductors. The growth of these layers can be precisely controlled to the minimum thickness of few atoms, facilitating the growth and study of interesting electronic and optical devices. In the 1970s, MBE was developed to grow high purity epitaxial layers of compound semiconductors at a rate of ~1 μm/h in a chamber maintained at Ultra High Vacuum (UHV: ~ 10^{-9} to 10^{-11} Torr). The source materials are contained in crucibles which are heated to evaporate the material. By opening a shutter in front of each crucible, molecular beams of several materials are made to interact on the surface of a substrate. The chamber is kept at low pressures to minimize incorporation of unwanted impurities. The quality of the growth can be monitored *in situ* using a technique called Reflection High Energy Diffraction, RHEED. The flux of a beam can be calibrated in terms of vapor pressure of the source material. Figure 2.1 shows the schematic of a MBE system and a cross-sectional TEM image of a layer sequence of InSb/AlInSb quantum well structure grown by MBE.

This chapter gives an introduction to the MBE growth modes (Sec. 2.1) and crystal defects (Sec. 2.2). Sec. 2.3 talks about the molecular beam epitaxy system at the University of Oklahoma. The sample is monitored *in situ* by RHEED (Sec. 2.4) during growth of InSb quantum wells with AlInSb barriers (Sec. 2.5). The structural defects in InSb quantum well structures grown on GaAs (001) substrates are detailed in Sec. 2.6. The optimization of the structure to reduce defect density, reduce parallel conduction and increase the mobility at low and room temperature is discussed in Sec. 2.7.

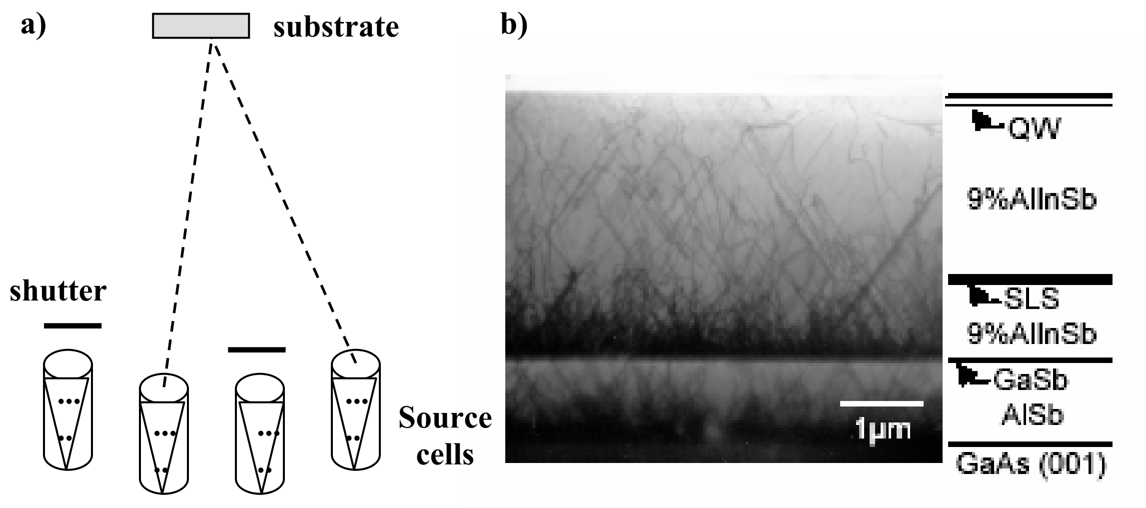

Figure 2.1: a) Schematic of a MBE system. b) Cross-sectional TEM image of an InSb/AlInSb quantum well layer structure grown by MBE [Ref.12].

2.1 Growth Modes

There are three main epitaxial growth modes: a) Frank-Van der Merwe or layer by layer, b) Volmer-Weber and c) Stranski-Krastanov. In Frank-Van der Merwe mode, the attraction between the deposited atom and the substrate is stronger than that between the deposited atoms. As a result, monolayer islands of deposits are formed which coalesce into a complete layer as the growth proceeds. In the Volmer-Weber mode, the attraction between the deposited atom and the substrate is smaller than that between the deposited atoms. The atoms form aggregates on the substrate which in turn, get bigger in size and start to touch each other resulting in a continuous film eventually. In the Stranski-Krastanov mode, initially few monolayers are formed on the substrate. Three-dimensional islands are then nucleated on top of these monolayers. Growth in this way can lead to misfit dislocations in the structure.

2.2 Defects

Semiconductor defects can be classified based on their dimensionality. Point defects, line defects, area and volume defects are 0D, 1D, 2D and 3D defects, respectively.

2.2.1 Point Defects

A vacancy is a point defect. In this defect an atom is missing from the lattice site. An interstitial is an atom present in between the lattice positions. If the atom at the interstitial is the same as the atoms that resides on the lattice sites then it is called self-interstitial. If the interstitial comes from the nearby vacancy then it is called a vacancy-interstitial combination (Frenkel defect). Both vacancies and interstitials are intrinsic defects.

2.2.2 Line Defects

A line defect is caused by an impurity atom at an interstitial site or at a lattice site. When the impurity atom is at the lattice site, it is called substitutional impurity. The most common line defect is a dislocation. The dislocation in the crystal occurs due to stress. If a shear force, applied on the two halves of the crystal on either side of a crystal plane, is large enough to separate the two sides by one atomic spacing, screw dislocation results. The dislocations are often caused when the point defects in the crystal stick together until a dislocation is formed. In a dislocation, an extra plane of atoms is inserted in between two other planes of atoms. In the edge dislocation, the extra plane is terminated on one end by the edge of the crystal. In the dislocation loop, the extra plane is contained in the crystal.

Threading dislocations are present in epitaxial layers grown on mismatched substrates. When a thin layer of mismatched material is grown on a substrate, the epitaxial layer is strained to match the lattice spacings of the substrate. If the thickness of the epitaxial layer exceeds a critical thickness, misfit dislocations set in at the interface.

2.2.3 Area Defects

One type of area defect is the stacking fault. It is an extra plane of atoms, in which the pattern is regular only in one direction. Stacking faults are disrupted by the edge of the crystal or by the dislocation lines. When grow this on {111} substrates, the stacking faults appear as triangles and lines on the surface of epilayer. When layers are grown on {100} substrates, the faults appear as squares. During epitaxial growth, atomic planes are deposited one at a time with a new plane formed after the first plane is completed. If however, there is a mismatch in a small region with respect to the substrate, there is irregularity in layer structure. The new layers continue to grow with this fault. These defects propagate from layer to layer and increase in size with each plane. A twinning defect occurs when one portion of the crystal lattice is oriented with respect to the other. The two parts are in contact over the surface called twinning plane. The twinning plane has a large concentration of broken bonds. This region is called the grain boundary.

2.3 MBE at University of Oklahoma

2.3.1 Pumps

Since the MBE chamber must be kept as clean as possible, it is essential that there is no backstreaming of oil from the pump to the chamber. Therefore, ultra high vacuum (UHV) in the system is achieved using a cryopump, an ion pump and a titanium sublimation pump.

A molecular drag pump is used to achieve a pressure of ~10^{-3} Torr which serves as a forepump for the cryopump and ion pump.

In an ion pump, the gas molecules are ionized. By applying an electric field, the resulting ions are removed from the system by attracting these ions to a negatively charged plate. The cathode is made of titanium. When the ions hit the cathode, a little titanium is sputtered off on to the surrounding surface. The gas molecules react with clean titanium surface to form molecules and therefore removed (gettering). In Titanium sublimation pumps (TSP), an additional source of titanium is added. One type of source is a titanium-molybdenum alloy filament. This source when heated, deposits titanium. This pump works on the principle of gettering as well.

A cryopump operates near liquid He temperatures. It has two stages, one is 15 K and the other is 80 K stage. Some gas molecules (for example H_2O) coming into the pump reaches the 80 K stage first and are adsorbed. Other molecules (O_2, N_2, CO_2 for example) are not adsorbed until they reach the 15 K stage.

2.3.2 Growth Chamber, Buffer Chamber and Load Lock

The system at OU is an Intevac Modular GEN II, 3" MBE system. This system has three chambers: a growth chamber, a buffer chamber and a load lock/ entry-exit chamber.

The new substrates are loaded on (and after growth removed from) a trolley in the entry exit chamber after opening it to the atmosphere. The chamber is then pumped down using a forepump and a cryopump (CRYO TORR CT-100). When the pressure reaches about 5 x 10^{-7} Torr, the trolley is outgassed with a quartz lamp at 200 ^{0}C for 2 hours. After outgassing, when the chamber has cooled down to the room temperature, the trolley is transferred to the buffer chamber.

The pressure in buffer chamber is maintained in the ~10^{-10} Torr range by an ion pump. The pressure can be further decreased to the 10^{-11} Torr range by a TSP. The buffer chamber has a heater port to outgas the substrate prior to loading it into the growth chamber.

Idle pressure in the growth chamber is ~ 10^{-11} Torr. The growth chamber has six source cells. These cells are loaded with, Gallium (Ga, United Mineral & Chemical Corp., 7N Grade), Arsenic (As, UMC, 7N5 Grade), Antimony (Sb, Dowa Mining Co. Ltd., 6N5 Grade), Indium (In, RASA, 7N Grade), Aluminum (Al, UMAT, MBE Grade) and Silicon (Si, Silicon Sense Ltd, Silica Source Technology Corp., SI-Tech Inc.). In is contained in a dual zone effusion cell, Sb is stored in a cracker effusion cell while the rest of the source materials are loaded in single zone effusion cells. The Sb cell has two parts, a "bulk" evaporator and a pyrolytic "cracker". The material is stored in the "bulk" that is surrounded by a liquid (water) cooling jacket for dissipating heat. The 'cracker' breaks Sb_4 into Sb_2 and Sb. Cold alcohol flows in the shroud between the cells to prevent hot spots and interaction between the hot cells. The TSP, ion pump, cryopump (CRYO-TORR CT-8) and liquid Nitrogen cryopanels are used to bring the pressure in the growth chamber into the UHV range.

Care is taken while melting or solidifying Al. The crucible can crack due to the stress induced by rapid melting or refreezing of the charge when temperature fluctuates around the melting point of Al. Freezing of the Al charge during a power failure can also crack the crucible. Care must be taken while loading the charge as well. The 60 c.c. crucible should be filled only up to ~10% of its capacity as Al tends to creep up the crucible wall when melted. The charge should be held in a double walled crucible or in a single walled crucible with a pBN insert. Care must also be taken while decreasing the Ga cell to the room temperature. The melting point of Ga is ~30 ^{0}C. If the power to the cell goes off while alcohol is cooling the shroud, the Ga charge will solidify. The rapid freezing of the charge cracks the crucible due to thermal expansion of the charge. Remelting of the charge in the cracked crucible can lead to Ga creeping out of the cracks and damaging the cell.

InSb quantum well samples are grown on GaAs (001) substrates (AXT, Inc.). Since these are epi-ready substrates, no pre-load cleaning is required. The 3" substrate is cleaved into quarters and a different epilayer is grown on each quarter. The flux of source material falls on the substrate from different directions. As a result, the distribution of deposited material can differ, giving non uniform layers. The substrate is therefore rotated (~25 rpm in this work) during growth to maintain a consistency in the thickness and the composition of the layer grown throughout the wafer. An ion gauge at the sample position can be used to monitor and measure the intensity of the molecular beams. During the growth, the III-V beam flux ratio is maintained. This serves as a good growth monitoring tool when the growth rate data from RHEED measurement is not available.

2.4 Reflection High Energy Electron Diffraction

The MBE system has an *in situ* RHEED system for surface characterization. A 9.5 keV electron beam strikes the surface of the substrate at a grazing angle. The diffracted beam is observed on a phosphor-coated screen mounted on a viewport. The surface structure and lattice constant can be determined from the separation of the diffracted beam. The flux ratio and substrate temperature can be calibrated by the transition from one surface reconstruction to the other. RHEED is also used before initiating the growth, to determine whether the native oxides have been removed from the surface of the substrate.

2.4.1 Calibration of Growth Rates

The energy states on the surface of a crystal are typically not completely filled. These states can be due to dangling bonds that align themselves in a way that reduces the surface energy. The atoms at the surface are therefore aligned differently than in the bulk crystal. The surface alignment of the atoms, called the surface reconstruction, depends on the ratio of the species present and on the substrate temperature. The optimal growth conditions for GaAs (001) homoepitaxy can be characterized by a (2x4) RHEED pattern. In InSb, a (2x4) reconstruction is not present. Figure 2.2 shows a) c(4x4) and b) '1x3' (called pseudo 1x3) RHEED patterns observed on an InSb surface. For the substrate temperature below a certain critical temperature, c(4x4) pattern is seen under Sb-rich conditions on the surface. A 2x pattern is seen along [110] and $[1\bar{1}0]$ directions. As the substrate temperature is increased keeping the flux ratio of In and Sb same, instead of the 2x pattern along the $[1\bar{1}0]$ direction, two fractional-order streaks are seen. The splitting fraction (ratio of the distance between the two fractional order streaks to that between integral–order streak) is around 0.25.

Earlier results have shown good InSb growth on '1x3' surfaces. It is still not clear what causes this reconstruction. Oliveira et al. [13] have suggested that the coexistence of analogous (2x4) structures with different Sb coverages may be responsible for these fractional order diffraction streaks. As the substrate temperature is increased, the surface reconstruction in our AlInSb alloy layer changes from c(4x4) $\rightarrow$ symmetric (1x3) $\rightarrow$ '1x3'. This suggests that InSb '1x3' may be closely related to the (1x3) RHEED pattern observed on GaSb and AlSb surfaces [14].

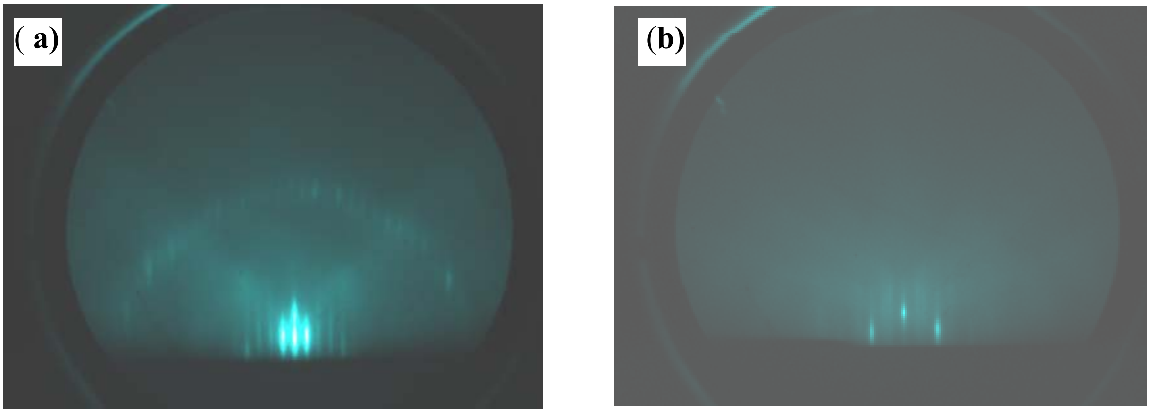

Figure 2.2: RHEED image of a) 4x along [100] in Sb-rich c(4x4) surface reconstruction and b) '3x' along $[1\bar{1}0]$ in In-rich '1x3' reconstruction during the growth of an InSb layer.

Growth rates can also be calibrated using RHEED. As the growth proceeds, the peak intensity of the specular beam which oscillates during growth, is monitored as a function of time. One period of oscillation period corresponds to the time needed for a monolayer growth. When the layer is smooth, the intensity is maximum. As more atoms are deposited, the surface is less smooth since islands are formed. With maximum roughness on the surface, the intensity is at a minimum. With time, islands grow and coalesce with adjacent islands to form a complete layer, causing the next intensity maximum.

a) Ga Incorporation Rate

The Ga incorporation rate is measured on a GaAs surface. First, a GaAs layer is grown on a GaAs (001) substrate at a temperature 20 ^{0}C above the oxide desorption temperature. The surface reconstruction during the growth is (2x4). Group-III incorporation rates are calibrated in a Group-V-rich environment. Ga-induced oscillations are observed as shown in Figure 2.3 (a).

b) As Incorporation Rate

The incorporation rate for As is measured on a GaAs surface. First, the Ga shutter is opened for a few seconds to deposit ~10 monolayers of Ga. Then the Ga shutter is closed and the As shutter is opened immediately. Group V incorporation rates are calibrated on Group III-rich surfaces. The oscillations observed are shown in Figure 2.3 (b).

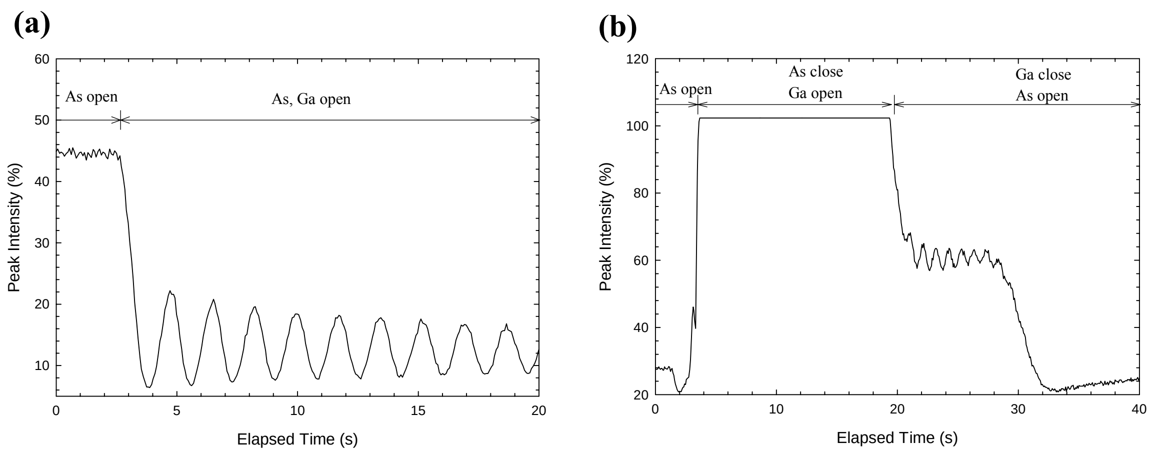

Figure 2.3: a) Ga- induced and b) As-induced RHEED intensity oscillations.

c) Al Incorporation Rate

The incorporation rate of Al is measured on a GaAs surface. The temperature of the As source is such that its beam flux pressure is more than that of Al. The As shutter is kept open and the Al shutter is opened to grow 8-10 monolayers of AlAs. As Al on the surface is prone to attract impurities, a few monolayers of GaAs are grown after closing the Al shutter. Figure 2.4 shows the typical Al-induced RHEED intensity oscillations. Using the Al and In incorporation rates, the rate of AlInSb can be deduced.

d) In Incorporation Rate

The calibration of growth rates for GaAs(001) can be done on a (2x4) surface at varying substrate temperatures and for a range of growth fluxes. On the other hand, it has been seen that the calibration of In and Sb incorporation rates on an InSb surface can be done only in a narrow range of substrate temperature and fluxes. This makes the calibration on InSb using RHEED oscillations difficult. To calibrate In, first ~1 μm of InSb is grown on GaAs substrate. As the temperature of the substrate is decreased below a certain temperature, the surface reconstructions of InSb changes from In-rich '1x3' to Sb-rich c(4x4). This transition temperature, T_{tr}, is ~390 ^{o}C. The temperature of the substrate is decreased nearly 25 ^{0}C below the T_{tr}. The In and Sb shutters are opened to grow 8-10 monolayers of InSb. The In-induced oscillations are shown in Figure 2.5 (a).

e) Sb Incorporation Rate

The growth rate of Sb is calibrated in an In-rich environment when the substrate temperature is nearly T_{tr} – 25 ^{0}C. First, the Sb shutter is closed and the In shutter is opened to deposit 8-10 monolayers of In. Then, the In shutter is closed and the Sb shutter is opened. Sb-induced oscillations are seen in Figure 2.5 (b).

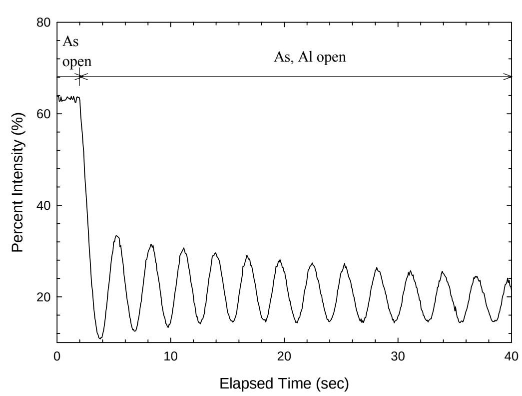

Figure 2.4: Al- induced RHEED intensity oscillations.

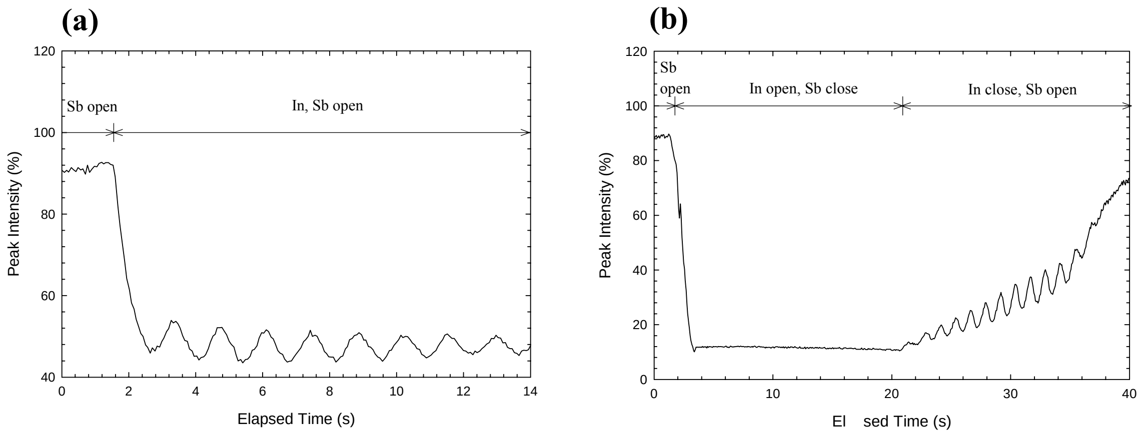

Figure 2.5: a) In- induced and b) Sb-induced RHEED intensity oscillations.

2.5 InSb Quantum Well

Among all binary III-V semiconductors, InSb has the highest intrinsic electron mobility, the narrowest band gap, and the smallest electron effective mass. These characteristics make InSb quantum wells (QWs) with remotely doped $Al_xIn_{1-x}Sb$ barriers promising for several novel devices. Mesoscopic magnetoresistors that take advantage of the high electron mobility in InSb QWs at room temperature are currently being developed for read head applications [15, see Ch. 5]. The promise of InSb QWs for spin transistors has been shown recently by experiments that demonstrate a large zero-field spin splitting [16, see Ch. 5] and ballistic transport at temperatures as high as 200 K [17, see Ch. 3].

2.5.1 Typical Layer Structure of InSb Quantum Well

Semi-insulating GaAs is used as a substrate material in spite of the large lattice mismatch (~14.6%). The single quantum-well structure, with $Al_xIn_{1-x}Sb$ barrier layers, is grown on GaAs (001) substrates [18]. Two typical layer sequence are shown in Figure 2.6.

The AlSb and the first AlInSb layer are grown at substrate temperatures ~100 ^{0}C and 300 ^{0}C respectively, below the oxide desorption temperature of GaAs substrate. The

AlInSb surface reconstruction during growth is typically '1x3'. After growing ~1 μm of AlInSb, growth is paused and the substrate temperature is decreased to measure the transition temperature of AlInSb surface reconstruction to c(4x4). The substrate temperature is then raised 40 ^{0}C above the transition temperature and further growth of superlattice and 2 μm AlInSb is initiated. All buffer layers (layers below the first Si δ-doped layer), except the strained-layer superlattice, are expected to be almost fully relaxed due to their large thicknesses. After the buffer layers, the strained quantum well structures, shown in Figure 2.6, are grown at 370 ^{0}C. This low substrate temperature is used in order to suppress migration of Si atoms from the δ-doped layers [19]. The two Si-δ-doped layers near the well provide electrons to the quantum well and the one near the surface provides electrons to the surface states. The strained quantum wells are thin enough to be below the expected critical thickness [20]. The electron density in the well can be changed by changing the composition and thickness of AlInSb barrier layers. The conduction band edge diagrams for these samples, with well width 20 nm and 25 nm respectively, are shown in Figure 2.7.

2.5.2 Typical Mobility and Density

Mobility and density as functions of temperature are shown in Figure 2.8 for an InSb quantum well structure. The measurements were performed in a closed cycle Helium refrigerator with a maximum magnetic field of ~0.1 T. The temperature is varied from 300 to 7 K. The mobility and density show a temperature dependence that is typical of remotely doped quantum wells. The Hall data for a few of our good samples, where only the first subband is occupied, is given in Appendix 2. The typical 4.2 K Hall resistance and longitudinal resistance in an InSb/AlInSb quantum well without any parallel conduction, are shown in Figure 1.2 and Figure 2.9.

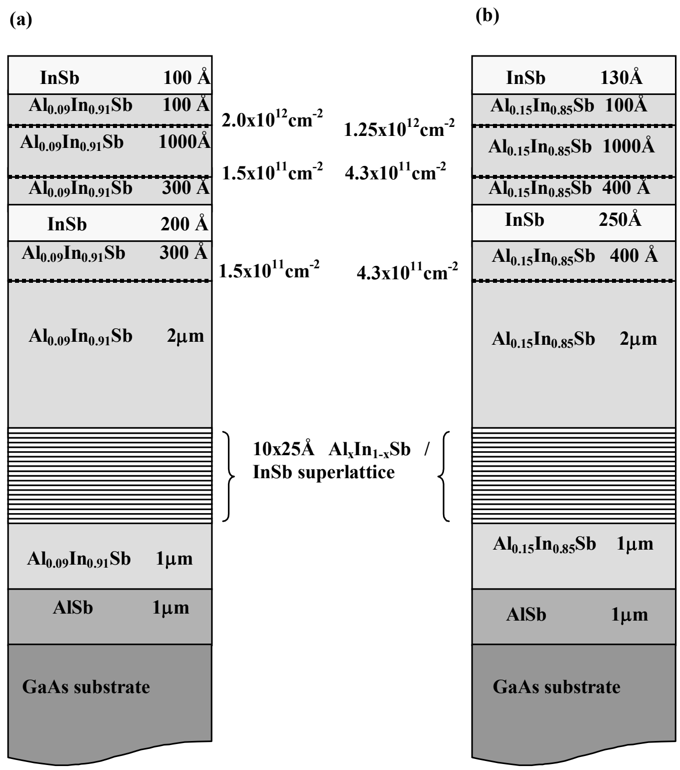

Figure 2.6: The layer structure of InSb quantum wells with $Al_xIn_{1-x}Sb$ barriers, where $x = 0.09$ (sample s697) and $x = 0.15$ (sample s842). The dotted lines represent Si-δ-doped layers with densities as indicated in the figure.

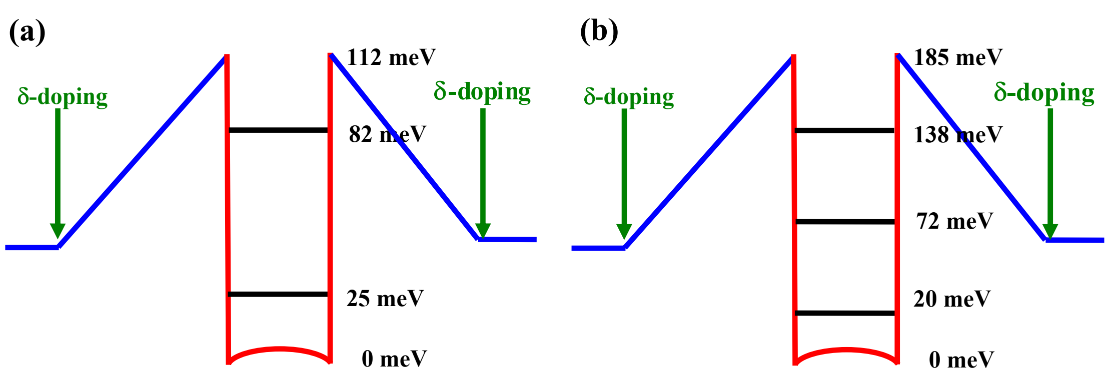

Figure 2.7: The conduction band diagram for a) s697 and b) s842 with non-parabolicity taken into account.

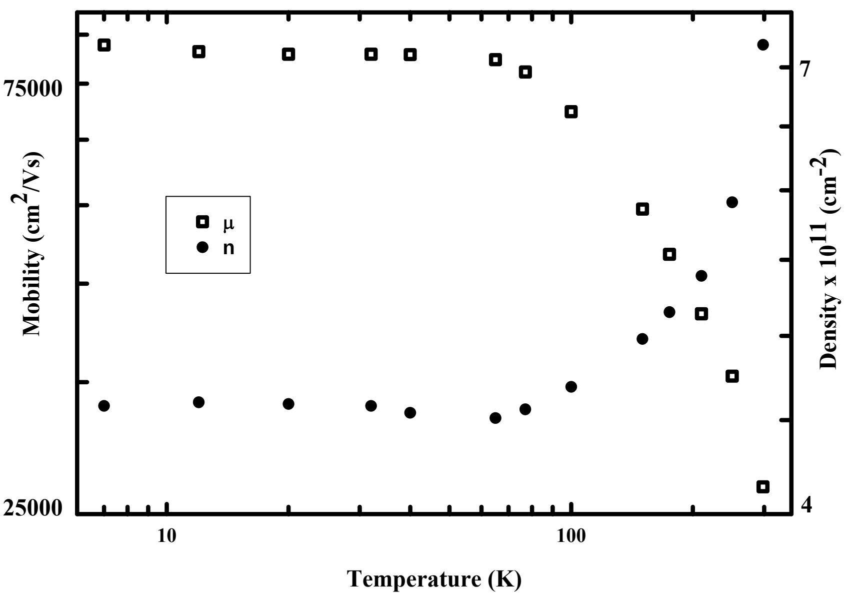

Figure 2.8: Mobility (square) and density (filled circle) as functions of temperature in a 5mm x 5mm square piece of s842.

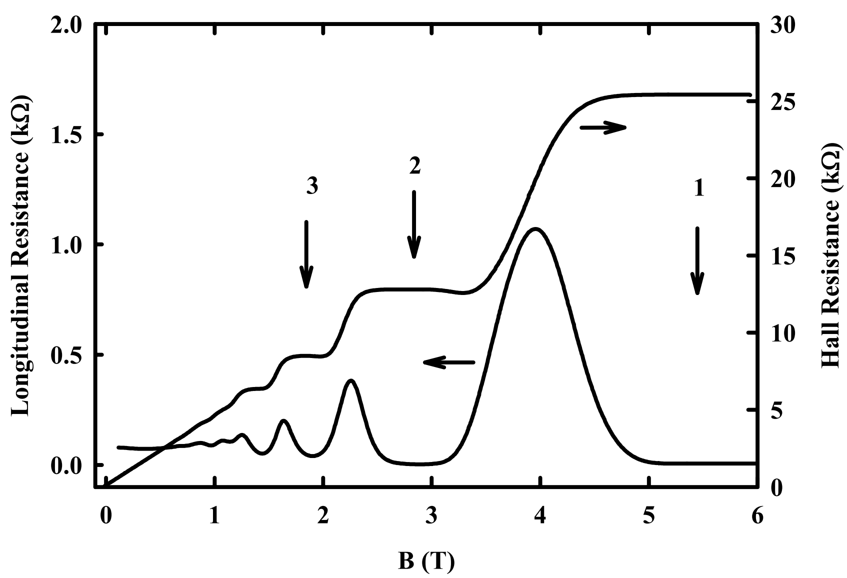

Figure 2.9: Hall resistance and longitudinal resistance for s704 (20 nm wide well and 30 nm wide $Al_{0.09}In_{0.91}Sb$ barriers) with van der Pauw geometry at 4.2 K. The density and mobility of electrons in the quantum well are *1.33* x *10^{11} cm^{-2}* and *170,000 cm^2/Vs* respectively.

2.6 Structural Defects in InSb Quantum Well

One drawback in using InSb-based structures for electronic devices is that there are no lattice matched III-V insulators to serve as barrier and substrate materials. Earlier studies have shown that $Al_xIn_{1-x}Sb$ layers, which have <1% lattice mismatch for $x < 0.2$, are effective as barrier layers for low temperature applications [21]. However, they can conduct significantly at room temperature due to intrinsic electrons if x is not sufficiently large [18]. Conduction through the $Al_{0.09}In_{0.91}Sb$ barrier layers is thought to limit the room temperature performance of magnetoresistors [15] and ballistic transport devices [17]. Structural defects in our InSb quantum well have been investigated by J.C. Keay and M.A. Ball using AFM [22,23] and by T.D. Mishima using TEM [24, 25]. Their results are summarized concisely in the following sections.

2.6.1 Results and Discussion

a) AFM Measurements

Figure 2.10 (a) shows an AFM image of the surface of an InSb QW sample. This image is characterized with two features: 1) round-top protrusive features seen at, e.g., A and B in the figure, which are categorized as hillocks [22, 23], and 2) line features along the [110] and $[\bar{1}10]$ directions, which are named oriented abrupt steps, OASs [22, 23]. A third type of defect, square mounds [22, 23], is observed as shown in this image. The OASs have an anisotropic density: the $[\bar{1}10]$-oriented OASs are more numerous than the [110]-oriented ones. Morphological similarity between the hillocks and spiral features observed on a GaSb epilayer grown on a GaAs (001) substrate [22] suggests that a hillock may be formed with a threading dislocation at its core [22, 23].

Shown in Figure 2.10 (b) is the height profile along line C-D which goes across an OAS. One can see that the OAS has an inclination angle of ~12° with respect to the (001) surface. Such height profile measurements show that the inclination angles of the OASs of the sample are, on average, ~10.9°.

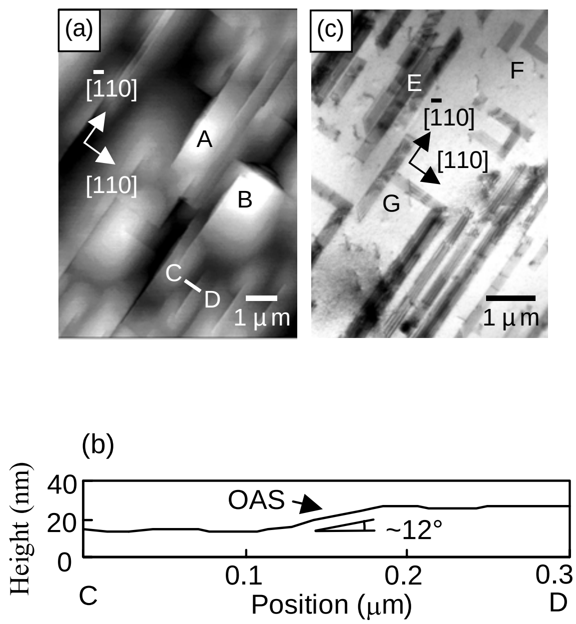

Figure 2.10: a) AFM image of an InSb quantum well sample with hillocks (eg. A and B) and oriented abrupt steps (OASs). b) Height profile along line C-D, which crosses an OAS. The inclination angle of the OAS is measured to be ~12^0. c) Plan-view TEM image of the sample. Rectangular contrasts are derived from {111}-planar defects.

b) TEM Measurements

Figure 2.11 shows a representative two-beam 220 dark-field (DF) cross sectional TEM (X-TEM) image taken from a $[\bar{1}\,\bar{1}\,0]$ cross-sectional specimen. Two types of defects can be seen: (1) dislocations that appear as thin bent lines and (2) (111)- and $(\bar{1}\,\bar{1}\,1)$ -planar defects that appear as thick straight lines at an angle of 54.7^0 with respect to the substrate surface. The first InSb/$Al_{0.09}In_{0.91}Sb$ interface (labeled A in Fig. 2.11) traps many dislocations, which then form a bundle of dislocations along that interface. The (111)- and $(\bar{1}\bar{1}1)$-planar defects are introduced at many locations, including the InSb/GaAs interface, the first InSb/ $Al_{0.09}In_{0.91}Sb$ interface, the SLS, and the thick $Al_{0.09}In_{0.91}Sb$ layer. When (111)- and $(\bar{1}\bar{1}1)$-planar defects encounter each other, one of the two planar defects tends to be blocked while the other propagates toward the sample surface.

In Figure 2.10 (c), the top edge of the micro-twin is inclined by ~12° with respect to the (001) surface. On average, the inclination angles are ~10.7°. The excellent agreement in inclination angles (~10.9° for the OASs and ~10.7° for the micro-twins) indicates that OASs are the terminal edges of micro-twins at the sample surface. The OASs and micro-twins have a density of $\sim 5 \times 10^7 - 1 \times 10^8\ /cm^2$ and an anisotropic density ratio ($[\bar{1}10]/[110]$) of ~5.8.

Figure 2.12 (a) and (b) are 200 DF X-TEM images of a micro-twin propagating through a QW. It is apparent that there is an offset between the parts of the QW on each side of the micro-twin. The angle between a line connecting the edges of the two parts (points labeled A and B in Figure 2.12 (a)) and the (001) surface of the substrate is ~16°. The same angle is seen for all the crossings of a micro-twin and a QW that we observe. This angle coincides with the angle between the {111} surface of micro-twins and the (001) surface of the substrate. As shown in Figure 2.12 (b), the QW on the upper side is slightly inclined until it is ~0.4 μm away from the micro-twin. The inclined region may be formed by vicinal interfaces or by lattice bending.

Figure 2.13 (a) and (b) are two-beam 220 and $\bar{2}20$ DF TEM images, respectively, taken for the same area of a plan-view specimen. Two of the four equivalent types of

{111}-micro-twins can be seen in each image: (111)- and $(\bar{1}\bar{1}1)$-micro-twins are seen as rectangular features in Figure 2.13 (a), and $(\bar{1}11)$- and $(1\bar{1}1)$-micro-twins are seen in Figure 2.13 (b).

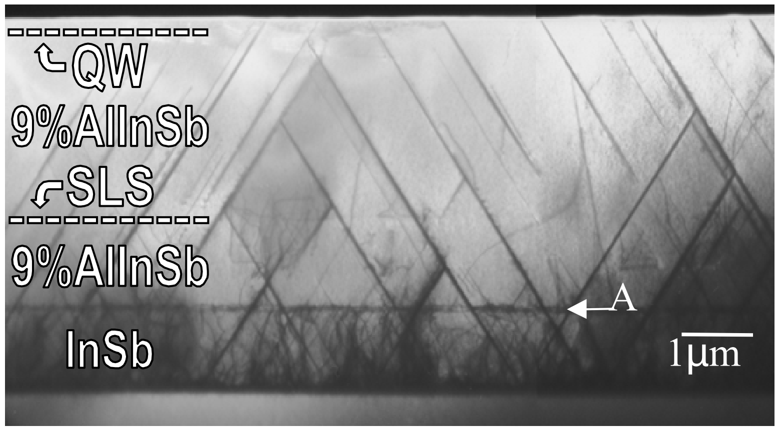

Figure 2.11: 220 DF X-TEM image taken from a $[\bar{1}10]$ cross sectional specimen. Label A indicates the first InSb/$Al_{0.09}In_{0.91}Sb$ interface from the GaAs substrate.

Within the rectangular features, there are regions with different patterns and contrasts. This is due to {111}-bilayer thickness (0.37 nm) differences, or equivalently, different numbers of overlapping stacking faults [26]. By comparing Figure 2.13 (a) and (b), one can see that partial dislocations are located at the boundaries of the regions, although dislocations that are not trapped by micro-twins are also seen. It is apparent that more micro-twins are aligned along the $[\bar{1}10]$ direction than along the [110] direction: the length densities of the micro-twins are 0.22 μm^{-1} in the [110] direction and 1.37 μm^{-1} in the $[\bar{1}10]$ direction, which yields a ratio $([\bar{1}10]/[110])$ of ~5.7.

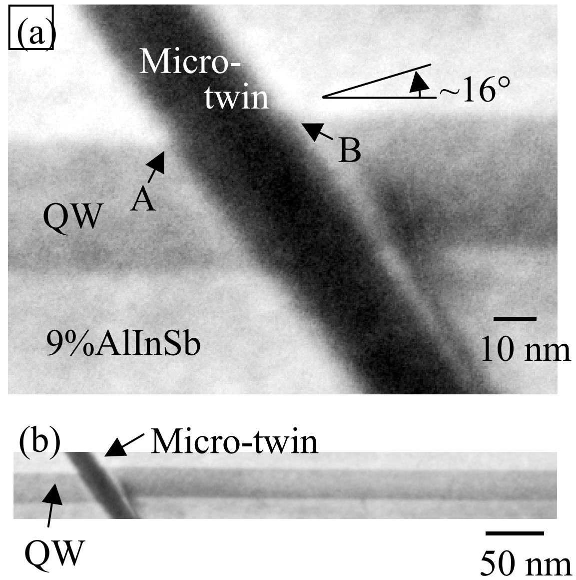

Figure 2.12: a) 200 DF X-TEM image for the crossing of a micro-twin and a QW. The image was taken from near the <110> direction of a [100] cross-sectional specimen. Dislocation contrast also can be seen on the right side of the micro-twin. b) A wider area view of the micro-twin and QW. The part of the QW on the right side of the micro-twin is slightly tilted.

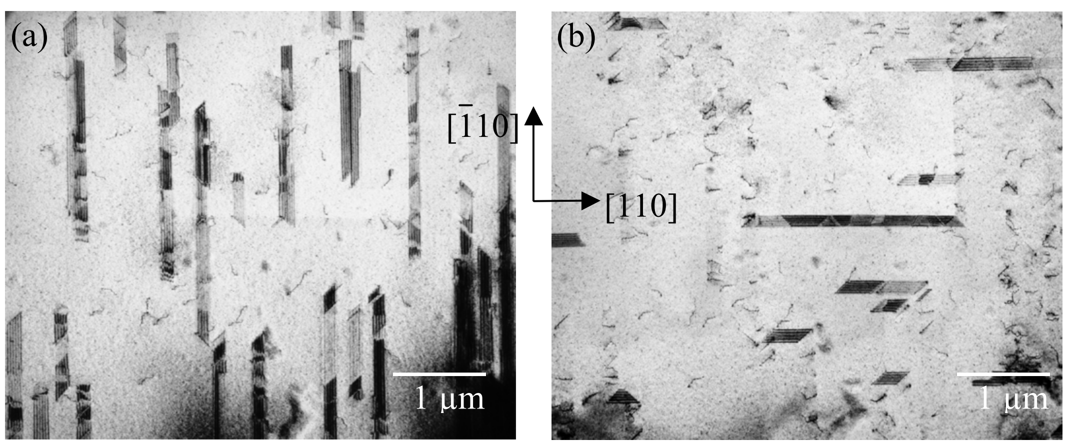

Figure 2.13: (a) 220 and (b) $\bar{2}20$ DF plan-view TEM images. Micro-twins yield a rectangular contrast. The contrasts of dislocations are visible.

Our TEM observations suggest several mechanisms for electron scattering in the QW due to micro-twins. First, because of the difference in crystallographic orientation between the micro-twin and matrix regions, electrons passing through micro-twins can be reflected and diffracted. Secondly, the dislocations trapped by micro-twins can scatter electrons in the QW. The correlation between a highly asymmetric-dislocation density and anisotropic electron mobility has been reported for $In_{0.2}Ga_{0.8}As$ QWs [27]. Thirdly, chain-like scattering potentials formed by atomic steps on the vicinal interfaces located near micro-twins [28] and at the micro-twin/matrix boundaries can be scattering sources.

c) Mobility and Density

The mobility and carrier density of the sample are shown in Figure 2.14. When current is passed along the $[\bar{1}10]$ direction, the mobility shows a temperature dependence that is typical of remotely doped quantum wells. In contrast, the mobility at low temperature is much lower when current is passed along the [110] direction and does not show strong temperature dependence. The degree of mobility anisotropy varies among samples and depends on the buffer layer composition and growth parameters.

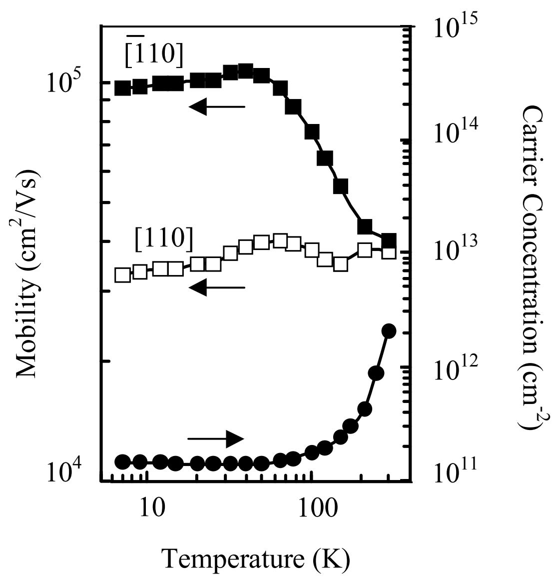

Figure 2.14: Measured electron density and mobilities in an InSb/$Al_{0.09}In_{0.91}Sb$ quantum well structure grown on a GaAs substrate. The $[\bar{1}10]$ and [110] labels indicate the direction of current flow during the measurement.

In the temperature range between 7 and 20 K where phonon scattering has a negligible contribution, the mobilities are somewhat constant and have values of ~*3.4* x 10^4 and ~*9.8* x 10^4 cm^2/Vs in the [110] and $[\bar{1}10]$ directions, respectively, with a carrier density of *1.46* x 10^{11} cm^{-2}. This mobility difference correlates with the density of OASs: in the [110] ($[\bar{1}10]$) direction, the mobility is lower (higher) and there is a higher (lower) density of OASs normal to the direction. The identical correlation has also been reported for other InSb QW samples [18]. The results of this study indicate that the origin of the correlation can be understood with the existence of the micro-twins. Micro-twins induce other structural defects in InSb QWs, such as offset and bending of the QWs, and the density of the micro-twins is correlated with the electron mobility in the QWs.

From Figure 2.14 , the ratio of the mobilities at low temperature, $\mu_{[\bar{1}10]} / \mu_{[110]} \approx 3.0$, and the elastic mean free path for each direction, 0.57 μm and 0.19 μm for current along the $[\bar{1}10]$and [110] directions, respectively can be calculated. Since the mean free paths are a similar order of magnitude to the average distance between micro-twins, scattering due to the micro-twins is expected to contribute significantly to limiting mobility. The lower density of micro-twins encountered by electrons moving along the $[\bar{1}10]$ direction implies that electron mobility in the $[\bar{1}10]$ direction should be larger, in agreement with the mobility measurements. The electron mobility ratio is smaller than the micro-twin density ratio. However, this discrepancy can be explained by the presence of additional scattering mechanisms with a different degree of anisotropy. It is known that scattering by ionized background impurities, remote ionized donors, interface-roughness [29], and dislocations [27] affect the mobility of electrons in remotely doped QWs.

2.7 Optimization of Layer Structure

2.7.1 Buffer Layers

It has been shown earlier that the buffer layers can have an important effect on the microtwin density [12]. The microtwin density has been reported earlier to decrease if 920 nm thick InSb layer in the sequence is replaced with AlSb (1 μm) layer [13]. Moreover, replacing the superlattice structure in the buffer layer sequence with 0.2 μm wide InSb interlayer, decreases the micro twin density by an order of magnitude [12]. Although this indicates that InSb acts as a good dislocation filter, this layer may act as a parallel conducting path at room temperature. The intrinsic carriers in InSb layer ($n = 2 \times 10^{16}\ cm^{-3}$) can be a source of leakage through this structure.

The similar effect of dislocation bending at the interface of InSb interlayer and the AlInSb buffer layer can also be achieved by replacing the InSb with AlInSb interlayer. The lattice constant difference between InSb and underlying AlInSb buffer layer should be maintained between the AlInSb interlayer and underlying alloy layer. For this the interlayer should have a higher Al concentration than that in the buffer layer. In order to further study the effect of the buffer layer composition on mobility of these structures, three types of quantum wells with slightly different buffer layers sequences were grown. The layer structure for two of these samples is given in Figure 2.15. The buffer layers AlSb and $Al_{0.12}In_{0.88}Sb$, one micron each, were grown on GaAs substrate. Next either a 10 x 25 Å InSb/ 25 Å $Al_{0.12}In_{0.88}Sb$ superlattice (sample 1: s940, Figure 2.15 a) or 0.2 μm $Al_{0.24}In_{0.76}Sb$ interlayer (sample 2: s936, Figure 2.15 b) were grown followed by 2 μm $Al_{0.12}In_{0.88}Sb$ layer. A third type of sample with similar layer structure as sample 2 but with

1 μm thick top buffer alloy layer instead of 2 μm (sample 3: s943, layer structure not shown) was also grown. The doping density along with the thickness and composition of the active region and cap layers were kept same in all the three samples. Hall measurements on a sample of van der Pauw geometry for variable temperature (300 to 12 K) are shown in Figure 2.16. The density and mobility in the three samples are compared. Hall measurements at 4.2 K in a ^{4}He cryostat for the three samples give mobility of about *98,000 cm²/Vs* for sample 1; *200,000 cm²/Vs* for sample 2 and *140,000 cm²/Vs* for sample 3.

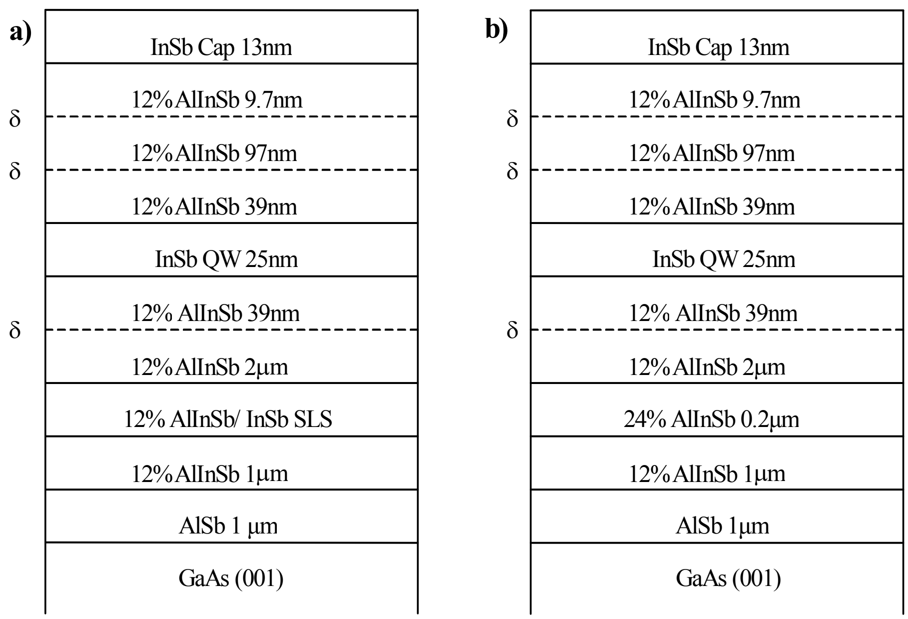

Figure 2.15: Layer structure for $Al_{0.12}In_{0.88}Sb$ / InSb single quantum well a) with superlattice (s940) or b) $Al_{0.24}In_{0.76}Sb$ interlayer (s936) as dislocation filter.

The improvement in low temperature value of mobility for sample 2 compared to sample 1 indicates that the alloy layer with higher Al concentration may be decreasing the defects propagating towards the quantum well. Moreover, decreasing the thickness of the upper buffer alloy layer decreases the low temperature mobility indicating the influence of possible defects propagation to the well region. The mobility for sample 3 was still better than the structure with superlattice. There was no significant improvement in the room temperature mobility in s936 or s943. To check the possible relation between the defect density on the mobility of these samples, TEM measurements are underway.

2.7.2 Delta Doped Layers

The effect of changing the doping density near the well and the surface can be seen in Table 2.1. The result of variable temperature Hall measurements on van der Pauw samples is shown in Figure 2.17. Sample s937, s944, s945 and s946 were grown with layer structure similar to s936 but with different density in Si-δ-doped layers. On decreasing the doping density near the well (s944) compared to that in s936, the average density at room temperature increases and the average mobility at 300 K decreases. The sample s944 is depleted below 175 K. This may indicate that the decrease in the doping density near the well has decreased the carrier density in the well. As a result, contribution to the average mobility and density by the higher mobility carrier has decreased at room temperature.

In order to see the effect of the change in surface delta doped layer, the doping density in Si-δ-layer near the surface is reduced in s937. The average density decreases and the average mobility increases considerably indicating that the doping near the surface may be the primary source of leakage path through these structures at room temperature. This may suggest the possibility of significant decrease in parallel conduction at 300 K. As the doping density near the well is kept constant in s937 and s945, the density in the well decreases at lower temperature whereas there is no significant change in the room temperature average values. The density in s945 at low temperature is lower than that in s937 implying we may have started to decrease the density in the well as the carriers in the dopants near the well may now be required to satisfy the surface states. The trend continues in s946. The mobility of *36,000* cm^2/Vs at room temperature and *200,000* cm^2/Vs at 4.2 K are among the highest values so far obtained for InSb/AlInSb single quantum well samples. There is sign of slight parallel conduction at 4.2 K in samples s939, s940 and s943. Further measurements of Hall and longitudinal resistance in a few of the samples listed in Table 2.1 are underway to estimate the density and mobility of carriers at higher temperatures using QMSA.

For a few of these samples, anisotropy in the longitudinal resistance in two perpendicular directions was observed at zero magnetic field, indicating the anisotropic mobility in the two directions. The numbers given in Table 2.1 are the average numbers for the two directions. Experiments on L-shaped Hall bars are underway to study the anisotropy in these samples.

Sample	SLS or $Al_{0.24}In_{0.76}Sb$	Upper+Lower $Al_{0.12}In_{0.88}Sb$	n_δ near well (each side)	n_δ near surface	n_{300K}	$n_{4.2K}$	μ_{300K}	$\mu_{4.2K}$
		μm	x 10^{11} cm^{-2}				x 10^4 cm^2/Vs	
S936	$Al_{0.24}In_{0.76}Sb$	2+1	5	11	9.6	4.1	2.7	20
S940	SLS	2+1	5	11	10	4	2.3	7.9
S943	$Al_{0.24}In_{0.76}Sb$	1+1	5	11	9.7	3.9	2.6	14
S944	$Al_{0.24}In_{0.76}Sb$	2+1	2	11	11.7	deplete	1.9	deplete
S937	$Al_{0.24}In_{0.76}Sb$	2+1	4	8	5.9	4	3.5	16
S945	$Al_{0.24}In_{0.76}Sb$	2+1	4	4	5.7	3.5	3.4	9.3
S946	$Al_{0.24}In_{0.76}Sb$	2+1	3	2	4.2	2.6	3.6	9

Table 2.1: The comparison in average Hall mobility and average Hall density at room temperature for a few single quantum well samples.

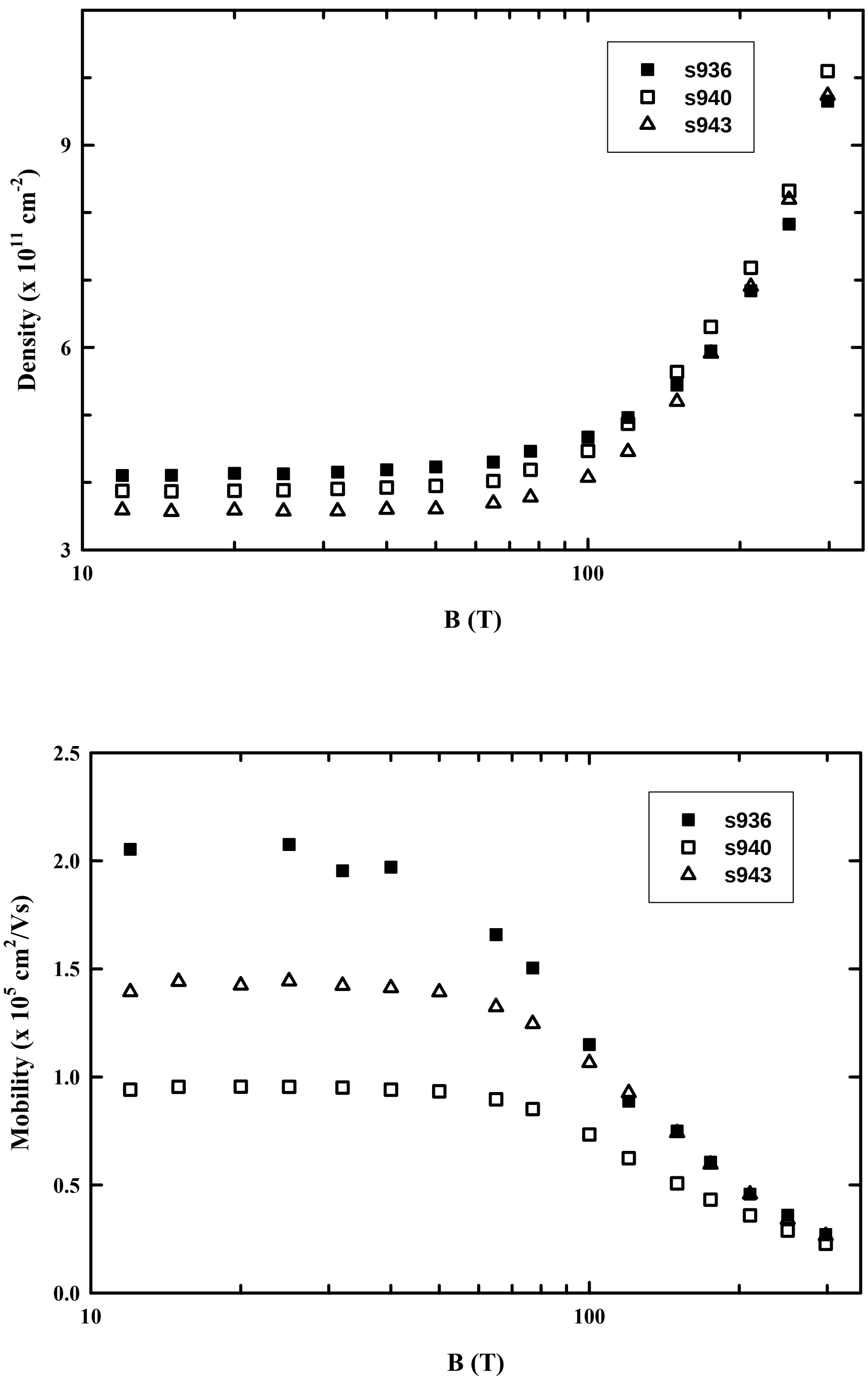

Figure 2.16: a) Density and b) mobility at temperatures ranging from 300 to 12 K for samples s936, s940 and s943 are compared.

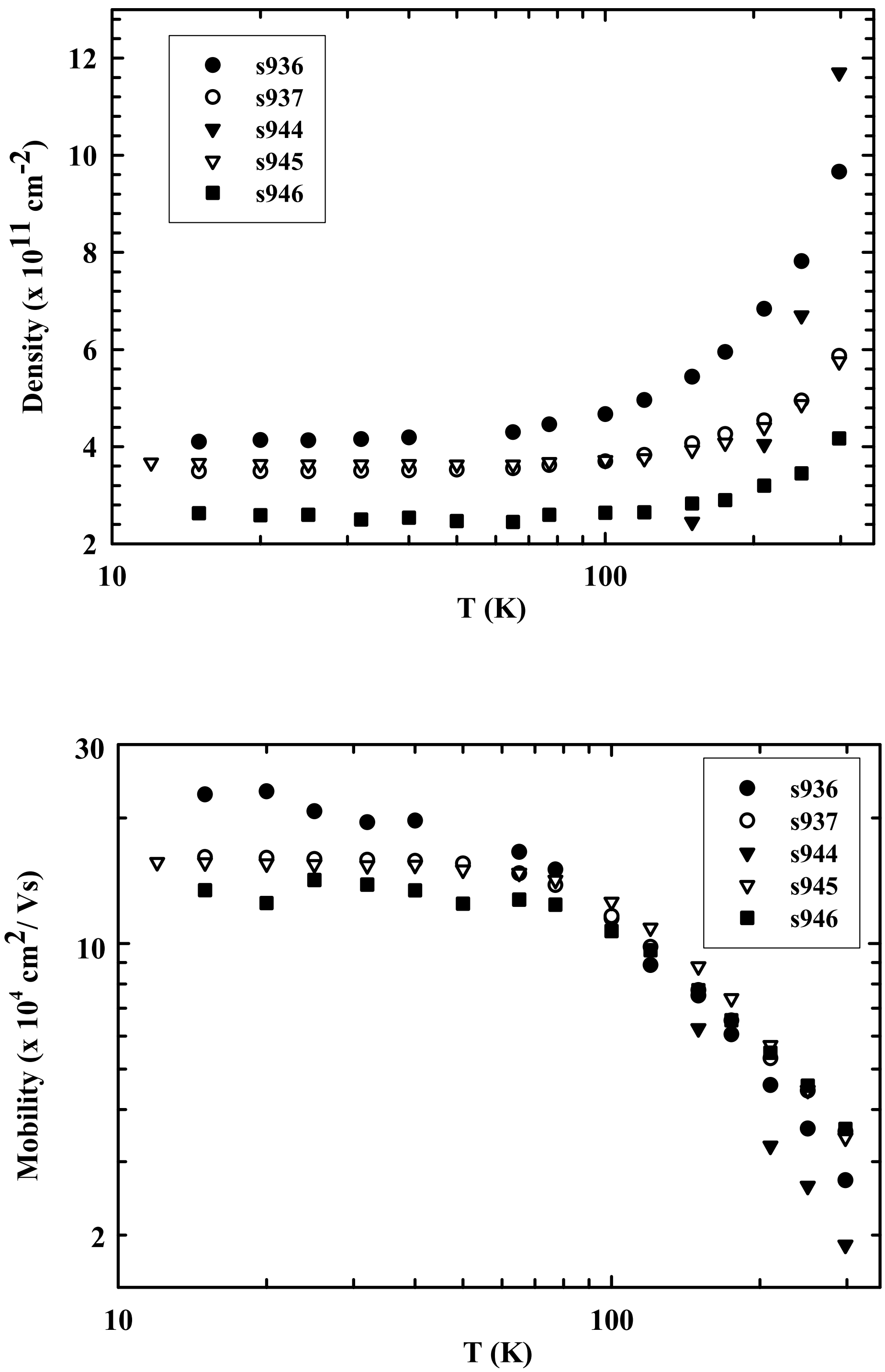

Figure 2.17: Density and mobility as functions of temperature for a few samples.

Chapter 3
BALLISTIC TRANSPORT:NEGATIVE BEND RESISTANCE

There is a growing interest in devices like spin transistors [30], in which transport through the channel is ballistic. In some of the proposed spin devices, the signal depends strongly on the electron's path length. All electrons should have the same path length for the sharpest signal. Since the spin coherence length in semiconductors can be much longer than the electron mean free path, l_e [31,32], the channel length of the spin FETs are limited by l_e. If l_e in the system is less than the channel length of the sample, then the transport is diffusive. As the dimension of the system is decreased such that the channel length is equal to or less than l_e, scattering due to the boundary of the system affects the transport of the electrons. This is the ballistic regime. Therefore, the performance of these devices depends critically on the degree to which electron transport occurs without large-angle scattering.

The amount of large-angle scattering can be characterized by measuring the so-called bend resistance. A negative bend resistance (which is characteristic of ballistic transport) has been observed at temperatures up to 100 K in AlGaAs/GaAs mesoscopic structures [33,34]. For practical purposes, the spin FET should be able to function at room temperature. Since mobility is more strongly affected by large-angle scattering than small-angle scattering, materials with a high mobility mean free path ($l_e = (h\mu/e)(n/2\pi)^{1/2}$ where μ is the mobility and n is the electron density) should exhibit a stronger bend resistance. Negative bend resistance (NBR) has been observed up to room temperature for a structure fabricated in the AlGaAs/InGaAs/GaAs system, where μ = *7,800* cm^2/Vs, n = *1.1* x 10^{12} cm^{-2}, and l_e=*0.13* μm [35].

The smaller effective mass of electrons in InSb and the higher room temperature mobility may enable ballistic transport at room temperature. This chapter reports results obtained from ballistic transport measurements performed on four-terminal structures fabricated from InSb/$Al_xIn_{1-x}Sb$ (x = *0.09, 0.15*) single quantum wells. Our data are the first demonstration of ballistic transport in InSb quantum wells. The dependence on device size, barrier height and temperature is studied. Observation of ballistic transport at higher temperatures may be obscured by the leakage through the structure. Therefore, the parallel conduction in the samples is estimated using the quantitative mobility spectrum analysis technique.

3.1 Ballistic Transport: Literature Overview

If the channel length is much larger than l_e, transport through the channel is diffusive. Transport is ballistic when the size of the sample is less than l_e, and the scattering from the boundaries of the device limit the current. Many groups have reported magnetoresistance anomalies like quenching of the Hall effect [36, 37], last Hall plateau [36, 37, 38, 39], negative Hall resistance [37], and bend resistance [40, 41, 42] in narrow Hall bars.

The bend resistance of a cross junction is found by passing current through two adjacent terminals and measuring the voltage across the other two terminals. In the absence of an applied magnetic field, a large percentage of the ballistic electrons will accumulate in the voltage terminal located opposite from the current-injection terminal. The sign of the measured voltage indicates whether the majority of electrons are moving ballistically or diffusively. A negative bend resistance (the measured voltage divided by the injected current) is a characteristic of ballistic transport. As B increases, the Lorentz force bends the trajectory of the electrons.

The bend resistance is strongly dependent on the shape of the junction. The rounding of the junction collimates the electron beam [43]. The positive overshoot in R_B at low B for rounded corners, has been reported experimentally [33] and theoretically [44]. The effect was not seen in the calculations done for straight corner junctions [45].

The Hall resistance of a cross junction (four-terminal) is found by passing current through two opposite terminals and measuring the voltage across the other two terminals. At very small B, if an electron is reflected by the side junction and if the geometry of the junction is such that there is a higher probability for electron to be reflected in the region many times, then there is an equal probability for the electron to enter the left or the right probe. The Hall voltage is suppressed and is called quenching of the Hall effect [46]. Due to the geometry of the junction, negative Hall resistance can be seen too [37]. As B is increased, the field guides the electron around the corner. If the cyclotron radius, r_c, becomes smaller than the radius of the curvature of the corner, there is no longer any backscattering of the electrons. In the absence of backscattering, the longitudinal resistance vanishes and the Hall resistance becomes equal to the contact resistance. As long as the B-field is such that the cyclotron diameter, d_c, is greater than the channel width W, the contact resistance is independent of the magnetic field. This leads to the observation of the last Hall plateau [46]. These magnetoresistance anomalies disappear at higher temperatures. The inelastic scattering causes a transition to the diffusive transport regime.

Quantized conductance [see Ch 4], another signature of ballistic transport, has been observed up to 30 K in the AlGaAs/GaAs system [47]. Quantized conductance is related to 1D subbands and disappears if the subbands are not resolved due to thermal broadening. NBR, on the other hand, is independent of subband parameters but depends on the size of the device as compared to l_e. In AlGaAs/GaAs mesoscopic structures of length 0.3 μm, the bend resistance has been observed up to 100 K [33, 34]. The negative peak in bend resistance has been observed in four terminal structures can be explained using the Landauer-Büttiker formula [48], from which the ballistic length, l_b, can be calculated. Initially, l_b was reported to be smaller than l_e in a 2DES [49] due to diffusive boundary scattering. Later due to the development of high mobility heterostructures, l_e improved to ~100 μm [50]. As a result, ballistic devices can be fabricated by photolithography. The ballistic transport in relatively large four-terminal devices (10-210 μm) has been observed [51, 52]. Using the Landauer-Büttiker formula, l_b as a function of the electron density has been studied in these structures and was found to compare well with l_e, which depends on electron density and mobility [52].

NBR has also been observed up to room temperature for structure with $W = 260\ nm$ in the AlGaAs/InGaAs/GaAs system [35]. Since the room temperature electron mobility is higher in AlGaAs/InGaAs/GaAs than that in a conventional AlGaAs/GaAs modulation doped structure, NBR is expected to persist to higher temperatures. Moreover, the density of electrons in the AlGaAs/InGaAs/GaAs system can be nearly $10^{12}\ cm^{-2}$. As a result, the rounding of the edges of the etched lines of the junction, due to depletion spreading is reduced. High carrier density and high mobility increase l_e. Therefore, it is possible to make smaller structures with this material system.

InSb has the smallest effective mass and the highest room-temperature intrinsic electron mobility of all binary III-V semiconductors. This may enable the ballistic transport to persist up to higher temperatures. We have observed ballistic transport in Si-δ-doped InSb/$Al_xIn_{1-x}Sb$ quantum well structures [17, 53] at temperatures up to 205 K, which we report in this chapter.

3.2 Layer Structure

Two single quantum-well structures (s697, s842), with $Al_xIn_{1-x}Sb$ barrier layers ($x = 0.09, 0.15$), were grown on semi insulating GaAs (001) substrate. The layer sequence above the GaAs substrate for the two samples is shown in Figure 2.6. For characterizing the mobility and density of the quantum-well structures, Hall bar devices with channel widths of 50 μm were defined through photolithography and chemical etching.

The longitudinal resistance and the transverse (Hall) resistance at ~1.5 K for both the samples are given in Figure 3.1. The density and mobility for the InSb/ $Al_{0.09}In_{0.91}Sb$ quantum well at 1.65 K are $2.4 \times 10^{11}\ cm^{-2}$ and $1.1 \times 10^{5}\ cm^{2}/Vs$. The density and mobility for InSb/ $Al_{0.15}In_{0.85}Sb$ quantum well at 1.5 K are $4.1 \times 10^{11}\ cm^{-2}$ and $8 \times 10^{4}\ cm^{2}/Vs$. We deduce a mobility mean free path of $\ell_e = \hbar(\sqrt{2\pi n})\mu / e = 0.84 \mu m$ from the measured mobility and density of 50 μm wide Hall bars at 1.65 K and 1.5 K respectively, for both the samples.

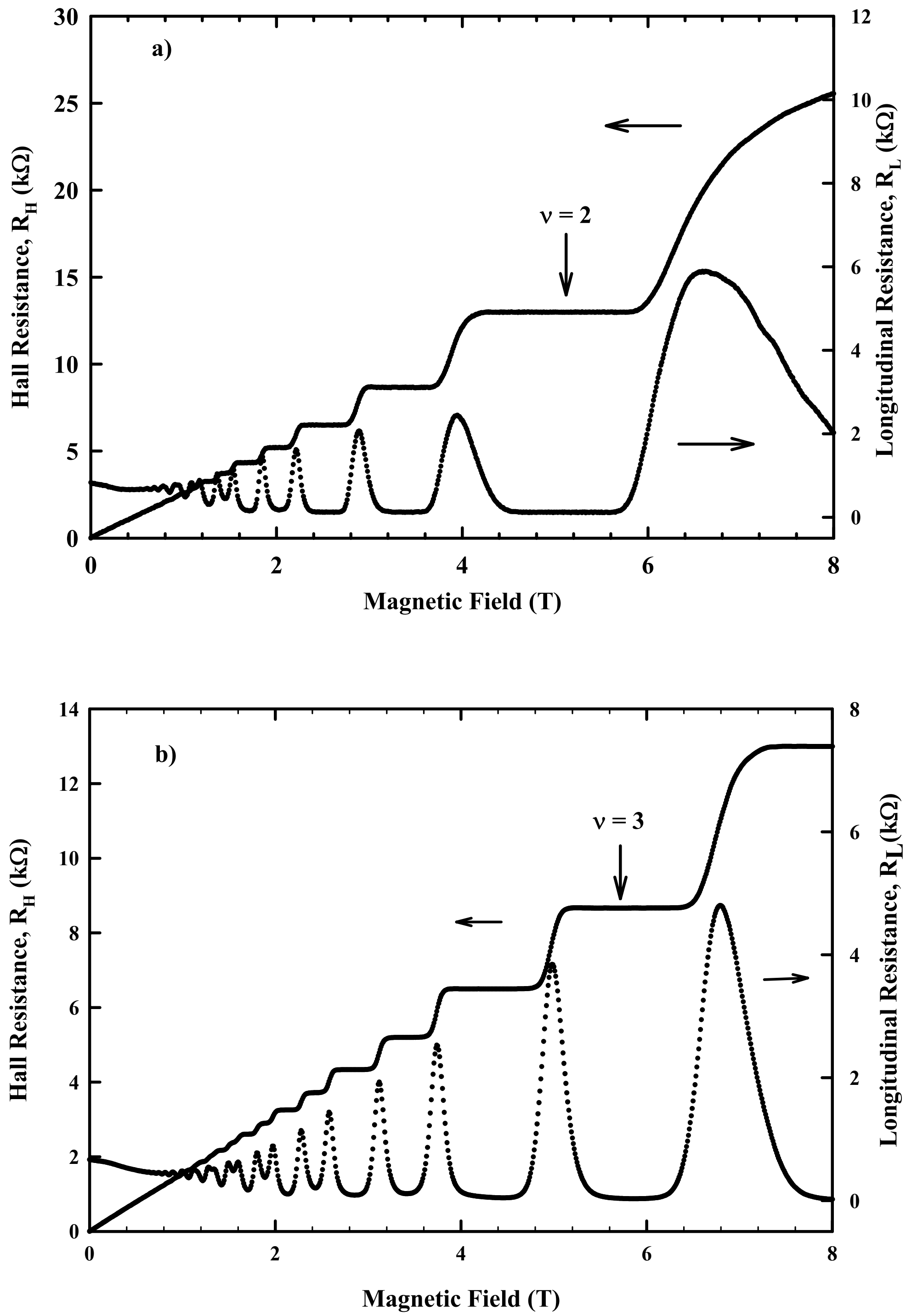

Figure 3.1: Hall resistance and longitudinal resistance for InSb quantum wells with (a) $Al_{0.09}In_{0.91}Sb$ barriers at 1.65 K (s697, M01718B), (b) with $Al_{0.15}In_{0.85}Sb$ barriers at 1.5 K (s842, N1016H).

3.3 Sample Preparation

3.3.1 Fabrication of Hall Bar

A Hall bar is fabricated from the grown quantum well structure. First, a large piece (~7 mm x 9 mm) is cleaved. Several Hall bars are defined on this piece according to the steps given in Appendix 3. An optical microscope picture of a Hall Bar is shown in Figure 3.2.

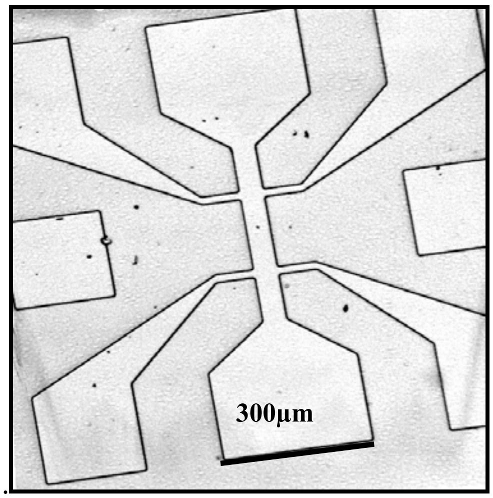

Figure 3.2: A Nomarski optical microscope picture of a 50 µm Hall bar etched on a $Al_{0.15}In_{0.85}Sb/InSb$ quantum well structure.

3.3.2 Electron beam lithography, Reactive Ion Etching

Devices with four terminals were defined on a few Hall bars by electron beam lithography and Reactive Ion Etching (RIE) with BCl_3. The etch depth was 230 and 200 nm for s697 and s842 devices, respectively. Figure 3.3 shows the schematic of four-terminal structure etched on the Hall bar.

3.3.3 Ohmic Contact

Ohmic contacts on $InSb/Al_{0.09}In_{0.91}Sb$ structure were made by evaporation of Indium on the pads of the Hall bar and subsequent annealing at 225 ^{0}C for 5 m in a mixture of H_2 (20%) +

N_2 (80%). For the InSb/$Al_{0.15}In_{0.85}Sb$ structure, AuGeNi (80%, 10%, 10%) alloy was thermally evaporated. No subsequent annealing was required.

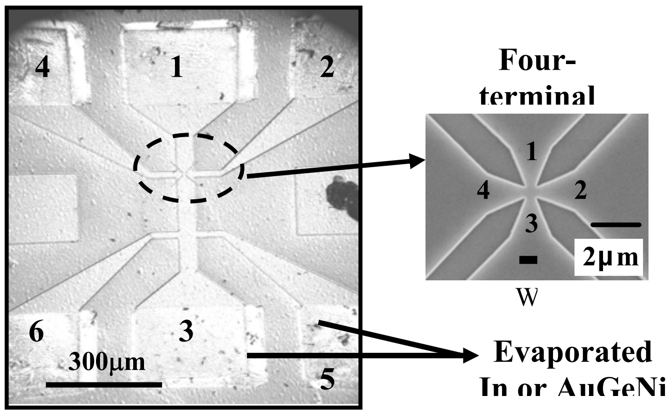

Figure 3.3: Optical microscope picture of the four-terminal structure defined on a Hall bar. SEM picture of the four-terminal structure is also shown.

3.3.4 Header and Wiring

The 7 mm x 9 mm piece was then scribed to separate out devices. Each cleaved sample had dimensions 1.2 mm x 1.2 mm. The sample was then mounted on the header using H20E epoxy, which was cured in an oven (Yamato Drying Oven DX 31) at 110 ^{0}C for 1 hour. The sample was wired with 99.99% Au wires using a wire wedge bonder. Figure 3.4 shows a sample mounted and wired on an 8-pin header.

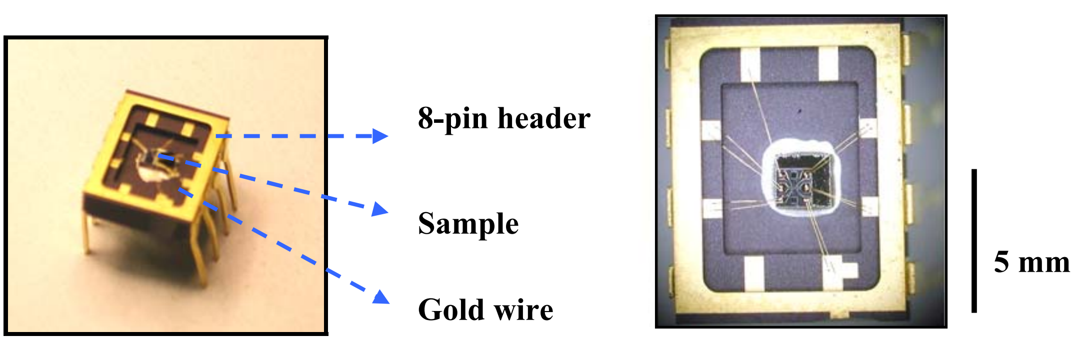

Figure 3.4: An 8-pin header with a sample wired on it.

3.4 Experimental Setup

The experimental setup used for ballistic transport measurements consists of Oxford He cryostat, 8T superconducting magnet, Oxford Intelligent superconducting magnet power supply IPS$^{120\text{-}10}$, Oxford Intelligent level meter ILM^{210}, Oxford Intelligent temperature controller ITC^{503}, HP4142B Modular DC source/monitor and SR560 low noise preamplifier. The cryostat and the magnet were cooled down to 4.2 K by liquid ^{4}He. The temperature of the sample was further reduced to 1.5 K by pumping on the ^{4}He using a rotary pump.

3.5 Measurements

3.5.1 Negative Bend Resistance, Hall resistance

For measuring bend resistance, R_B, four-terminal square devices with varying widths in the range of 0.1 to 1μm were defined by reactive ion etching. The SEM picture of a four-terminal structure is shown in the Figure 3.3. The reactive ion etch depth of the four lines is ~200 nm. R_B and Hall resistance, R_H at different temperatures were measured as functions of magnetic field. The width, W, is less than or equal to the mean free path, l_e, of the system and hence the regime is ballistic.

Bend resistance is defined as $R_B = V_{14}/I_{23}$ where V_{14} is the voltage across terminals 1 and 4 and I_{23} is the current passed from terminal 2 to terminal 3, Figure 3.3. Hall resistance is given by $R_H = V_{42}/ I_{13}$. Figure 3.5 shows a) R_B and b) R_H through the constriction at various temperatures for 0.2 μm wide four-terminal structure fabricated from InSb/ $Al_{0.09}In_{0.91}Sb$ quantum well. When the mean free path of the electrons is longer than the channel length, electrons will travel in straight lines (ballistic regime) from terminal 3. If most of the electrons have initial velocities in directions connecting terminals 3 and 1, V_{14} (and hence R_B) will be negative since a majority of injected electrons will collect in terminal 1. The NBR is a characteristic of ballistic transport. On increasing the magnetic field, the trajectory of the electrons starts to bend and the voltage becomes less negative.

3.5.1.1 S697 Devices

In Figure 3.5**,** NBR clearly indicates ballistic transport in the 0.2 μm wide device made from s697, an $InSb/Al_{0.09}In_{0.91}Sb$ quantum well. R_H shows features like "last plateau" (dashed arrow) and quenching of the Hall effect (line arrow). It is plausible that the corners of the lithographically defined lines are rounded due to depletion spreading. The rounded corners may shadow injection from the terminal 3 to 2. The positive overshoot observed in R_B at intermediate fields could be explained by rounding of the corners [33, 44]. The next cooling of this device depleted the well and no further measurements could be made.

In all the other devices there is no significant positive overshoot in R_B at small fields, indicating the sharpness of the junctions. Figure 3.6 shows a) R_H and b) R_B through the constriction at various temperatures for 0.5 μm four-terminal structure fabricated from s697. NBR is seen to persist up to 185 K. Above 185 K, the diffusive transport dominates and bend resistance is positive. The Hall resistance at 1.5 K shows features like suppression of the Hall effect (inset to Figure 3.6 a). At higher fields, the quantum Hall plateaus can be seen (not shown here). Four-terminal structures with W greater than 0.5 μm did not show ballistic characteristics in the devices with $x = 0.09$.

3.5.1.2 S842 Devices

The density of electrons in s842 is greater than that in s697. The electron mean free path is nearly the same (~0.85 μm) in both structures. Figure 3.7 shows a) R_B and b) R_H through the constriction at various temperatures for 0.2 μm wide four-terminal structure fabricated from an InSb/ $Al_{0.15}In_{0.85}Sb$ quantum well s842 (N1007G). The NBR peak amplitude in s842 device is greater than in the device shown in Figure 3.5. The fine peak structure in R_H and R_B at intermediate fields may be due to magnetic focusing effects [38]. NBR is observed up to 205 K. In a 0.2 μm device a noticeable ballistic component can be seen up to 260 K (as indicated by the dip in R_B around $B = 0\ T$ in the inset to Figure 3.7 a) even though $R_B > 0$ at $B = 0$. This strongly indicates the dominance of diffusive transport over ballistic transport. Features like quenching of Hall effect can be clearly seen in Hall resistance. Above 80 K, the Hall resistance starts to curve. This is strongly indicative of transport in a multi-carrier system (Ch. 1). If the quantum well is the only conduction path at all T, then Figure 3.7 would imply that the mean free path of the electrons in the quantum well is less than W at $T > 205\ K$. Alternatively, the diffusive conduction at higher T could be due to the emergence of another conduction path that is through a layer parallel to the quantum well. For example, intrinsic conduction through the ~3 μm of $Al_{0.15}In_{0.85}Sb$ below the quantum well would be diffusive at all T since those layers are below the etched lines that define the four-terminal device.

Figure 3.8, Figure 3.9 and Figure 3.10 show a) R_B and b) R_H through the constriction at temperatures of 0.35 μm, 0.5 μm and 0.65 μm, respectively, in four-terminal structures fabricated from s842. NBR is seen up to 200 K and there is some sign of suppression of the

Hall effect at low temperature for devices with up to 0.5 μm width. There is a transition to the QHE at higher fields in all these structures at 1.5 K. From Hall and resistivity measurements, electron mean free path for the quantum well sample is deduced to be nearly 0.84 μm. Since the 0.65 μm wide device has dimensions closer to this value, the diffusive components may have started to have a comparatively larger effect at lower temperatures. For devices with widths $\geq$ 1 μm, no ballistic transport was observed. Figure 3.11 and Figure 3.12 show the Hall resistance not through the constriction (V_{65} / I_{13}) as observed at various temperatures for N1007G, N1007D, N1007B and N1016B. The density calculated from the data for R_H through the constriction is ~14% lower than that calculated from the data for R_H not through the constriction. This may indicate that the reactive ion etching reduces the electron density.

Figure 3.13 shows the negative bend resistance amplitude for different device widths (W) at 1.5 K in four-terminal structures fabricated from s697 and s842. Figure 3.14 (a) compares the bend resistance of 0.5 μm four-terminal structures as a function of perpendicular magnetic field at 1.5 K. In Figure 3.14 (a), R_B for sample 2 is shifted by + 5 kΩ for clarity. For the W = 0.5 μm device, the NBR amplitude is smaller in the sample with x = 0.15. As shown in Figure 3.14 (b), NBR is observed at temperatures up to 185 K in the device with 9% Al concentration barriers and up to 200 K in the device with 15% Al concentration barriers.

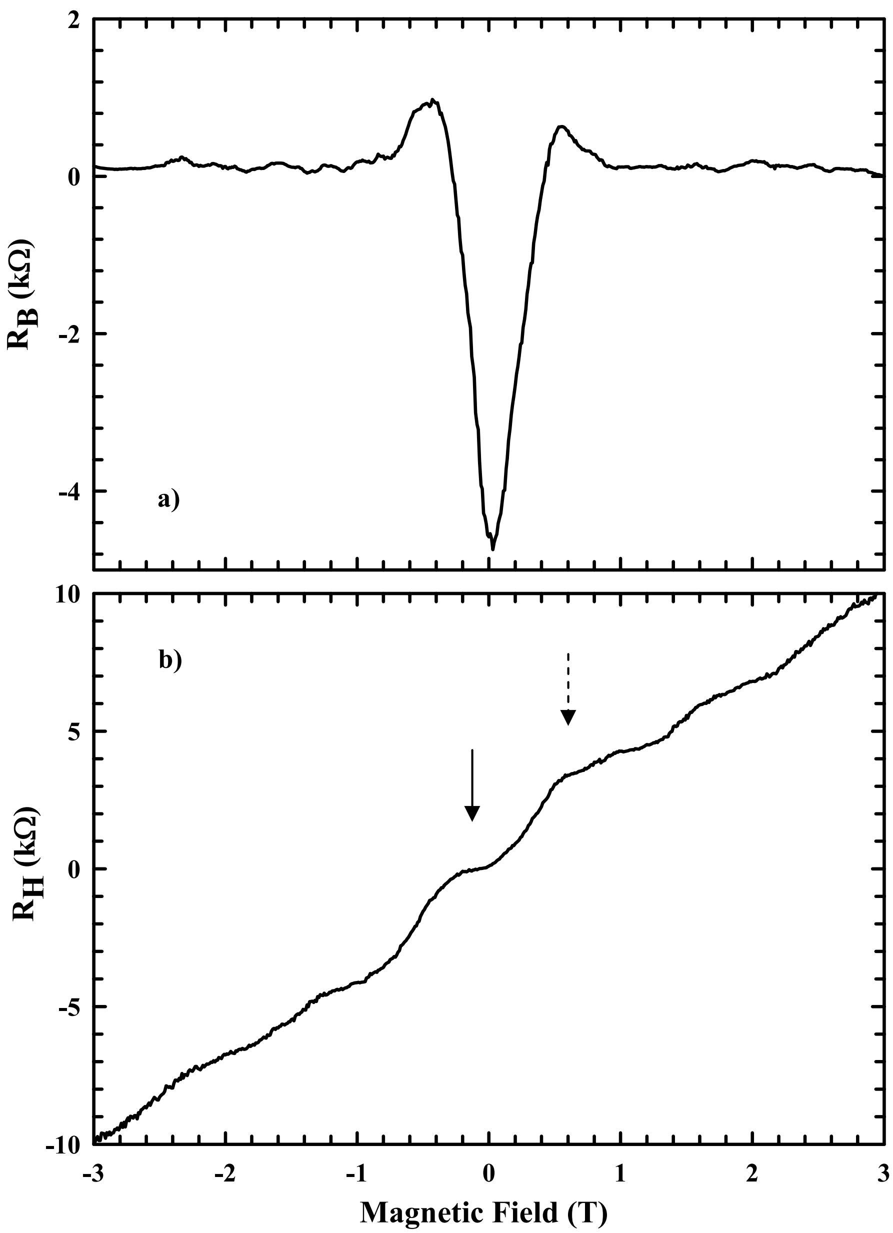

Figure 3.5: a) R_B and b) R_H as functions of B-field at 1.5 K for a 0.2 μm four-terminal structure fabricated from an $InSb/Al_{0.09}In_{0.91}Sb$ quantum well. The quenching of the Hall effect (line arrow) and the last plateau (dashed arrow) are marked in b).

a)

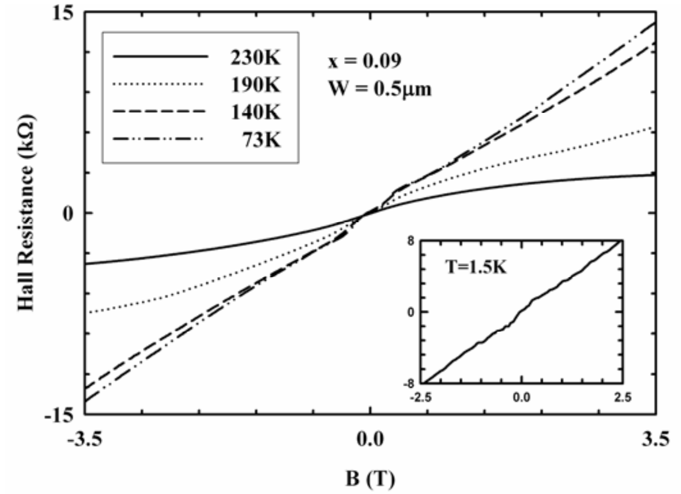

b)

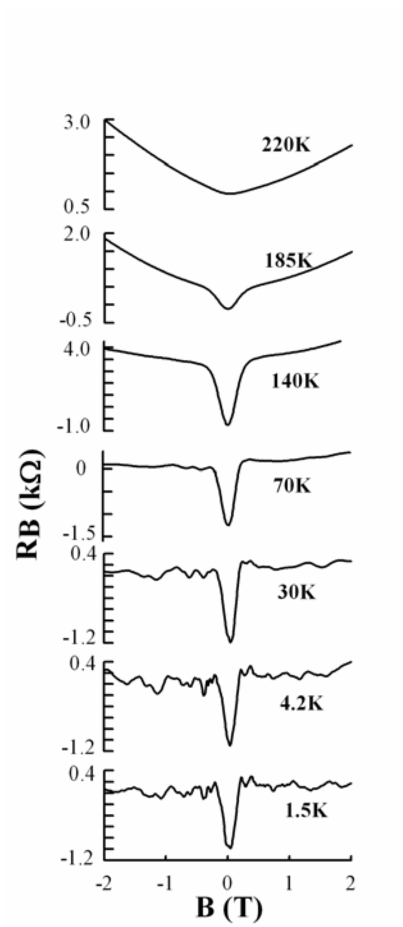

Figure 3.6: a) Hall resistance and b) Bend resistance as functions of magnetic field for various temperatures for a 0.5 μm four-terminal structure fabricated from a InSb/$Al_{0.09}In_{0.91}Sb$ quantum well.

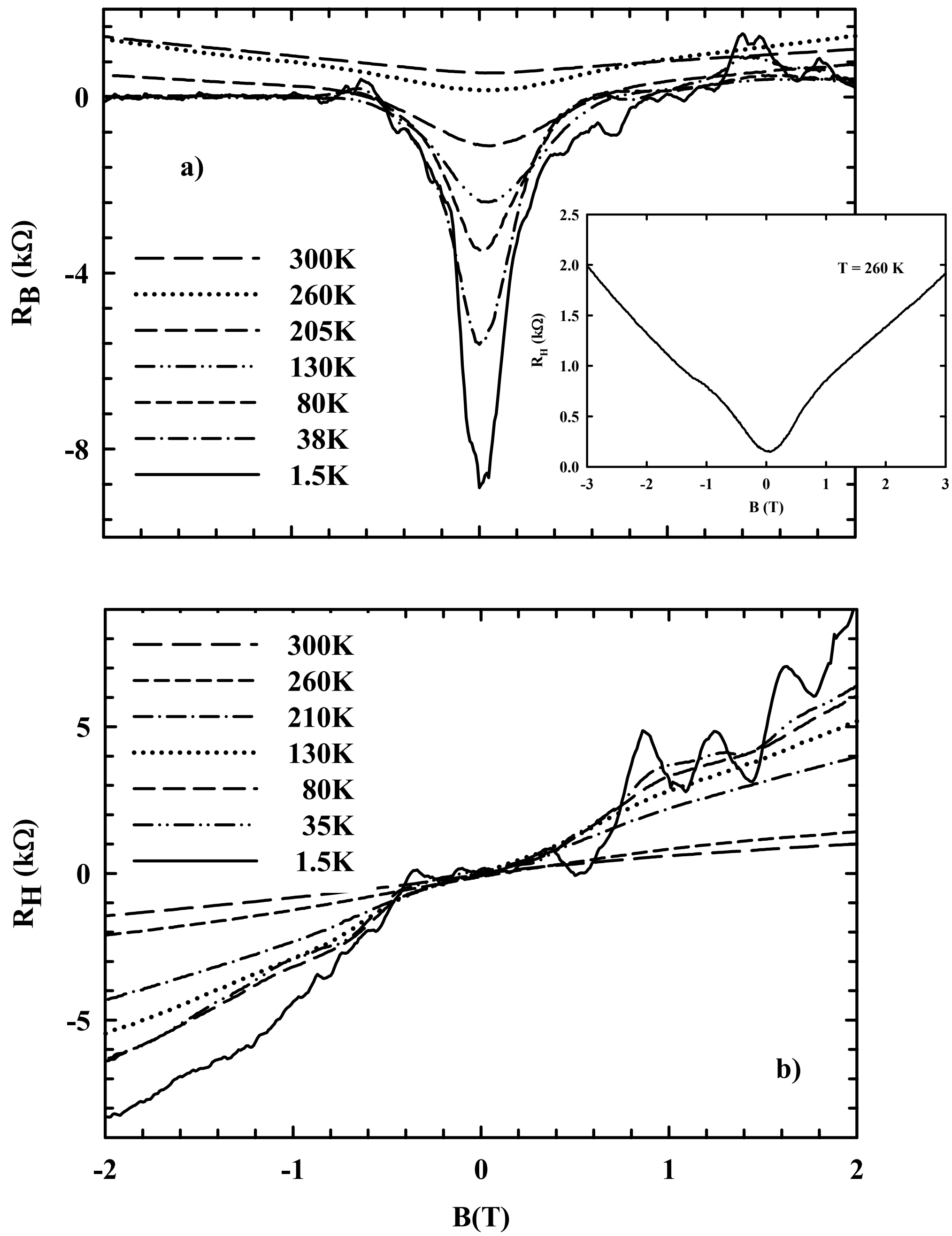

Figure 3.7: a) Bend resistance and b) Hall resistance through the constriction as functions of magnetic field for various temperatures for a 0.2 μm (N1007G) four-terminal structure fabricated from a $InSb/Al_{0.15}In_{0.85}Sb$ quantum well.

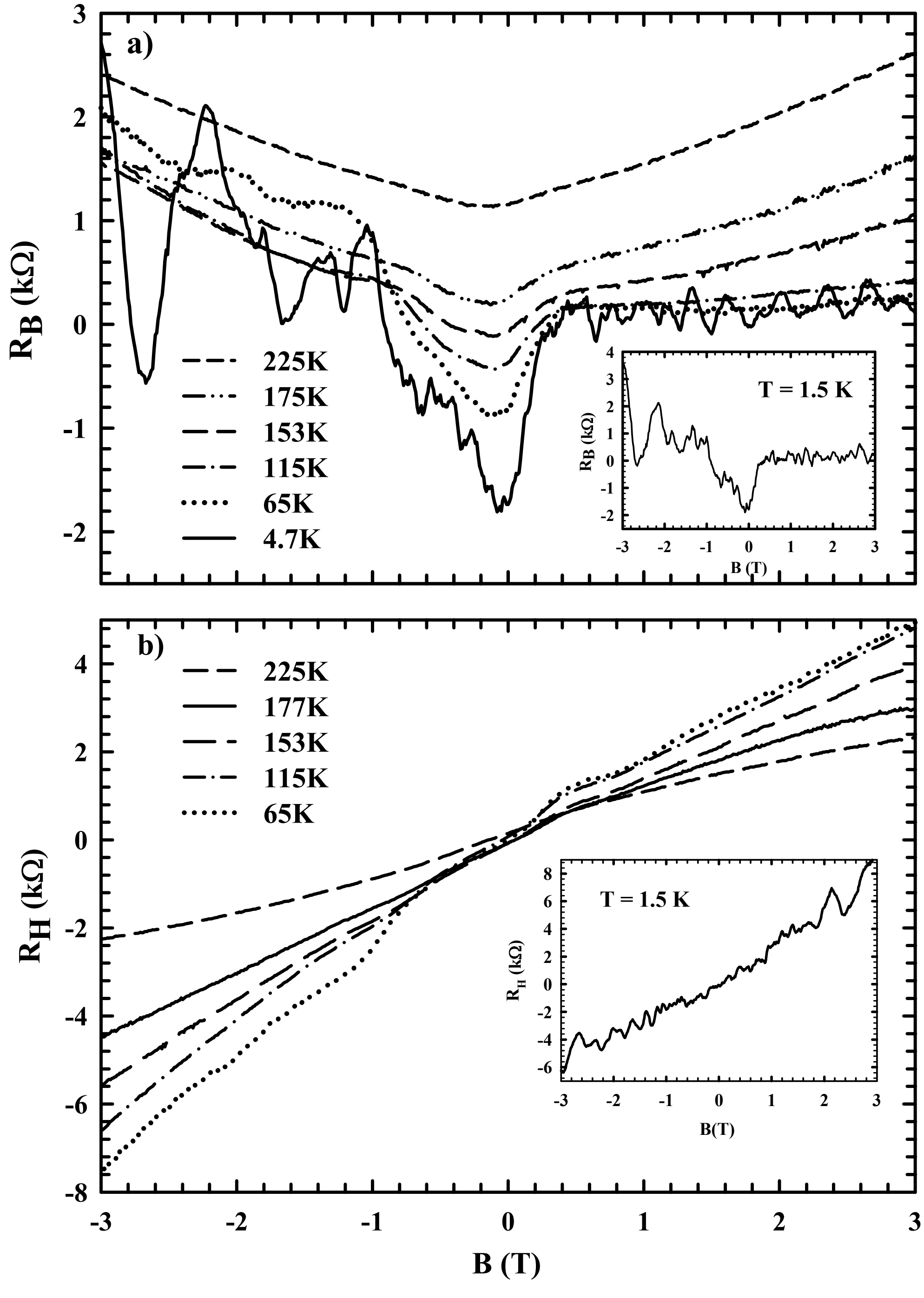

Figure 3.8: a) Bend resistance and b) Hall resistance as functions of magnetic field for various temperatures for a 0.35 μm four-terminal structure (N1007B) fabricated from a InSb/$Al_{0.15}In_{0.85}Sb$ quantum well.

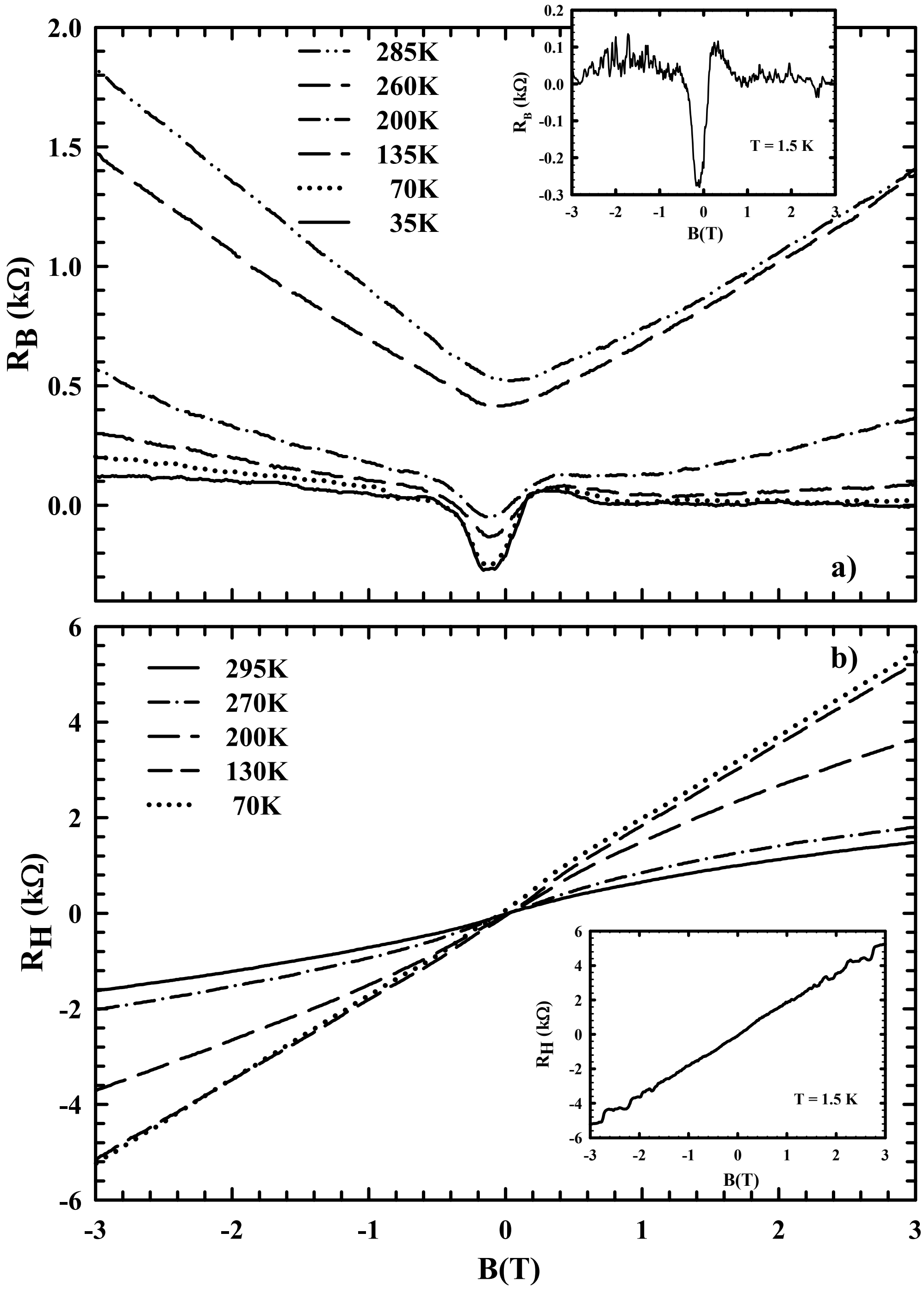

Figure 3.9: a) Bend resistance and b) Hall resistance as functions of magnetic field for various temperatures for a 0.5 μm four-terminal structure (N1016B) fabricated from a InSb/$Al_{0.15}In_{0.85}Sb$ quantum well.

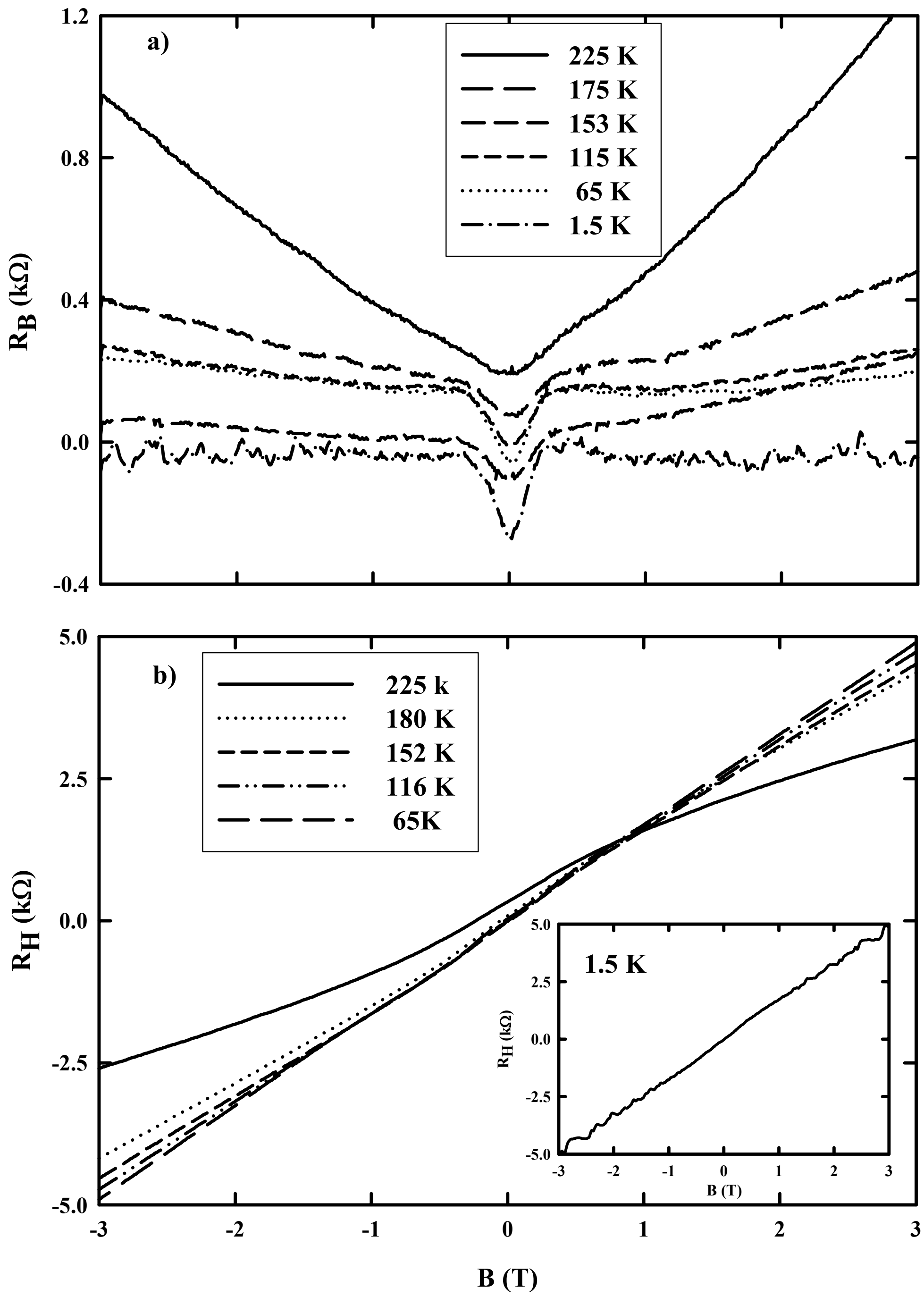

Figure 3.10: a) Bend resistance and b) Hall resistance as functions of magnetic field for various temperatures for a 0.65 μm four-terminal structure (N1007D) fabricated from a InSb/$Al_{0.15}In_{0.85}Sb$ quantum well.

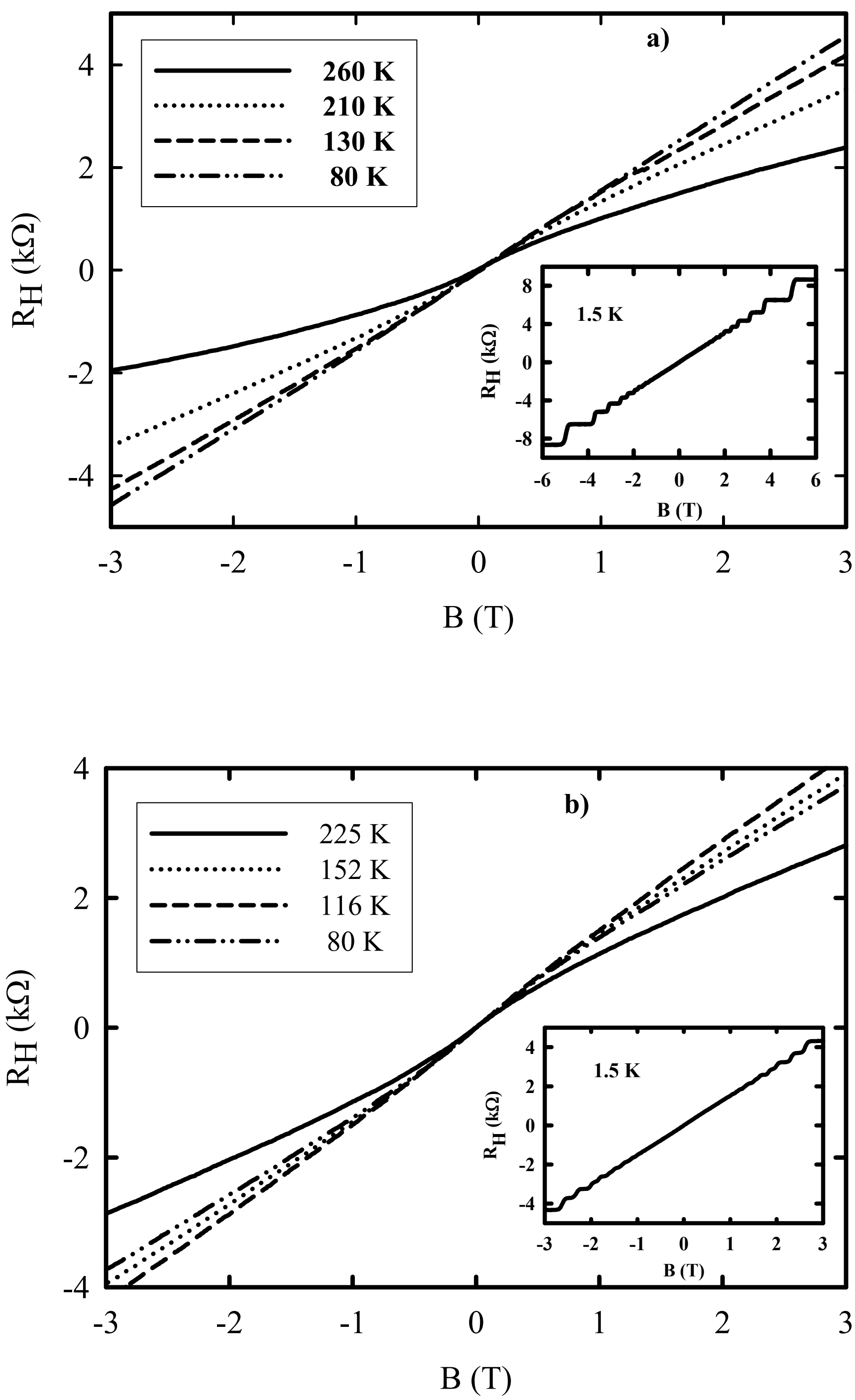

Figure 3.11: Hall resistance not through the constriction for a) N1007G and b) N1007D.

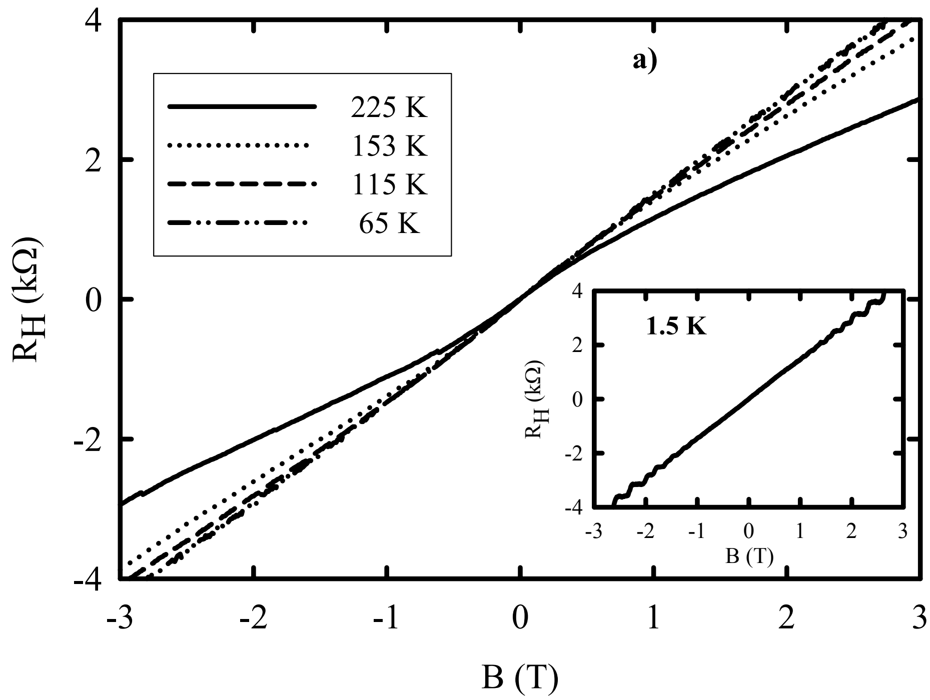

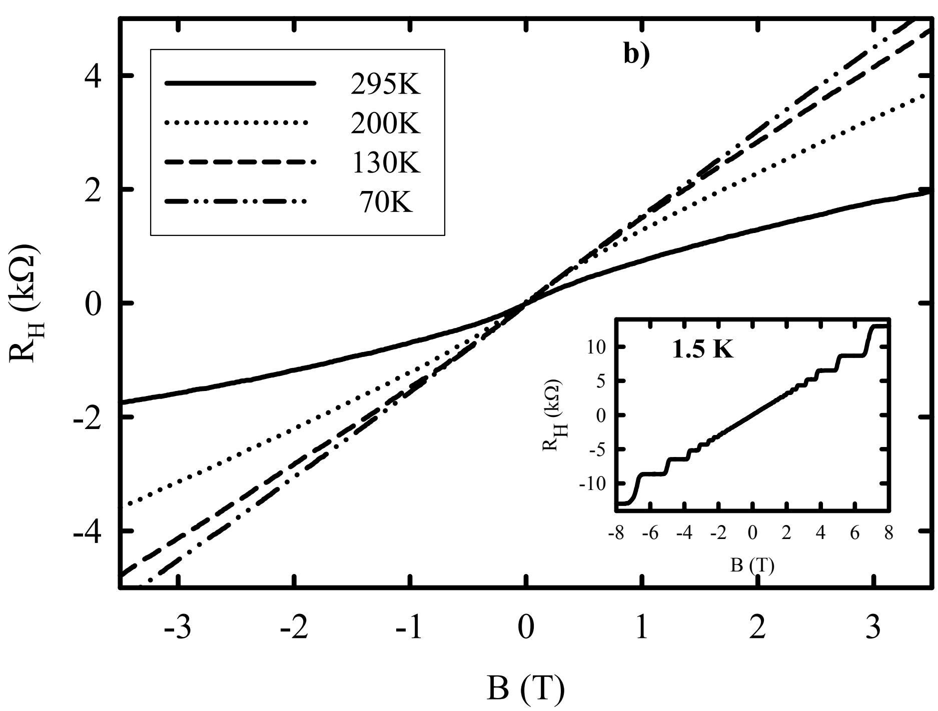

Figure 3.12: Hall resistance not through the constriction for a) N1007B and b) N1016B.

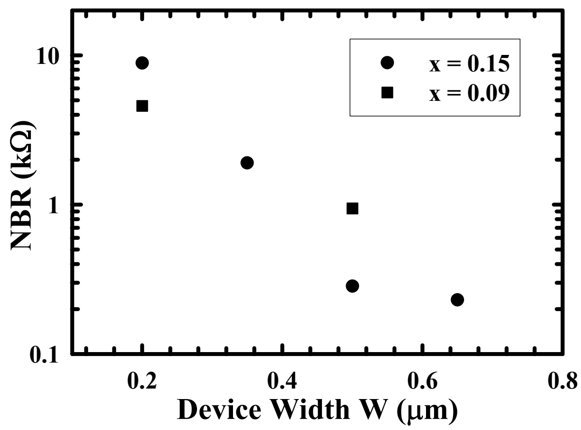

Figure 3.13: Comparison between NBR amplitude as a function of device widths (W) at 1.5 K in four-terminal structures fabricated on InSb/ $Al_xIn_{1-x}Sb$ quantum wells.

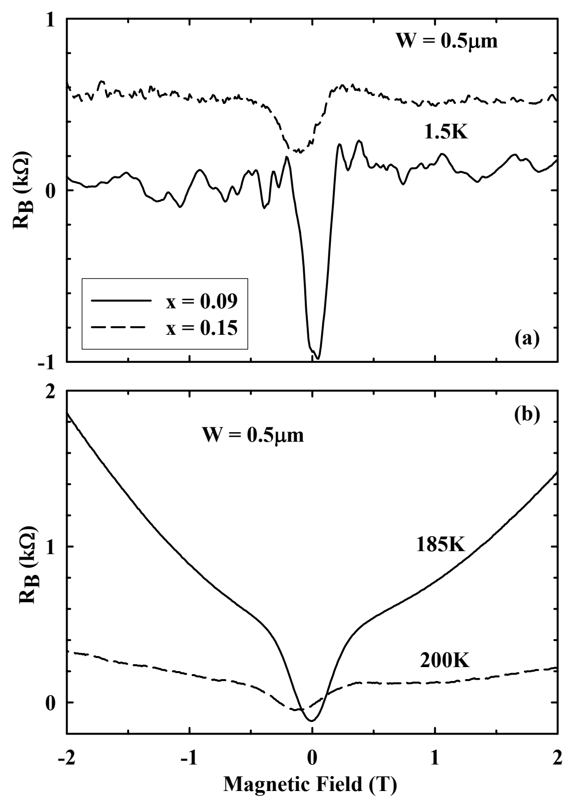

Figure 3.14: Bend Resistance for 0.5 μm four-terminal structure fabricated from InSb/$Al_xIn_{1-x}Sb$ quantum wells at a) 1.5 K and b) higher temperature. In (a) R_B is shifted by + 5 kΩ for clarity.

3.5.2 Transport Measurements on Hall Bar

The Hall resistance and the longitudinal resistance as functions of B were also measured in 50 μm wide Hall bar fabricated from InSb/$Al_xIn_{1-x}Sb$ ($x = 0.09, 0.15$) single quantum well samples. Figure 3.15 shows a) Hall and b) longitudinal resistivity at various temperatures as functions of magnetic field for a Hall bar fabricated from an InSb/ $Al_{0.09}In_{0.91}Sb$ quantum well sample. Figure 3.16 shows a) longitudinal and b) Hall resistance for different temperatures as functions of magnetic field for an InSb/ $Al_{0.15}In_{0.85}Sb$ Hall bar. For $T \geq 150$ K, the Hall resistance starts to curve with magnetic field. The non-linearity is pronounced at 300 K. This indicates the presence of more than one type of carrier at higher temperatures.

3.6 Discussion

3.6.1 Parallel Conduction

Higher μ and n are desirable for achieving high l_e. Higher n also allows the fabrication of smaller four terminal structures by preventing channel pinch off due to depletion from etched sidewalls. The height of the barrier can be increased to increase the density of carriers in the well. But increasing the Al concentration in the $Al_xIn_{1-x}Sb$ barriers above $x = 0.15$ introduces misfit dislocations in 200-300 Å thick quantum wells. On comparing our two samples, the effect of increasing n on the mean free path is weakened by the decrease in μ in the structure with a higher barrier. Because of the large lattice mismatch, dislocations are formed at the substrate interface [24] The defect density decreases during subsequent growth due to self-annihilation and filtering by the AlSb and superlattice layers. However, a significant number of micro-twin defects propagate through the quantum-well layer in both samples. This causes a reduction in the mobility, particularly at low temperatures [24]. Optimization of the buffer layer sequence to decrease the defect density is in progress.

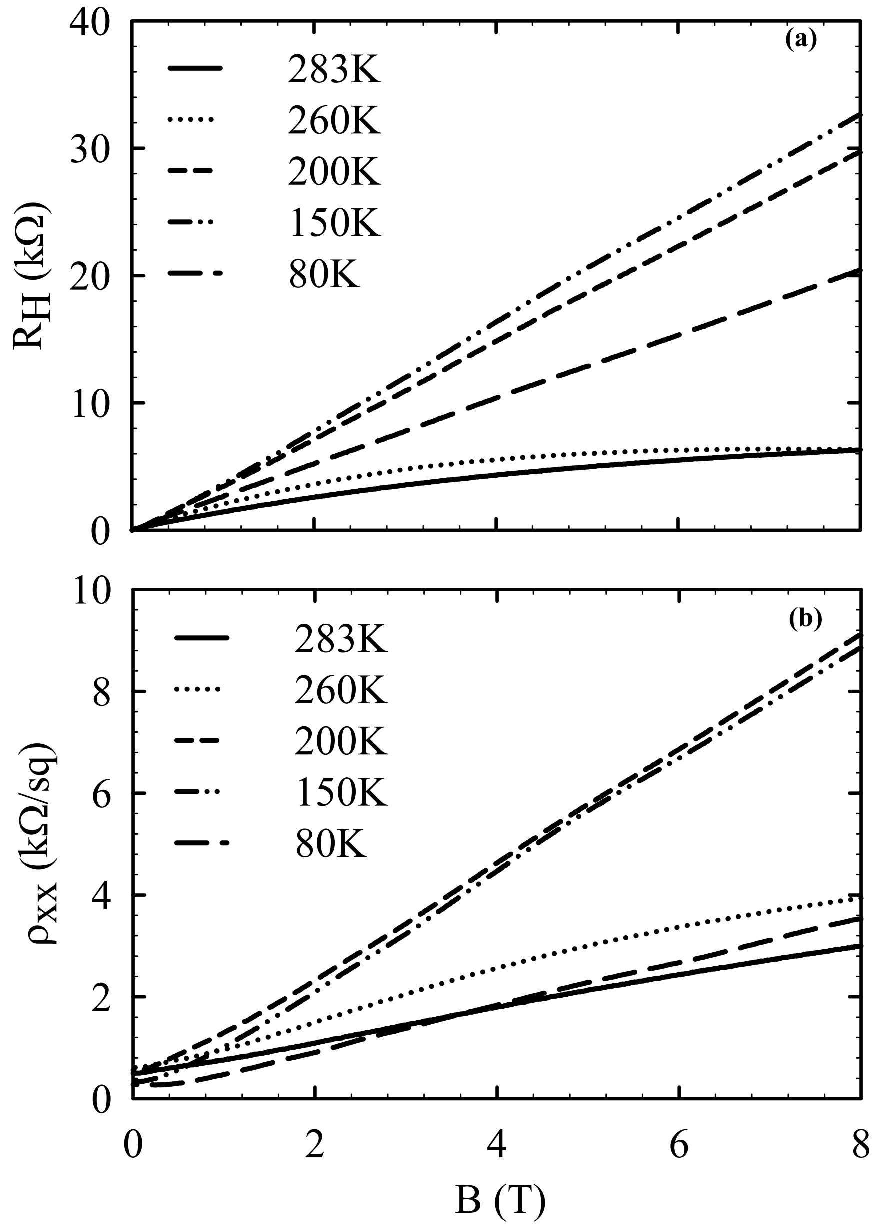

Figure 3.15: a) Hall resistance and b) longitudinal resistivity as functions of magnetic field for various temperatures for a Hall bar fabricated from InSb/ $Al_{0.09}In_{0.91}Sb$ quantum well (M01718B).

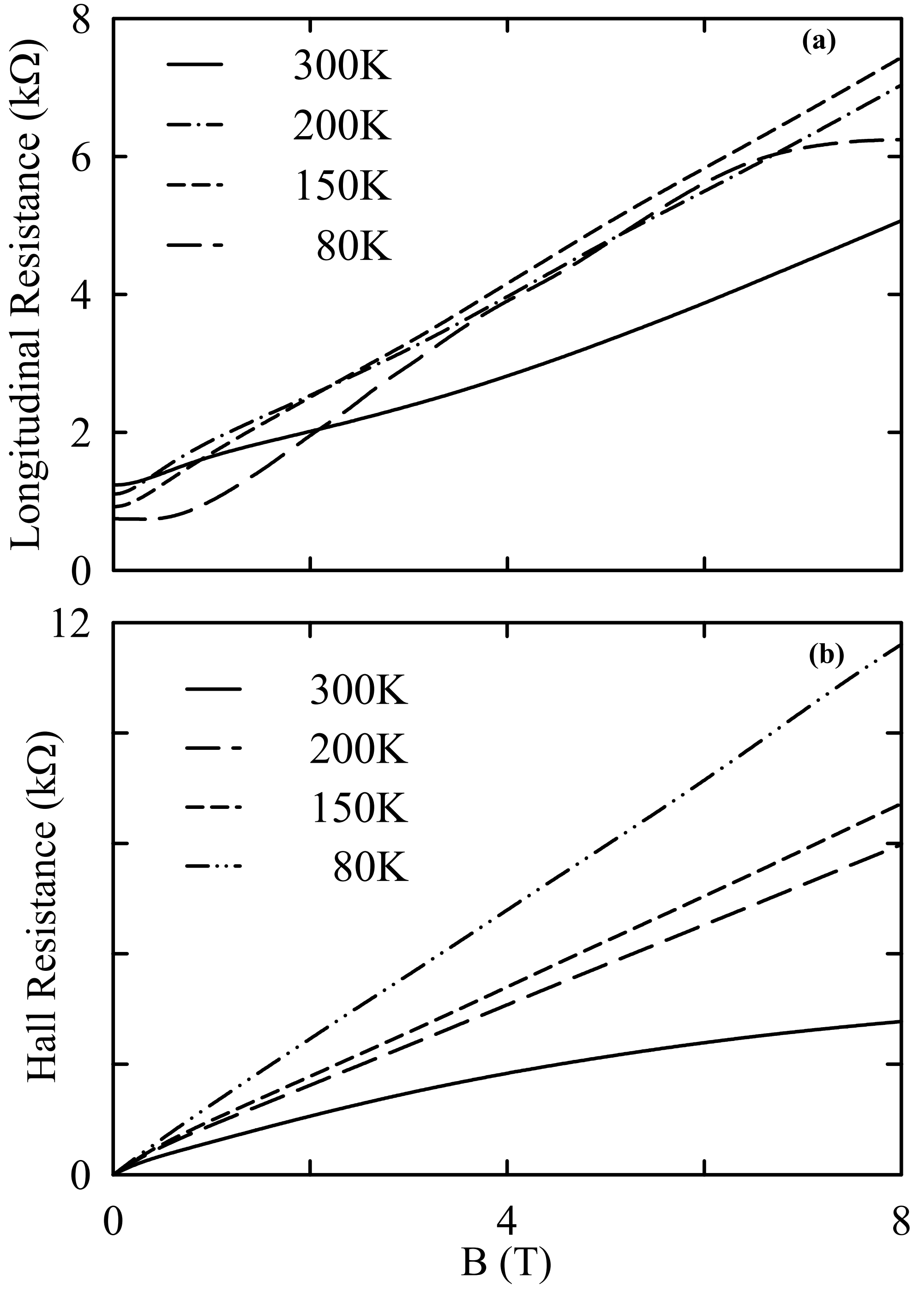

Figure 3.16: a) Longitudinal resistance and b) Hall resistance as functions of magnetic field for various temperatures for a Hall bar fabricated from InSb/ $Al_{0.15}In_{0.85}Sb$ quantum well (N1016H).

To get an accurate estimate of the relative importance of the different conduction paths, we use an iterative approach called quantitative mobility spectrum analysis, QMSA [Sec.1.4.5]. This approach deduces μ and n of each conduction path from measurements of Hall resistance and longitudinal resistance as functions of B. The number of conduction paths is not an input parameter, but rather is deduced by the calculation.

Using the overrelaxed iteration algorithm given by Eq. (1.73, 1.74), density and mobility of carriers can be calculated. First using the longitudinal and Hall resistance data obtained from the Hall bar of InSb/$Al_xIn_{1-x}Sb$ ($x = 0.09, 0.15$), as given in Figure 3.15 and Figure 3.16, experimental conductivity tensors are calculated. To smooth the data set, the data points are interpolated using spline interpolation technique. The initial trial functions are calculated using Dziuba and Gorska approach as given in Sec.1.4.4. The iteration constants ω_{xx} and ω_{xy} are both equal to 0.01. The QMSA result is calculated for various temperatures.

According to QMSA, two channels are present at $T \geq 150K$ in both the samples. Figure 3.17 and Figure 3.18 show the density, mobility and conductivity in the two channels for the Hall bar fabricated from sample 1 and 2 with 9% and 15% Al concentration in the alloy respectively. For sample 1 at 230 K, $\mu = 51{,}000\ cm^2/Vs$ and $n = 1.6 \times 10^{11}\ cm^{-2}$ for the 2DEG, and $\mu = 22{,}000\ cm^2/Vs$ and $n = 0.6 \times 10^{11}\ cm^{-2}$ for the dominant parallel channel. For sample 2 at 200 K, $\mu = 51{,}000\ cm^2/Vs$ and $n = 3.4 \times 10^{11}\ cm^{-2}$ for the 2DEG, and $\mu = 10{,}000\ cm^2/Vs$ and $n = 2.4 \times 10^{11}\ cm^{-2}$ for the dominant parallel channel. The n and μ values in the quantum well at 200 K for sample 2, where NBR is still observed, imply $l_e = 0.49\ \mu m$ which is still larger than W. The parallel layer, which has $l_e = 0.085\ \mu m$ accounts for only 13% of the total conductivity at 200 K. From the QMSA data, it is not surprising that NBR is observed at 205 K. Since the mean free path of the 2DEG at ~200 K is still comparable to the device length, one should expect NBR at ~200 K for both devices.

The R_B for the parallel conduction layers should be positive for two reasons: 1) If the parallel channels are below the reactive ion etch depth of ~2000 Å, the electrons will not be forced to pass through the 0.5 μm wide channel, and 2) Even if the parallel channels are within ~2000 Å of the surface, the small l_e for the parallel channels indicates that ballistic transport will not dominate in those channels at ~200 K.

On increasing T, μ in the quantum well decreases as expected for electron-phonon scattering. The n and μ in the quantum well at room temperature imply $l_e = 0.35\ \mu m$ for sample 2. Since l_e is a factor of ~2 larger than W, one might still expect to observe NBR at room temperature. However, the conductivity of the parallel channel ($l_e = 0.12\ \mu m$) is nearly one-third of the total conductivity. It is therefore plausible that diffusive transport in the parallel layer is obscuring observation of ballistic transport in the quantum well.

A comparison between the experimental data, points interpolated between a few points of the experimental data and the QMSA calculated data for the longitudinal, σ_{xx}, and transverse, σ_{xy}, conductivity tensor for both the samples ($x = 0.09$: s697; $x = 0.15$: s842) at various temperatures are shown in Figure 3.19 through Figure 3.25.

The source of the parallel-conducting path is yet to be determined. The T dependence of n implies the presence of intrinsic carriers. Conduction through the $Al_xIn_{1-x}Sb$ layer is one possible source of leakage current. The lack of a strong T dependence for μ, however, is more characteristic of conduction through a doped layer. We believe that ballistic transport in the quantum well may be observable above ~200 K if the parallel channels can be eliminated.

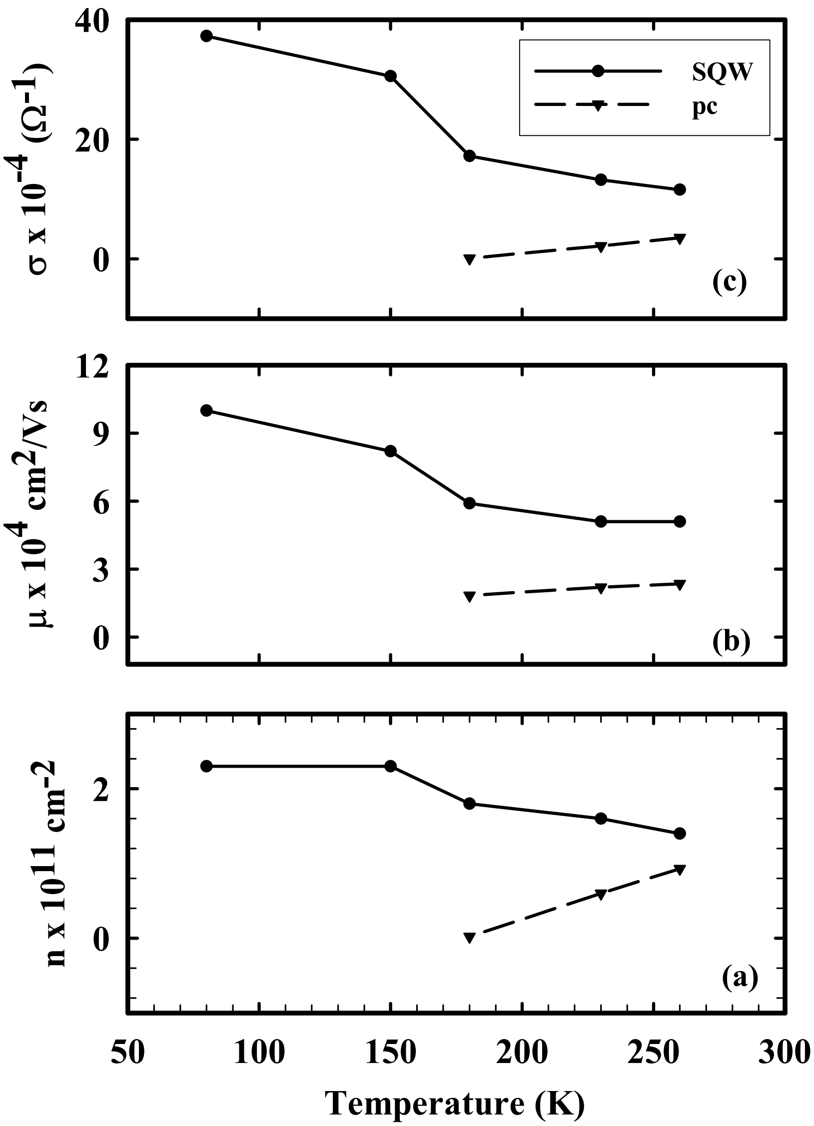

Figure 3.17: QMSA results of a) density and b) mobility as functions of temperature for carriers in $InSb/Al_{0.09}In_{0.91}Sb$ quantum well (SQW, filled circle) and in a parallel conducting channel (pc, filled triangle) calculated using the Hall and longitudinal resistance data of a Hall bar. c) The conductivity σ of the two channels as a function of *T* is shown.

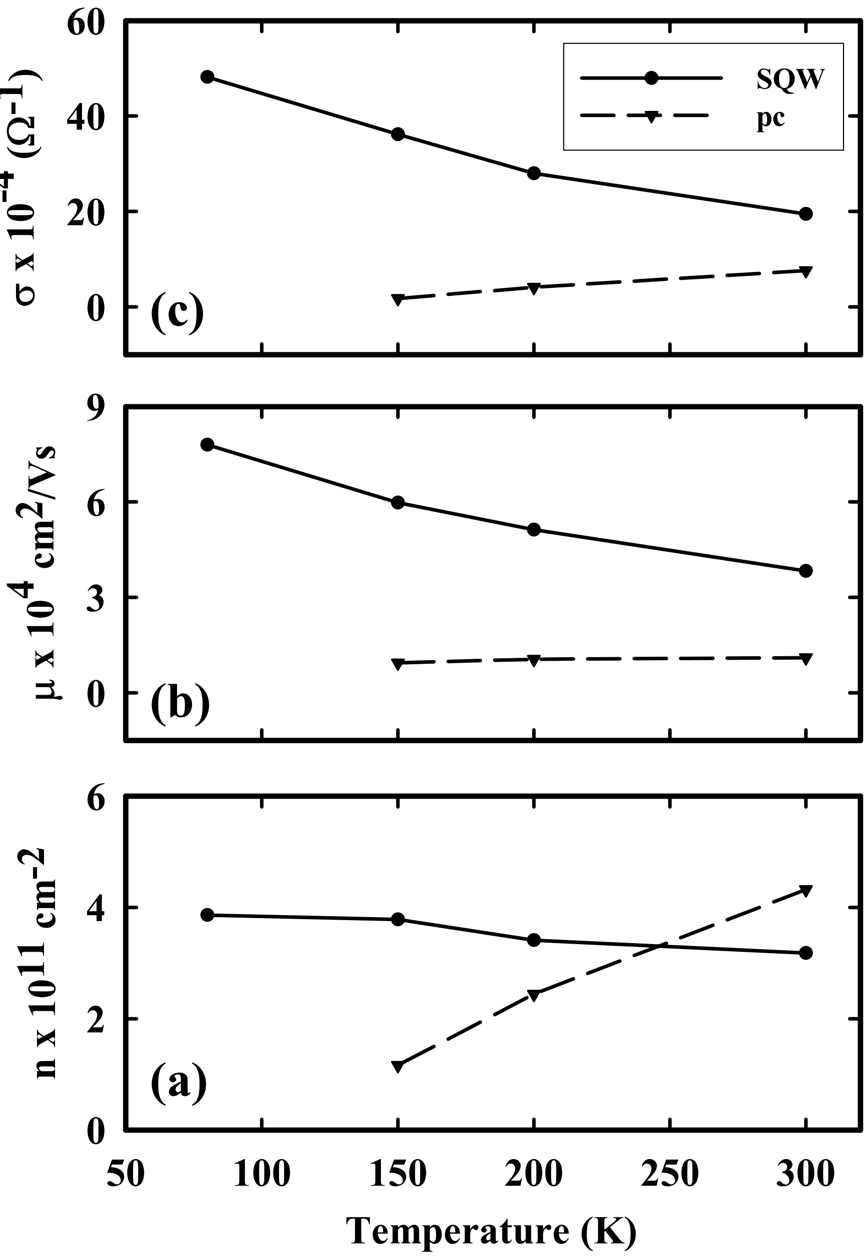

Figure 3.18: QMSA results of a) density and b) mobility as functions of temperature for carriers in InSb/$Al_{0.15}In_{0.85}Sb$ quantum well (SQW, filled circle) and in a parallel conducting channel (pc, filled triangle) calculated using the Hall and longitudinal resistance data of a Hall bar. c) The conductivity σ of the two channels as a function of T is shown.

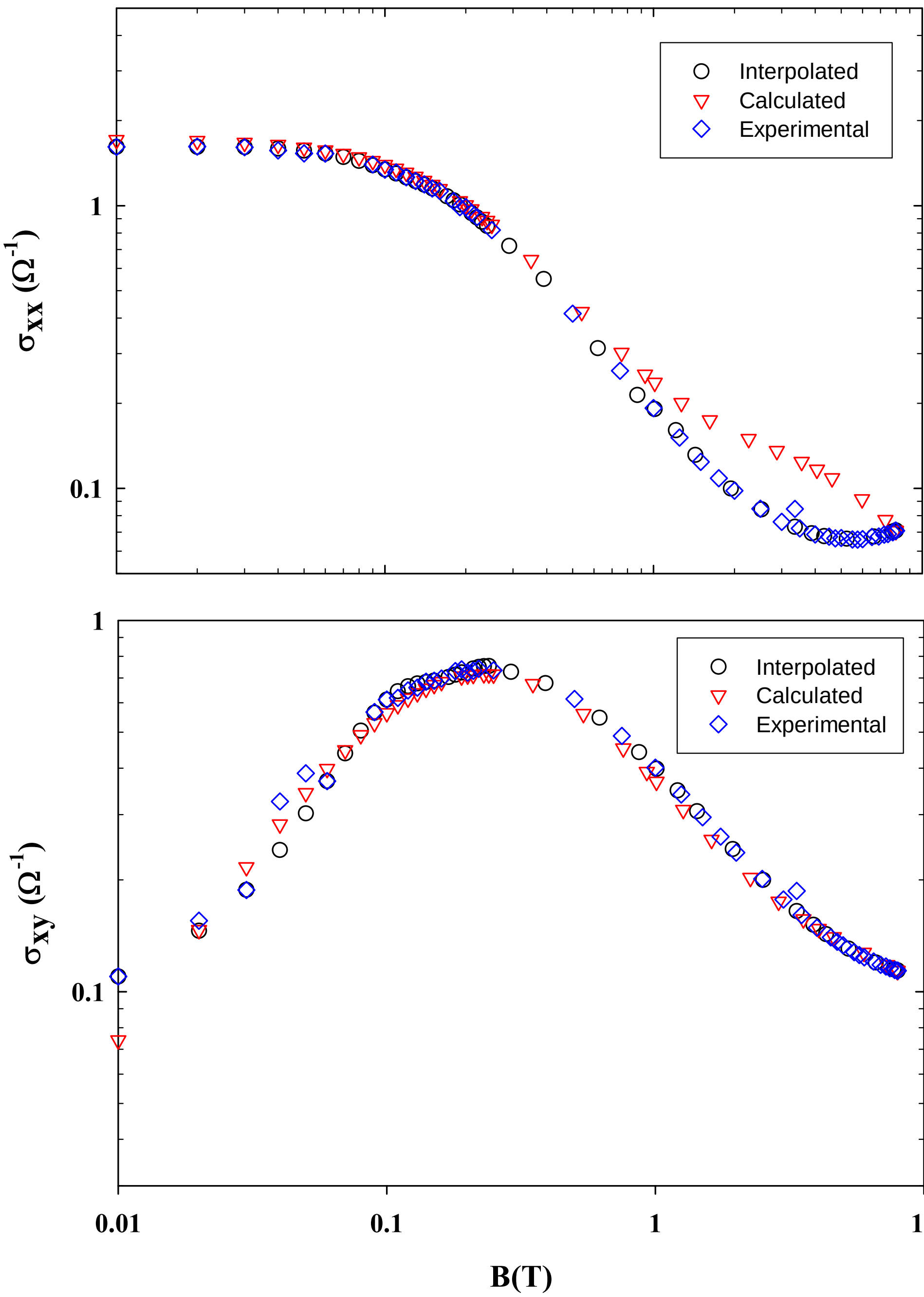

Figure 3.19: Comparison between the experimental data (diamond), data interpolated for QMSA analysis (circle) and the data calculated from QMSA (triangle) for σ_{xx} and σ_{xy} at 260 K for InSb/$Al_{0.09}In_{0.91}Sb$ Hall bar.

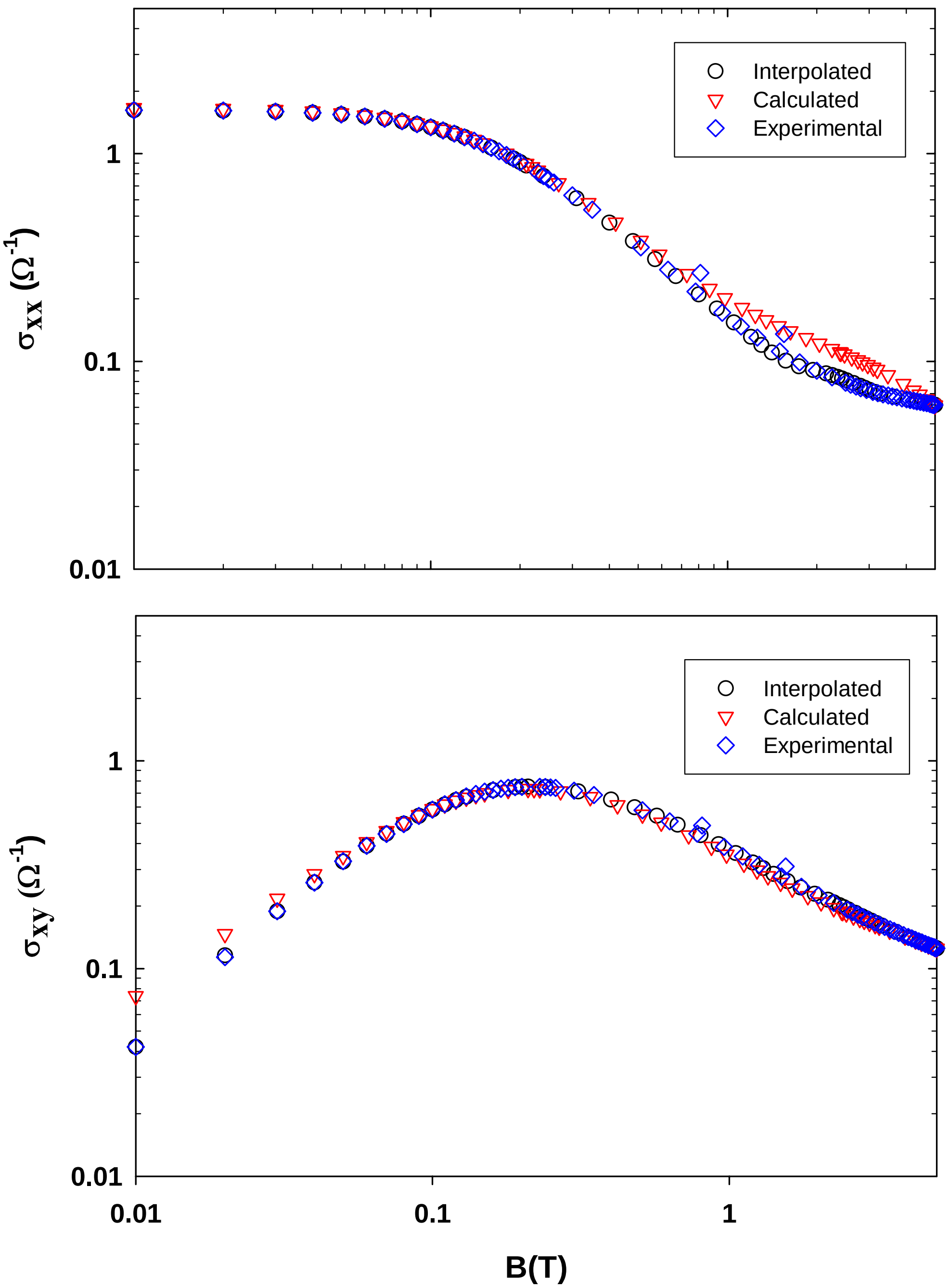

Figure 3.20: Comparison between the experimental data (diamond), data interpolated for QMSA analysis (circle) and the data calculated from QMSA (triangle) for σ_{xx} and σ_{xy} at 230 K for InSb/$Al_{0.09}In_{0.91}Sb$ Hall bar.

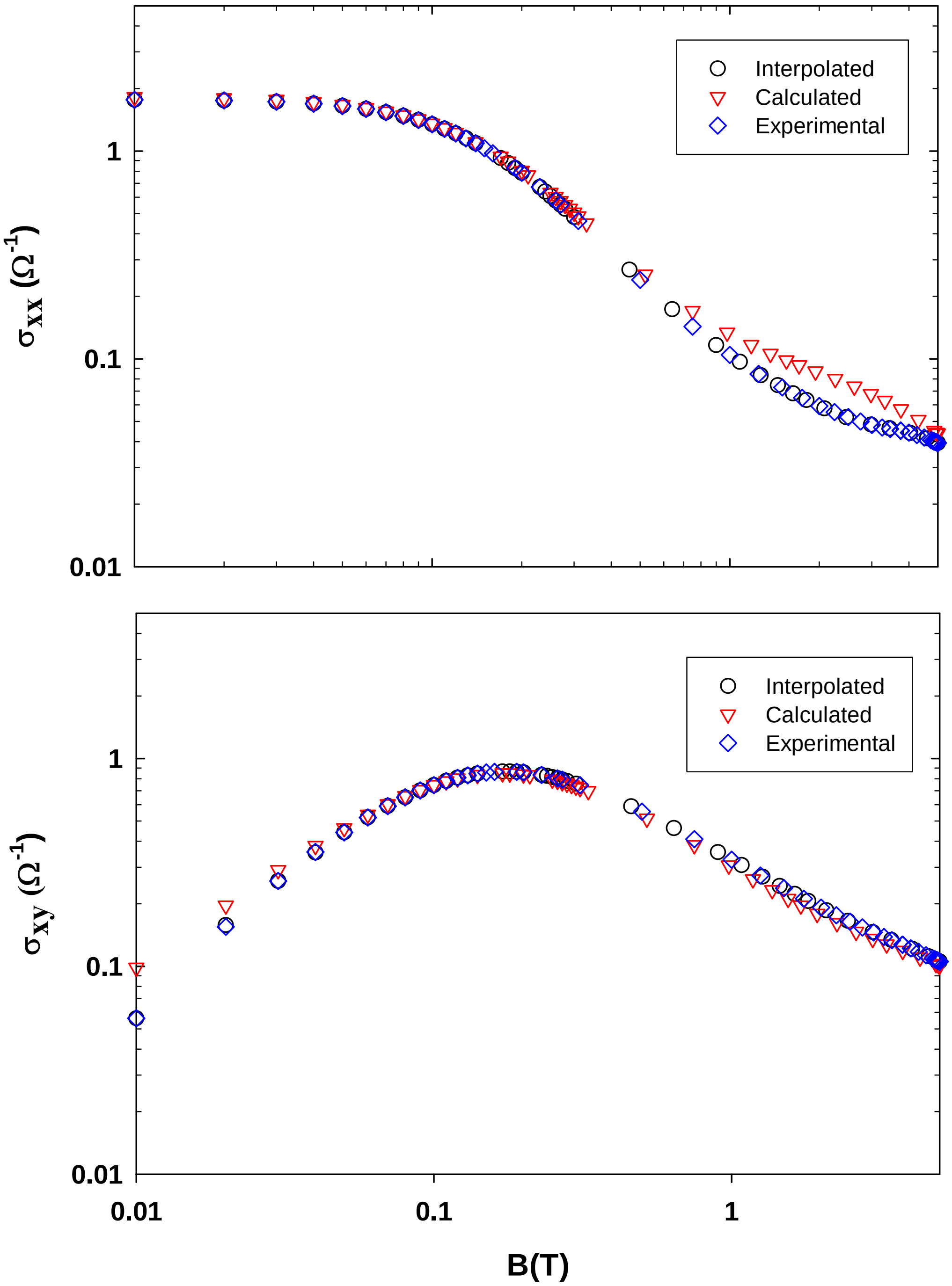

Figure 3.21: Comparison between the experimental data (diamond), data interpolated for QMSA analysis (circle) and the data calculated from QMSA (triangle) for σ_{xx} and σ_{xy} at 180 K for InSb/$Al_{0.09}In_{0.91}Sb$ Hall bar.

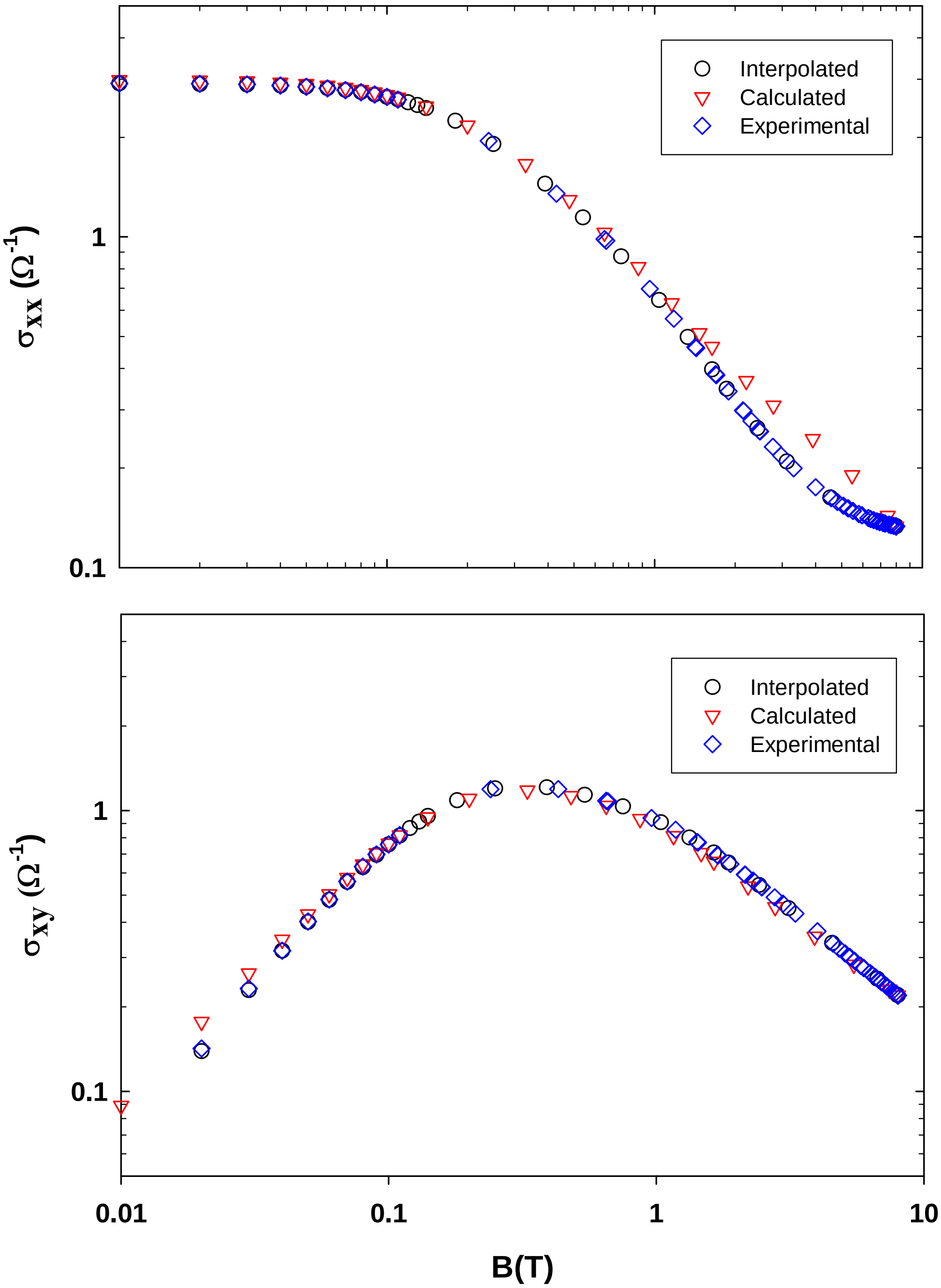

Figure 3.22: Comparison between the experimental data (diamond), data interpolated for QMSA analysis (circle) and the data calculated from QMSA (triangle) for σ_{xx} and σ_{xy} at 300 K for $InSb/Al_{0.15}In_{0.85}Sb$ Hall bar.

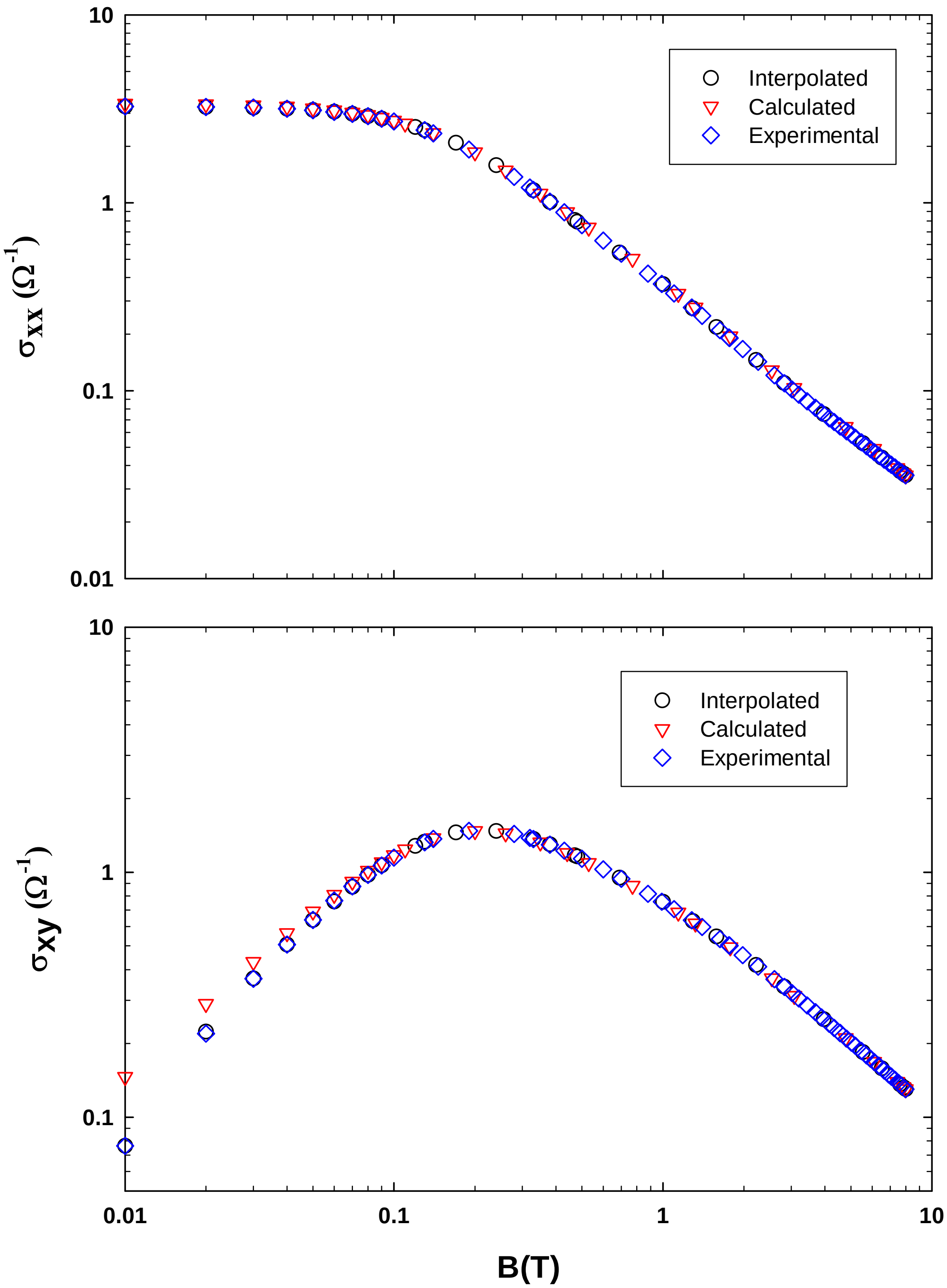

Figure 3.23: Comparison between the experimental data (diamond), data interpolated for QMSA analysis (circle) and the data calculated from QMSA (triangle) for σ_{xx} and σ_{xy} at 200 K for InSb/$Al_{0.15}In_{0.85}Sb$ Hall bar.

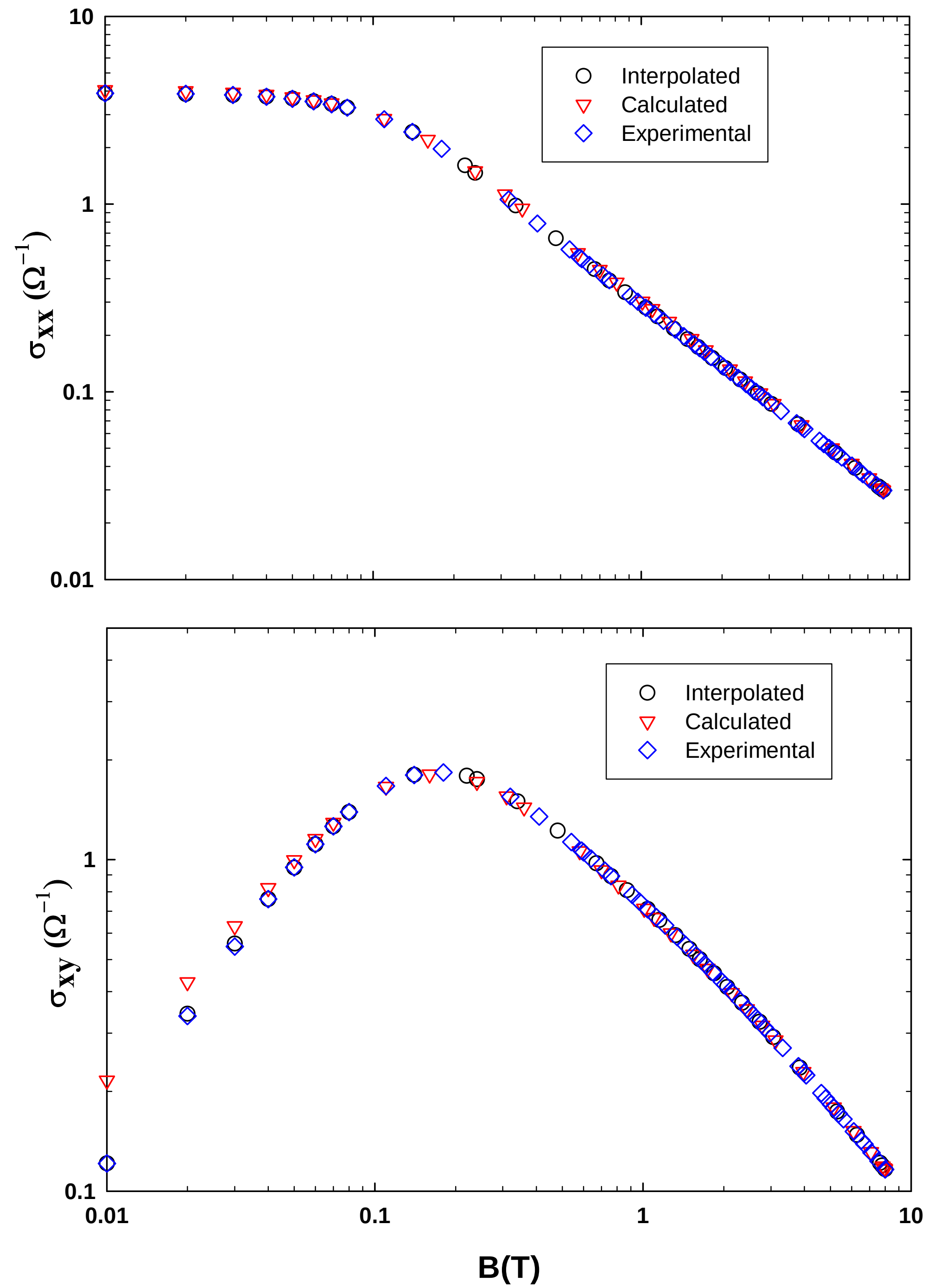

Figure 3.24: Comparison between the experimental data (diamond), data interpolated for QMSA analysis (circle) and the data calculated from QMSA (triangle) for σ_{xx} and σ_{xy} at 150 K for InSb/$Al_{0.15}In_{0.85}Sb$ Hall bar.

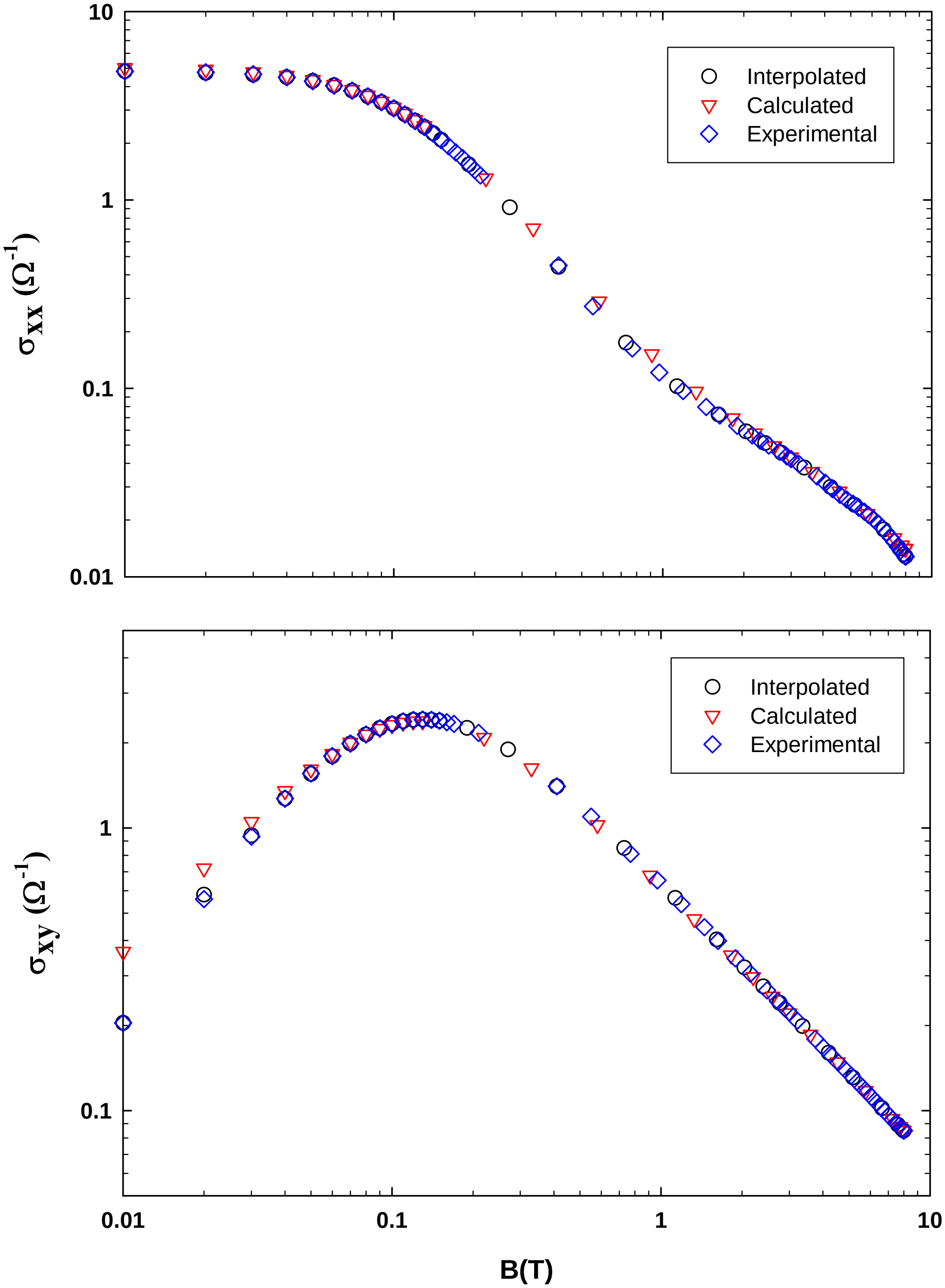

Figure 3.25: Comparison between the experimental data (diamonds), data interpolated for QMSA analysis (circle) and the data calculated from QMSA (triangle) for σ_{xx} and σ_{xy} at 80 K for InSb/$Al_{0.15}In_{0.85}Sb$ Hall bar.

Chapter 4
BALLISTIC TRANSPORT: QUANTUM POINT CONTACT

4.1 Introduction

When the dimensions of a device become smaller than the electron mean free path, scattering from the boundaries of the device is more important than scattering by impurities or phonons. The system is then in the classical ballistic regime. The last chapter showed ballistic transport features like bend resistance and quenching of Hall effect observed in InSb based mesoscopic structures. On decreasing the dimensions to the order of the wavelength of the carriers, quantum effects start to dominate. The spin field-effect transistor proposed by Datta and Das [30] is one of the several spintronic devices that require ballistic transport through a narrow-gap semiconductor channel. A clear understanding of transport behavior in narrow-gap structures of mesoscopic dimensions is essential for these device applications.

Quantum transport phenomenon has been widely studied in quantum point contacts (QPCs) which are short and narrow constrictions defined in a two-dimensional electron gas (2DEG). The widths of QPCs are smaller than the mean free path but comparable to the Fermi wavelength. In these experiments, the point contacts were defined electrostatically by either split gates defined on top of the heterostructure or by etched in-plane gates. Due to the lateral confinement in the channel, 1D subbands in the conduction band of the 2DEG are formed. The number of occupied subbands can be reduced by decreasing the width of the channel. This depopulation can be observed in the resistivity measurements. Another way to depopulate the subbands is by applying perpendicular magnetic field. The electronic structure and the quantum confinement of the QPC can therefore be determined by magnetotransport measurements.

Since the observation of conductance quantization in high mobility GaAs/AlGaAs heterostructures in 1988 by two groups working independently [54, 55], the quantization has also been reported on heterostructures with $In_xGa_{1-x}As$ channel layers [56, 57, 58], InAs/AlSb [59, 60], $Si/Si_{0.7}Ge_{0.3}$ [61] and PbTe [62] system. One-dimensional (1D) constrictions have also been fabricated using AFM [63, 64] by defining in-plane gates with the oxide lines. For all these material systems, except PbTe, the conductance exhibits plateaus quantized in units of $2e^2/h$, implying the subbands are spin-degenerate at 0 T. In PbTe, an average step spacing of e^2/h has been observed [62] which implies a zero field spin splitting of 1D subbands.

The distance between the 2DEG and the surface gates limits the 1D subband spacing because the fringing fields of the gates produce a gradual rather than abrupt potential profile. The steps are therefore observed at low temperatures only. It is desired to have 2DEG closer to the surface where the confining potential due to the split gate is sharper. But in order to prevent ionized scattering from affecting the ballistic transport, the dopant layer can not be too close to the 2DEG. In GaAs split gates, steps were observed up to 30 K with subband spacing of nearly 10 meV [47]. The effective mass of InAs is one-third that of the GaAs. Thus for the same potential the subband spacing in InAs is expected to be three times larger than in GaAs. In InAs/AlSb split gates devices, the dopants were in the surface layer, and steps were observed up to 30 K with subband spacing of ~11 meV [60, 65]. This value of subband spacing is similar to GaAs and the result was attributed to the immaturity of InAs system. Effects like parallel conduction and gate leakage present in this system was believed to disrupt the quantization at temperatures below the expected limit.

InSb has several properties that are advantageous for ballistic transport devices. Electrons have a higher room temperature mobility, a smaller effective mass ($m^* = 0.0139m_0$), and a larger *g*-factor (*-51*) in InSb than in any other III-V binary semiconductors. Since the mean free path depends on mobility, ballistic effects should persist to higher temperatures. The larger energy level spacing due to a small m^* should allow quantum ballistic devices to operate at higher temperatures. The large *g*-factor should reduce the magnetic field required to resolve Zeeman spin splitting. Additionally, a large Rashba spin splitting [16] has been observed in InSb quantum wells. This chapter presents the preliminary data for the realization of in-plane gate quantum point contacts in $InSb/Al_xIn_{1-x}Sb$ ($x = 0.09, 0.15$) quantum wells.

4.2 Quantum Point Contact

4.2.1 Two-dimensional Electron Gas

The energy of electrons in a subband of a 2DEG relative to the bottom of the subband is given by Eq. (1.30). The density of states for a single subband in a 2DEG is independent of energy and is given by Eq. (1.29). If magnetic field is applied perpendicular to the 2DEG, the electrons in the 2DEG move in a cyclotron orbit due to the Lorentz force. The energy is thus quantized, Eq. (1.27). The spin degeneracy is lifted in higher magnetic field due to Zeeman splitting $g\mu_B B$ of the Landau levels, Eq. (1.33).

4.2.2 Narrow Channel

If the 2DEG is confined laterally in a narrow channel, the 2D subband splits into a series of one-dimensional subbands with bottom of the bands at E_n. The last term in Eq. (1.33) is then the kinetic energy in the direction of the channel axis. The total energy of electron in the n^{th} 1D subband is given by

$$E_n(k) = E_n + \frac{\hbar^2 k^2}{2m^*} \tag{4.1}$$

In the literature, the lateral confinement has been modeled as either a square-well potential [66] or a parabolic potential well [67]. For wider channels at small gate voltage, the lateral confinement potential is described by square well with a width equal to the lithographic separation of split gates or the width between the two etched in-plane gates. The density is equal to the 2DEG density. When the gate voltage is made more negative, the subbands are depopulated. When there are only a few subbands occupied, the parabolic potential confinement, given below, can be considered.

$$V(x) = \frac{1}{2} m \omega_0^2 x^2 \tag{4.2}$$

The respective confinement levels for the square well and parabolic potentials are

$$E_n = \frac{(n\pi\hbar)^2}{2mW^2} \qquad \text{(for the square well potential)} \qquad n = 1, 2, 3 \ldots \tag{4.3}$$

$$E_n = (n - \frac{1}{2})\hbar\omega_0 \qquad \text{(for the parabolic well)} \qquad n = 1, 2, 3, \ldots. \tag{4.4}$$

where W is the width of the square well. If the channel is along the y-direction and B is applied in z-direction, the Hamiltonian for the 1D transport in QPC is

$$H = \frac{1}{2m^*}(-i\hbar\vec{\nabla} + e\vec{A})^2 + V(x) = -\frac{\hbar^2}{2m^*}\frac{\partial^2}{\partial x^2} + \frac{\hbar^2}{2m^*}(k_y + \frac{eBx}{\hbar})^2 + V(x) \qquad (4.5)$$

where, $\boldsymbol{A} = (0,Bx,0)$ and $V(x)$ is the confinement potential. The spin split subband energy is

$$E_n(k_y) = (n - \frac{1}{2})\hbar\omega + \frac{\hbar^2 k_y^2}{2m} \pm \frac{1}{2} g\mu_B B \qquad (4.6)$$

where, $m = m^* \frac{\omega^2}{\omega_0^2}$, $\omega = \sqrt{\omega_0^2 + \omega_c^2}$ and $\omega_c = \frac{eB}{m^*}$. The mass, m, is enhanced by a factor compared to the effective mass, m^*. The density of states depends on $\sqrt{m}$ and is therefore increased, too [67, 68, 69, 70].

4.2.3 Quantized Conductance

Point contacts in a 2DEG are defined by split gates on the top of the heterostructure or by in-plane gates. In split gate devices, the 2DEG is depleted from beneath the gates and a 1D channel gets defined between the gates. On the other hand, the channel in in-plane gate devices is depleted from the sides. By varying the gate voltage, the width of the point contact and the number of occupied subbands (density) can be changed. The quantized steps are observed with each subband contributing $2e^2/h$ to the conductance. This quantization is measured in the absence of magnetic field. As the number of occupied subbands is an integer, N, therefore, the total conductance is given as

$$G = \frac{2e^2}{h} N \qquad (4.7)$$

This phenomenon can be explained theoretically by Landauer-Büttiker formalism where the transport is treated as the transmission problem [48].

The subbands can also be depopulated by applying magnetic field perpendicular to the 2DEG. The B-field has considerable effect if the cyclotron diameter is less than the channel width (i.e. $B >> B_{crit} = \frac{2\hbar k_F}{eW}$). The electrostatic confinement for the density of states can be neglected and the density of states is defined by Landau levels (see Ch. 1). For $B << B_{crit}$, the electrostatic confinement is more important. The subbands are called magnetoelectric subbands around B_{crit}, as both electrostatic and magnetic confinements determine the density of states. They are depopulated more slowly compared to the depopulation of Landau levels. At high field, spin degeneracy is lifted ($g\mu_B B$) and conductance from each spin split subband is given by $G = e^2/h$.

As the temperature increases, the plateaus begin to have a slope and at high enough temperatures, cannot be resolved. At finite temperatures, G is given as [42]

$$G(E_F, T) = \frac{2e^2}{h}\sum_{n=1}^{\infty} f(E_n - E_F) \tag{4.8}$$

where, E_n is the energy at the bottom of the nth subband, E_F is the Fermi energy and f is the Fermi Dirac function.

4.2.4 Determination of *g*-factor and Subband Energy Spacing

The *g*-factors of 2DEG systems have been studied widely [71]. For GaAs system in tilted field, enhancement of *g*-factor has been observed compared to its bare value [72]. It is possible to determine the *g*-factor of 1D subbands [73] by performing the spectroscopy of 1D subbands [74] using a dc source-drain voltage, V_{SD}, in QPCs. If a dc V_{SD} is applied in the absence of B-field and the gate voltage is varied, the steps are seen in G. Additional structures called half plateaus, in the middle of the original plateaus can be observed above certain V_{SD}. The first derivative of G with respect to V_G shows peaks at V_G where steps occur in G. These are called transconductance peaks. When $eV_{SD} = \Delta E_{n,n+1}$, the transconductance peaks cross each other [73]. Here, $\Delta E_{n,n+1}$ is the energy separation between the n^{th} and $(n+1)^{th}$ subbands. This way the subband spacing of 1D constriction can be determined by source-drain bias measurement. The degeneracy of subbands can also be lifted if in-plane B-field is applied at zero source-drain bias. The *g*-factor can then be determined by comparing V_{SD} required to produce the same amount of splitting as the magnetic field [74],

$$eV_{SD} = 2g_{||}\mu_B B_{||}S + \Delta_i \tag{4.9}$$

where, Δ_i is the zero field spin splitting, $S = ½$ and $g_{||}$ is the *g*-factor in the direction of the B-field. For the wide channel GaAs based devices, measured $g_{||}$ had a value closer to the bulk GaAs value (g ~ -0.4) whereas an enhancement of $g_{||}$ was observed as the number of occupied subbands decreased [75].

4.2.5 0.7 Conductance Anomaly

There is another structure that appears at $0.7(2e^2/h)$ besides the quantized conductance plateaus mentioned above. This is called "0.7 structure" [76]. The 0.7 structure has been seen in 1D wires defined in GaAs [76, 77, 78] and Si heterostructures [79]. Occurrence of spontaneous spin splitting at zero field ($0.7\ (2e^2/h)$) has been reported to drop to $0.5\ (2e^2/h)$ in in-plane magnetic field [76] at fixed temperature. With the increase in temperature, both the quantized plateaus and anomalous plateau disappear due to thermal smearing. As the temperature is decreased, the anomalous plateau shrinks and conductance approaches ($2e^2/h$). A few groups have also reported observation of $0.5\ (2e^2/h)$ structure at 0 T [78,80] in case of low electron density samples. As the magnetic field is increased this structure was observed to strengthen [80] indicating spin polarization [81]. With the increase in temperature, it has also been observed that the zero field 0.5 $(2e^2/h)$ structure rises to $0.6(2e^2/h)$ [82].

The mechanism for the 0.7 structure has not been established conclusively yet. This can be partly due to the narrow range of temperatures (0.1- 4 K) in which it has been observed in split gate QPCs where close-lying 1D subbands are formed. The 0.7 structure has also been observed in trench-etched QPCs [83] up to 6.5 K but is absent at 1.1 K. Various groups have and are studying this anomaly theoretically using concepts of zero field spin polarization [84,85,86], spin density wave formation [87], pairing of electrons [88], singlet-triplet formation [89], Kondo –like interactions [90, 91] and electron-phonon effects [92].

At high enough field, applied parallel to the current direction, spin-split 1D subbands can be made to cross each other. If these crossing subbands have opposite spins and different spatial wavefunctions, then spontaneous splitting occurs which give rise to new structures called 0.7 analogs [93]. Since these analogs are observed in eight samples by one of the group [93], they ruled out scattering due to disorder as the reason for the phenomenon. The group argued the strong exchange interactions may lead to the degeneracy at the crossing point being lifted. At the fixed temperature, the 0.7 anomaly has also been shown to depend on the source-drain voltage. As the bias is increased from zero to some finite value, the anomaly increased from 0.7 to 0.9.

4.3 Layer Structure

To carry out experiments on InSb based QPCs, the single quantum-well structure with $Al_xIn_{1-x}Sb$ barrier layers ($x = 0.09, 0.15$), were grown on semi insulating GaAs (001) substrate. The layer sequences of the samples s697 and s842 are shown in Figure 2.6. The longitudinal resistance and the transverse (Hall) resistance at 1.5 K for both the samples are given in Figure 3.1. The density and mobility for s697 (InSb/ $Al_{0.09}In_{0.91}Sb$ quantum well) at 1.65 K are 2.4×10^{11} cm^{-2} and $1.1 \times 10^5\ cm^2/Vs$. The density and mobility for s842 (InSb/ $Al_{0.15}In_{0.85}Sb$ quantum well) at 1.5 K are $4.1 \times 10^{11}\ cm^{-2}$ and $8 \times 10^4\ cm^2/Vs$. The mobility mean free path of $\ell_e = \hbar(\sqrt{2\pi n})\mu / e = 0.84\mu m$ is deduced from the measured mobility and density of 50 μm wide Hall bars at 1.65 K and 1.5 K respectively, for both the samples. The Fermi wavelength for s697 (at 1.65 K) and s842 (at 1.5 K) is 0.05 μm and 0.04 μm respectively. The Fermi energy for s697 at 1.65 K and for s842 at 1.5 K is 40 meV and 70 meV respectively.

4.4 Sample Preparation

4.4.1 Fabrication of Hall Bar

The sample is cleaved into 7mm x 9mm shape using a scriber. Many Hall bars are fabricated on this piece by the method given in Appendix 3. An optical microscope picture of a Hall Bar is shown in Figure 3.2.

4.4.2 E-Beam Lithography, Reactive Ion Etching

Leaving a few Hall bars, the in-plane gates of different channel widths (0.2, 0.3, 0.4, 0.5 and 0.65 μm) were then defined on the other Hall bars by electron beam lithography and

Reactive Ion Etching (RIE). The devices were fabricated with RIE depths of 200, 220, 240 and 700 nm. Figure 4.1 shows the SEM pictures of two types of quantum point contacts defined on the Hall bar (optical microscope picture of a Hall bar is also shown). Type 1 has trenches etched at 90^o to each other and the type 2 devices have etched trenches aligned at 45^o to each other.

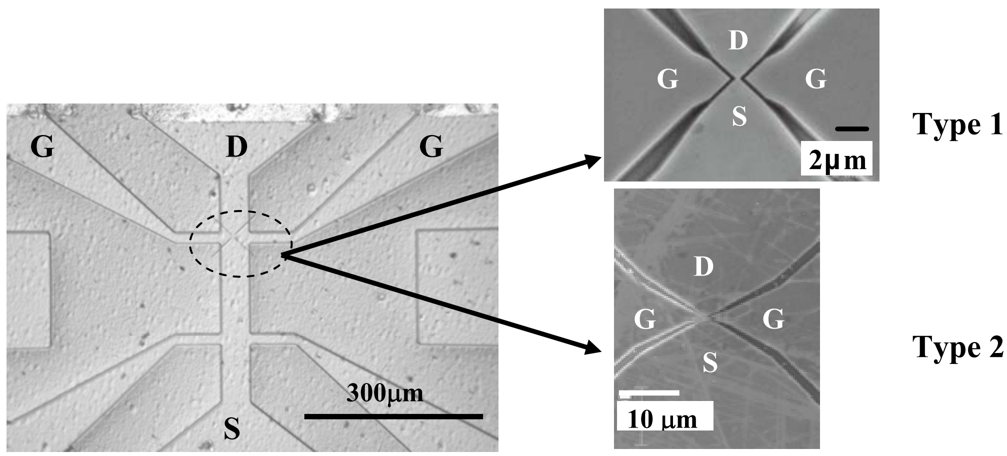

Figure 4.1: Nomarski optical microscope picture of a Hall bar with SEM pictures of the two types of in-plane gate devices. The gates (G), source (S) and drain (D) are indicated on each device.

4.4.3 Ohmic Contact

Ohmic contact on $InSb/Al_{0.09}In_{0.91}Sb$ structure were made by evaporation of Indium on the pads of the Hall bar and subsequent annealing at 225 ^{0}C for 5 m in a mixture of H_2 (20%) + N_2 (80%). For the $InSb/Al_{0.15}In_{0.85}Sb$ structure, AuGeNi (80%, 10%, 10%) alloy was thermally evaporated on the contact pads to make ohmic contact. No subsequent annealing was required.

4.4.4 Header and Wiring

The big piece was then scribed and separated in to 1.2 mm x 1.2 mm devices. Each device was then mounted on a header using epoxy. For effective bonding of the sample to the header, the header was heated in the oven at 110 ^{0}C for 1 h. The sample was wired to the contact pads on the header by 99.99% Au wires using a wire wedge bonder. Figure 3.4 shows a sample mounted and wired on a 8-pin header.

4.5 Experimental Setup

The magneto-transport experiments were performed at NTT Basic Research Laboratories. The experimental setup used for quantum point contact measurements consists of Oxford He cryostat, 8T super-conducting magnet, Oxford Intelligent superconducting magnet power supply IPS$^{120\text{-}10}$, Oxford Intelligent level meter ILM^{210}, Oxford Intelligent temperature controller ITC^{503}, HP4142B Modular DC source/monitor and SR560 low noise preamplifier. The cryostat and the magnet were cooled down to 4.2 K by liquid ^{4}He. The temperature of the sample was further reduced to 1.5 K by pumping on ^{4}He using a rotary pump.

4.6 Gate Leakage

First of all, the leakage through the gate is measured. The gate (*G*) voltage is applied with respect to the Drain (*D*) and the current from *G* to *D* (I_{GD}) is measured. Figure 4.2 shows the setup for measuring gate leakage. The range of V_G is then selected to be the values for which I_{GD} is negligible (no leakage).

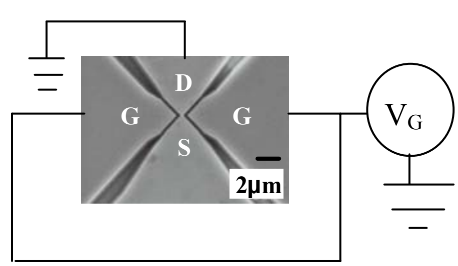

Figure 4.2: SEM image of the 0.4 μm QPC (N0710H: structure s842). The connections for measuring gate leakage are also shown.

4.7 Measurements on Devices of Type 1

Figure 4.3 (a) shows the gate leakage through the lithographically defined 0.3 μm device (N0710G, s842) in the first cooldown cycle. After this measurement, the contact to the pad came loose and the device had to be removed from the cryostat. The compliance current was set to 10 nA. Figure 4.3 (b) shows the results for gate leakage in the second cooldown cycle of the device. As is seen, the gate leakage increased for subsequent cooling cycle of the same device. This indicates the importance of keeping sample cool until all the critical measurements are taken.

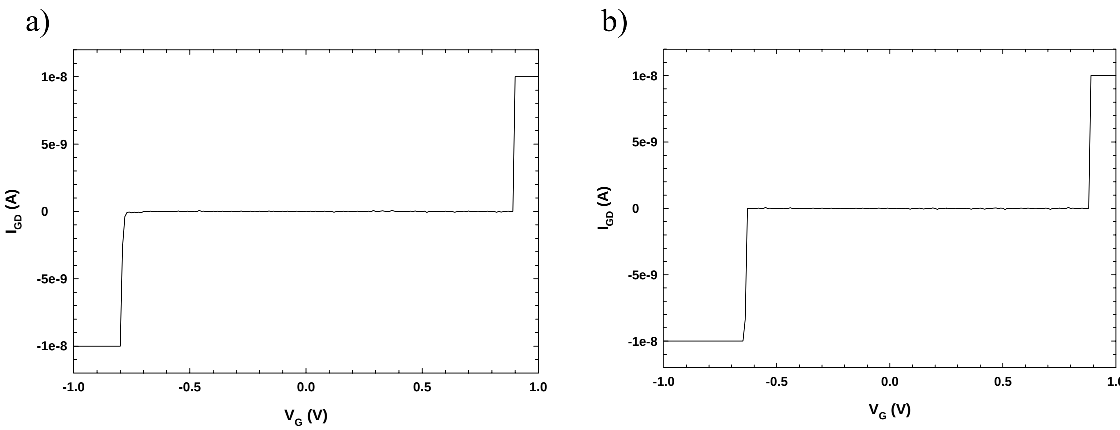

Figure 4.3: The leakage current through the 0.3 μm device (N0710G: structure s842) is shown for the a) first cooldown and b) second cooldown cycle. The leakage current has increased in the second cooldown.

4.7.1 Source Drain Resistance at Zero Magnetic Field

In initial experiments, QPC devices of type 1 were fabricated on sample 1 with RIE etch depth of 240 nm and channel widths of 0.3, 0.5 and 0.8 μm. All these devices were pinched off at zero gate voltage. The second and third set of devices fabricated on sample 1 had RIE depth of 200 nm and 220 nm respectively. The channel widths were 0.5, 0.8, 1.1, 1.4, 1.7 and 2 μm. Although, the channel was not pinched off at zero gate voltage but the gate leakage occurred close to zero gate voltage. The channel width could not be changed by varying the gate voltage.

The next measurements were performed on QPCs of type 1 devices fabricated from structure s697 and s842. The devices had widths ranging from 0.2 to 0.65 μm. The depth for the samples fabricated on s842 was 0.7 μm. as confirmed by AFM. The RIE depth for s697 devices was 0.24 μm. Although it should be mentioned that the depletion effects of the sidewall of the etched trenches of the gate can make the effective width of the channel much smaller than the width of the etched mesa. Figure 4.4 shows the connections for the conductance measurements. The gate voltage V_G is applied to both gates. The V_G is varied in the range where there is no gate leakage (see Sec 4.6). The voltage measured across the source-drain, V_{SD}, gives the resistance R_{SD}. The device with lithographically defined 0.65 μm-wide QPC fabricated on both s697 and s842 did not show any conductance quantization.

Figure 4.5 shows the two terminal resistance of N0707J (0.5 μm, s697) as a function of applied V_G at zero magnetic field. Three plateaus can be seen. This resistance contains the serial contribution from the 2D regions adjacent to the point contact and the ohmic contacts. The values of resistance indicate that the plateau corresponding to e^2/h (~26 kΩ) or $2e^2/h$ (~13 kΩ) are not present in the given gate voltage range. It is difficult to guess the series resistance to subtract in this device. Therefore, only the raw data is shown here which clearly indicates quantization at zero field.

Figure 4.6 shows the first and the third cooldown result of R_{SD} for N0710G (0.3 μm, s842). A dc source to drain current (I_{SD}) of 0.1 μA was applied while V_G was varied. The gate leakage current was less than 1 nA when $-0.7V < V_G < 0.9V$. Four plateaus can be seen. The importance of the cooldown cycle of the sample can also be observed in the conductance plots of Figure 4.6 (a, b). The gate leakage was found to increase with each subsequent cooling cycle of the sample. The plateau around 17 kΩ seen clearly in (a) is barely visible in (b). The S-D resistance during the fourth cooldown is shown in Figure 4.7.

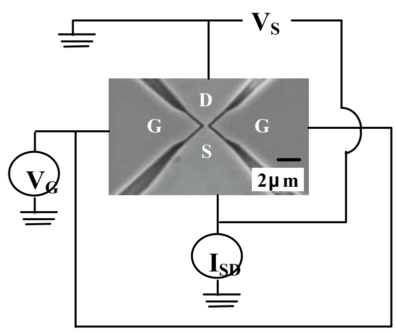

Figure 4.4: SEM image of the QPC with the connections for making the conductance steps measurements. Gate voltage (V_G) is applied to the in-plane gates and the current I_{SD} passes from source (*S*) to drain (*D*). Voltage across source-drain, V_{SD}, is measured.

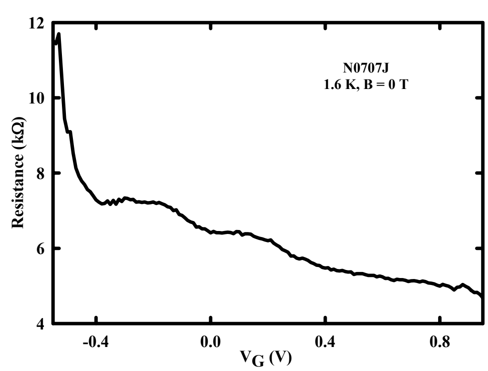

Figure 4.5: Raw data for the resistance measured for QPC as a function of V_G at zero B-field and 1.5 K for N0707J (0.5 μm: s697).

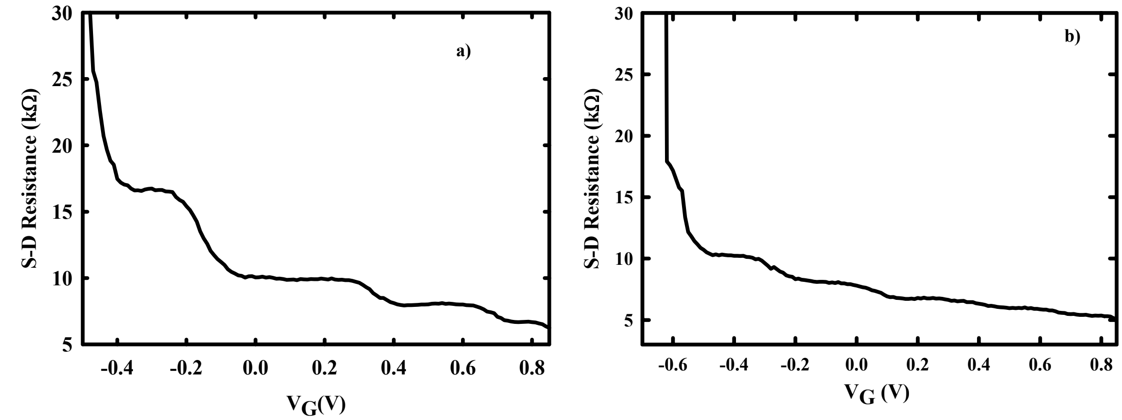

Figure 4.6: Source-drain resistance, R_{SD} as a function of gate voltage for N0710G (0.3 µm wide, s842) at 1.65 K during a) first cooldown and b) third cooldown cycle. The gate leakage has increased in third cooldown and therefore the plateau width around 17 kΩ is narrower in b).

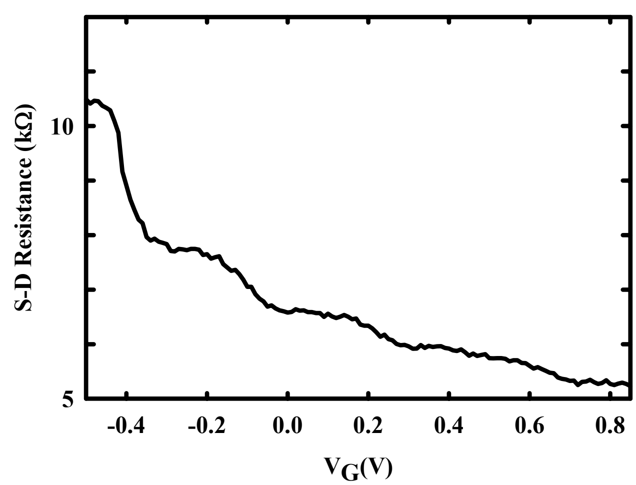

Figure 4.7: Source-drain resistance, R_{SD} as a function of gate voltage for N0710G (0.3 µm wide, s842) at 1.65 K during fourth cooldown.

4.7.2 Series Resistance and Conductance Quantization

The conductance of the point contact, as measured experimentally, has contributions from the background resistance. The determination of this series resistance, R_s can be difficult. The largest contribution to R_s is from the ohmic contacts. Also, R_s may be gate voltage dependent and can vary in similar devices because of the differences in gate geometries, inhomogenities in layer structure and trapping charges. It is difficult to guess correct R_s for N0707J and N0710G. When a series resistance of 3.4 kΩ is subtracted from the first cooldown cycle result, the conductance as a function of gate voltage for N0710G is shown in Figure 4.8 (a). The conductance is quantized in units of $2e^2/h$. These observed steps are the first experimental evidence of conductance quantization in InSb devices.

Figure 4.8 (b) shows the conductance quantization for fourth cool-down cycle of N0710G. The exactness of the quantization and the flatness of the plateau are not as accurate as for the first cool-down cycle. The deviation from exact quantization of the higher subbands indicates that the series resistance may be gate voltage dependent. Due to the limit of experimental gate voltage range, there was no indication of 0.7 structure in either N0707J or N0710G.

A discrepancy arises in our devices in deducing the correct series resistance at 0 T. Figure 4.9 a) shows the conductance plot at 0 T with various series resistance (listed in the legend) subtracted from the third cooldown data of N0710G. If a value of 1.6 kΩ is subtracted then there is fair alignment of plateaus in the units of e^2/h indicating the spin-split levels. For the rest of the series resistances subtracted, the plateaus are not evenly spaced. The series resistances are also subtracted from the first cooldown cycle data, Figure 4.9 b). The alignment with spin split levels can be seen at 1.6 kΩ. This indicates the importance of the contribution of series resistance in these two terminal measurements.

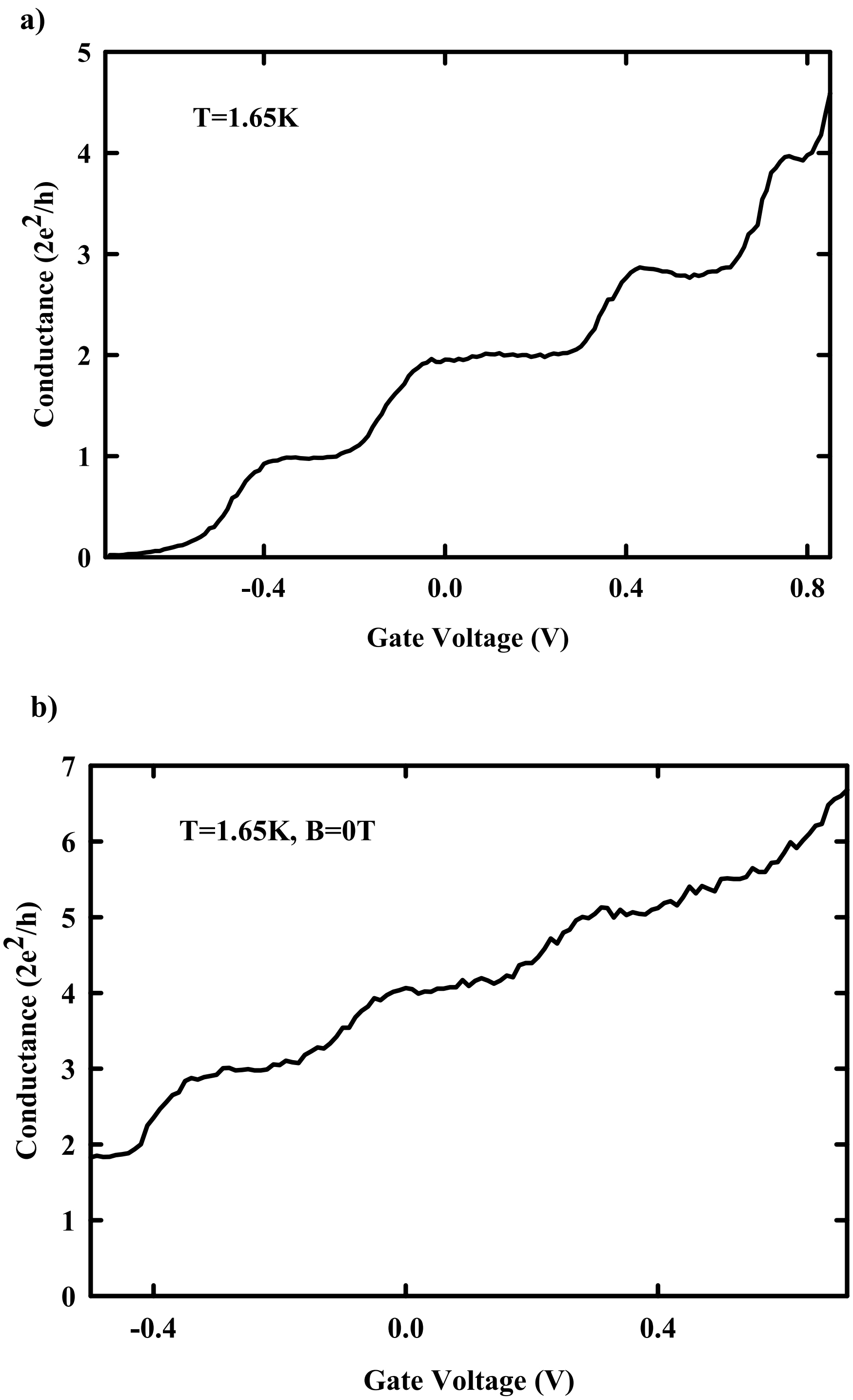

Figure 4.8: Conductance steps as a function of V_g at 0 T and 1.65 K as observed in a 0.3 µm in-plane gate QPC (N0710G, s842) fabricated on an $InSb/Al_{0.15}In_{0.85}Sb$ single quantum well during a) first cooldown and b) fourth cooldown of the sample.

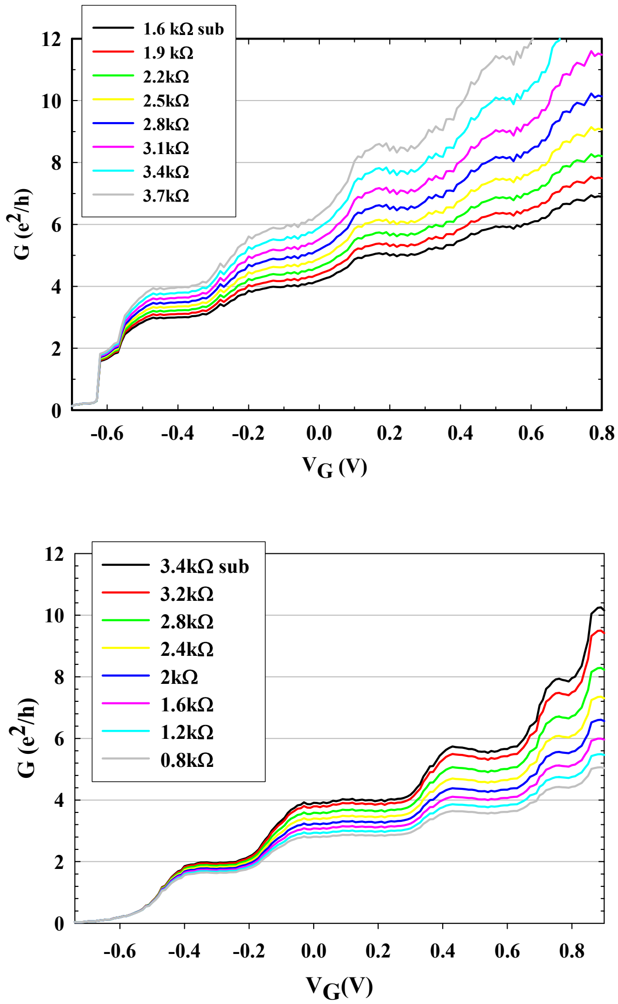

Figure 4.9: The conductance plot for N0710G at 0 T for various series resistances subtracted from the raw data during a) the third cooldown cycle and b) the first cooldown cycle. R_s values subtracted for respective curves are listed in the legends.

4.7.3 AC versus DC Current

Comparison between the raw data for two terminal resistance as a function of V_G when ac and dc source drain current, I_{SD} (= 0.1μA) is passed through the N0710G device at 1.65 K is shown in Figure 4.10. The readings were taken during the fourth cool-down. Most of the experiments in literature have been performed using ac I_{SD}. From our data we can see that quality of the result is almost the same in both the case. For all the rest of the experiments we inject dc I_{SD} through the device.

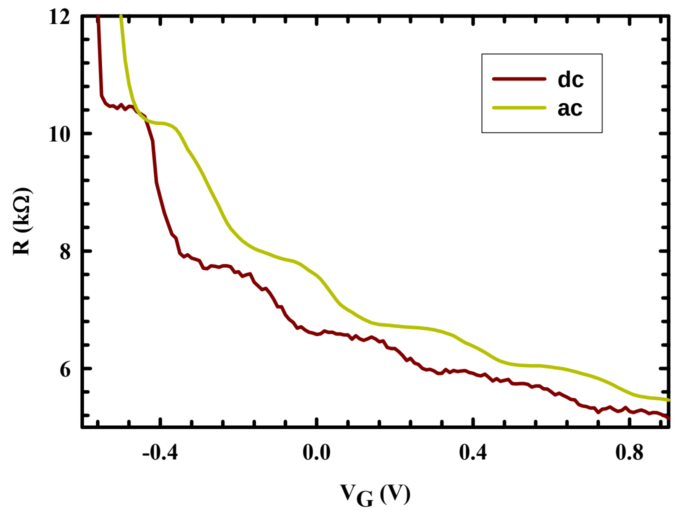

Figure 4.10: Comparison of raw data of two terminal resistance as a function of V_G when ac and dc I_{SD} is passed through N0710G device at 1.65 K.

4.7.4 Perpendicular B-field

The measurements were also taken when magnetic field is applied perpendicular to the plane of the channel. The setup is shown in Figure 4.11 (a). The raw data for source drain resistance at a few perpendicular magnetic field values for N0710G are given in Figure 4.11 (b). Figure 4.12 shows the comparison between the series resistance subtracted from the perpendicular field data for N0710G and the SdH oscillation and QHE results for Hall bar fabricated on s842. A low *B*-field the results do not match but at higher fields, series resistance assumed is reasonable except near Landau level fillings of 4 and 3. Conductance of N0710G (0.3 μm, s842) as a function of V_G at a few perpendicular *B* values after subtracting R_s during the third cool-down is shown in Figure 4.13. The plots are offset for clarity. The shift of plateaus to more positive gate voltage with increasing magnetic field can be seen in the plot. This is the magnetic depopulation effect. As the magnetic field is applied, the subband spacing increases. Larger variation of gate voltage is required to populate or depopulate a subband. As a result, the plateaus widen. Moreover, the plateaus are seen to become more flat at higher *B* because of the decrease in the backscattering due to the impurities in and near the QPC.

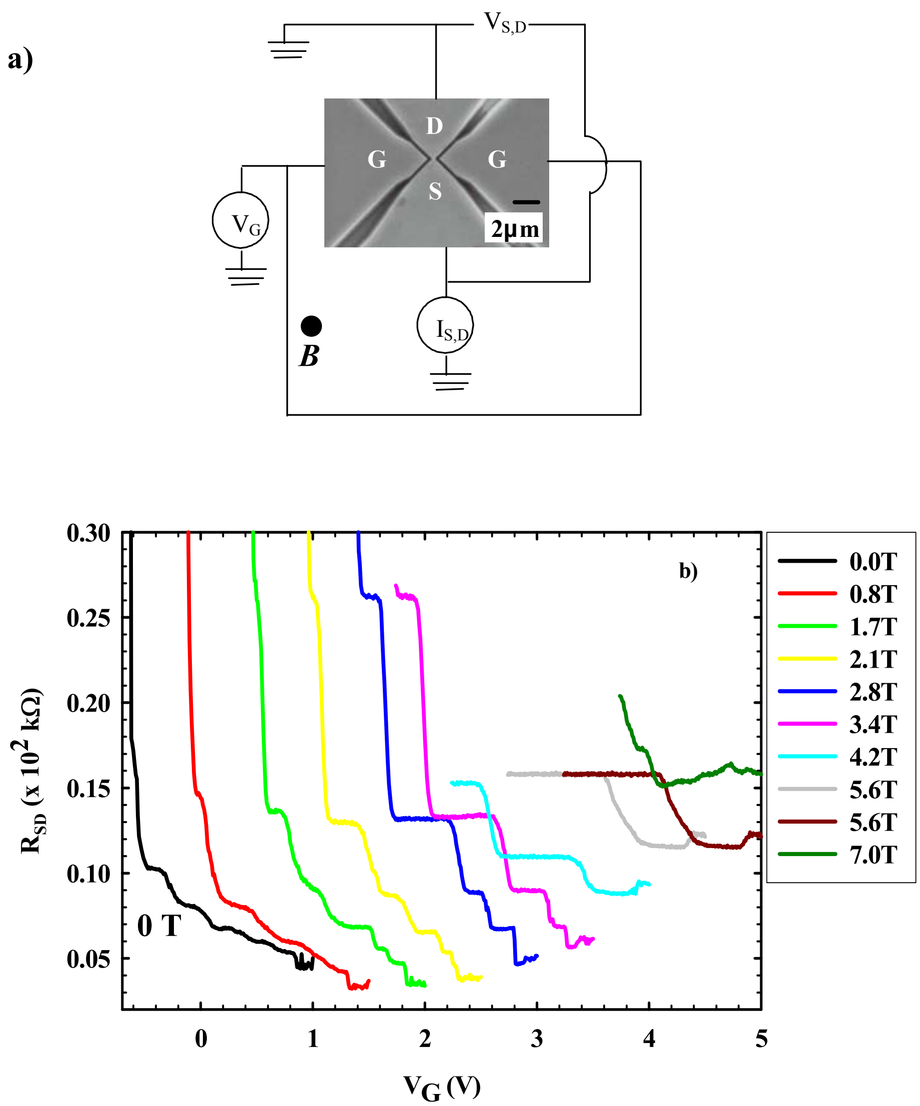

Figure 4.11: a) The setup for measuring the R_{SD} as a function of V_G. The B-field is applied in the layer growth direction. b) Raw data for R_{SD} as a function of V_G for various $B_\perp$ values. The consecutive graphs after 0 T data are offset in theV_G-axis direction for clarity.

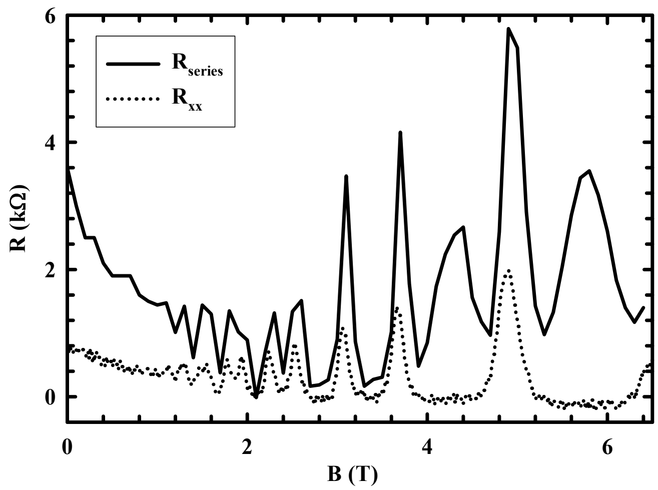

Figure 4.12: The comparison between the series resistance subtracted from the perpendicular field QPC data (N0710G) and the longitudinal resistance at 1.5 K measured in a Hall bar (s842).

An interesting feature that can be seen is the appearance of additional plateaus in between the B = 0 steps around 0.9 T. These steps correspond to odd integer subband indices. The odd integer plateaus can be clearly seen in the data at $B = 1.7\ T$. These conductance steps ($G = N\ (e^2/h)$ where $N = 1, 3, 5$.....) indicate the lifting of the spin degeneracy. This is a lower magnetic field than reported for resolving spin splitting in QPCs made from GaAs (~6 T in Ref. 93) or InAs (2.5 T in Ref. 65). This result indicates that various interesting phenomenon can be observed at reasonably achievable magnetic field values in InSb based devices underlining the advantage of using this material system.

Figure 4.14 shows G as a function of V_G for the perpendicular B-field sweep from 0 to 4.3 T during the third cool-down cycle. The plots are offset by 140% in V_G - axis direction for clarity. Clearly the onset of Zeeman splitting can be seen around 0.9 T. The flatness of the plateaus is seen to improve with increasing magnetic field. Moreover, the number of plateaus decreases with increase in B indicating the depopulation of subbands.

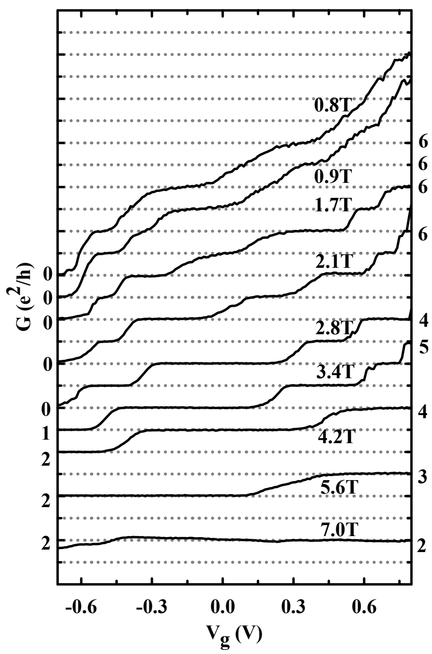

Figure 4.13: Conductance as a function of V_G for various values of perpendicular *B* (0.8 to 2.8 T) for N0710G (0.3 μm: s842) at 1.6 K. The plots have been offset in *G* for clarity.

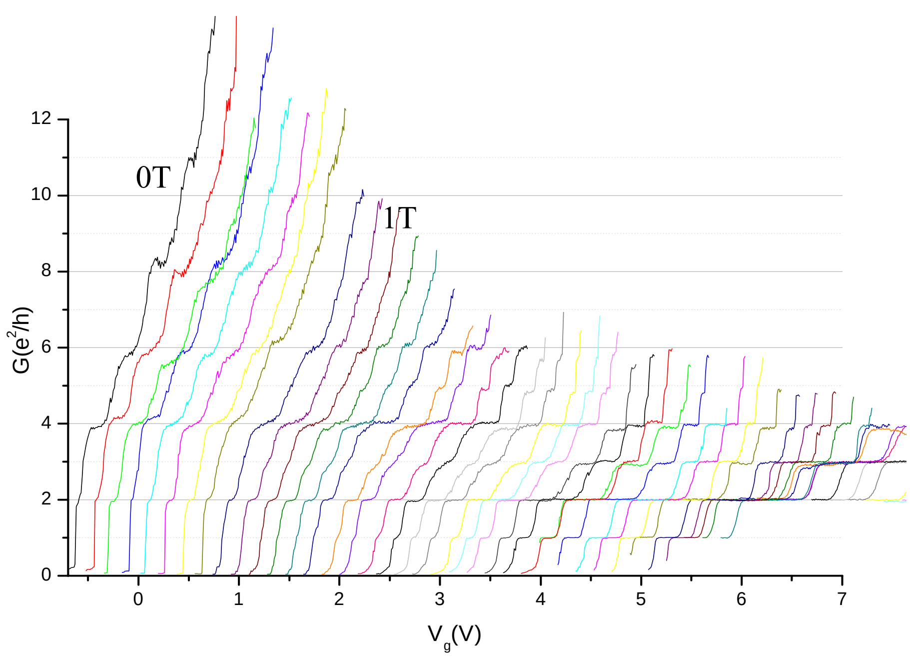

Figure 4.14: Conductance as a function of V_G for various values of perpendicular *B* (0 to 4.3 T) for N0710G at 1.6 K. The plots have been offset by 140% for clarity.

The contour plot for the data from 0 to 3 T is shown in Figure 4.15. The first derivative of conductance, dG/dV_G is plotted as a function of V_G and B. The number N of occupied 1D-subbands is also labeled in the plot. As the B field increases, ω_c increases. This gives the curvature to the subband as is expected from Eq. 4.6. Qualitatively, the data from 0 to 2 T agrees with this 1D eigen energy equation.

Figure 4.16 shows the contour plot for N0710G from 0 to 6.1 T. At higher fields > 2.5 T, there are steep dips with minima at $B \sim 4\ T$. These dips have not been reported in any other material system. The explanation for this dip is yet to be determined. With each dip the plateau index increases indicating a repopulation effect. If the *g*-factor in a 1D system is enhanced (as has been reported for GaAs 1D system in Ref. 75) then it is possible that the slope of E vs B of a higher lying 1D subband changes sign. This may imply that at certain B-fields the subband may fall below the Fermi level increasing the number of occupied subbands and hence the repopulation effect. This interesting phenomenon was observed in only one device. Further experiments on other QPCs are still underway to confirm this behavior.

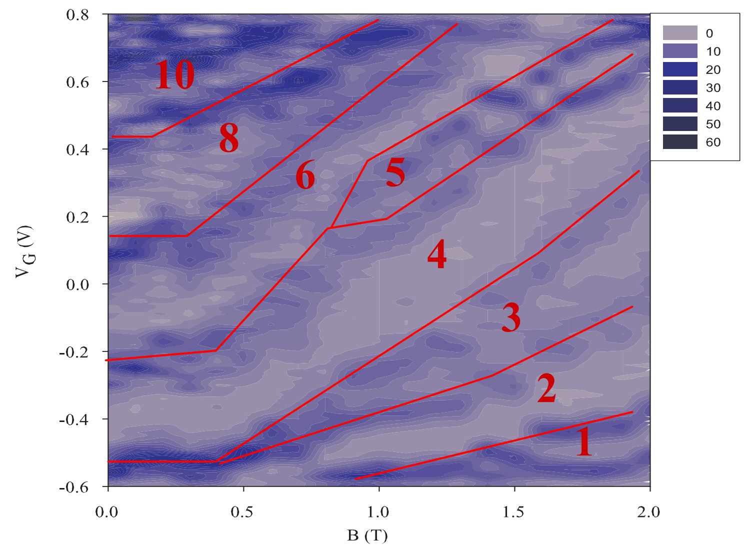

Figure 4.15: Contour plot of first derivative of *G* with respect to V_G is shown as a function of V_G and $B_\perp$ for N0710G at 1.5 K. Subbands occupation, *N = 4, 6 and 8* are clearly seen at 0 T. The data for $V_g > 0.5\ V$ and $< -0.6\ V$ is not clear due to the onset of gate leakage. The lines are guide to eye.

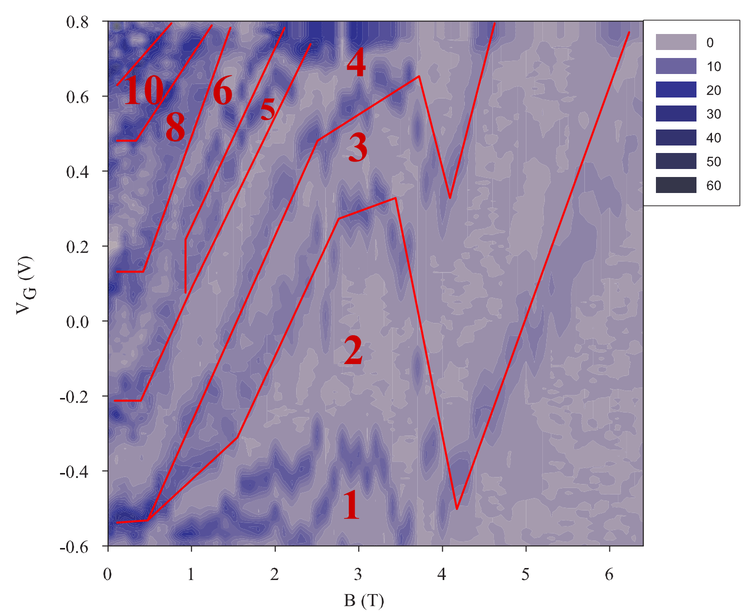

Figure 4.16: Contour plot of first derivative of *G* with respect to V_G as a function of V_G and $B_\perp$ for N0710G. The range of magnetic field is 0 to 6.1 T. The lines are guide to eye.

4.7.5 Parallel B-field

The measurements were also taken when magnetic field is applied parallel to the plane of the channel and to the current direction, Figure 4.17. Figure 4.18 shows the series resistance subtracted from the parallel field raw data.

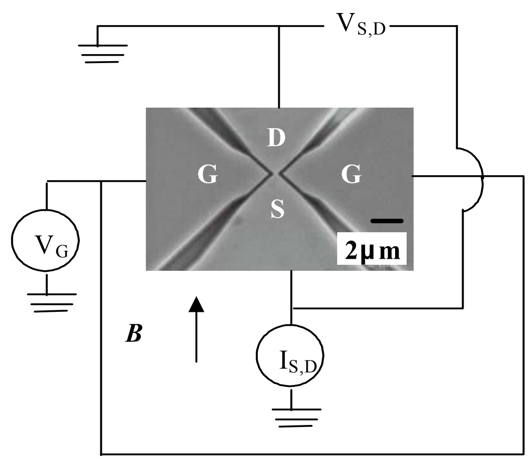

Figure 4.17: The setup for measuring source-drain resistance (R_{SD}) as a function of gate voltage (V_G) is shown. B-field is applied in-plane and parallel to the direction of the current. The conductance G, is then determined by subtracting series resistance from R_{SD}.

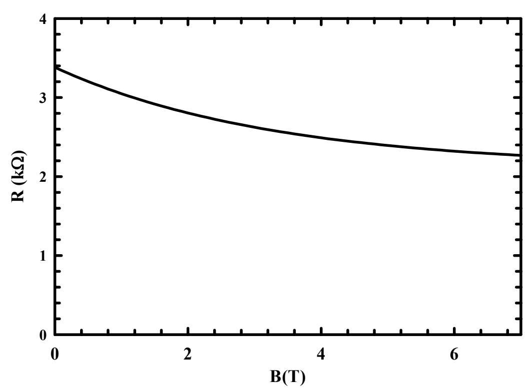

Figure 4.18: Series resistance subtracted from the parallel field QPC data (N0710G) as a function of B-field.

Conductance steps in N0710G (0.3 μm, s842) as a function of V_G is shown in Figure 4.19 for various values of B during the fourth cool-down cycle. The B-field intervals in each graph of Figure 4.19, is 0.1 T. The plots are offset by 100% in the G-axis direction for clarity. The quality of the data can be seen to have deteriorated, as this is the fourth cool-down cycle for the device.

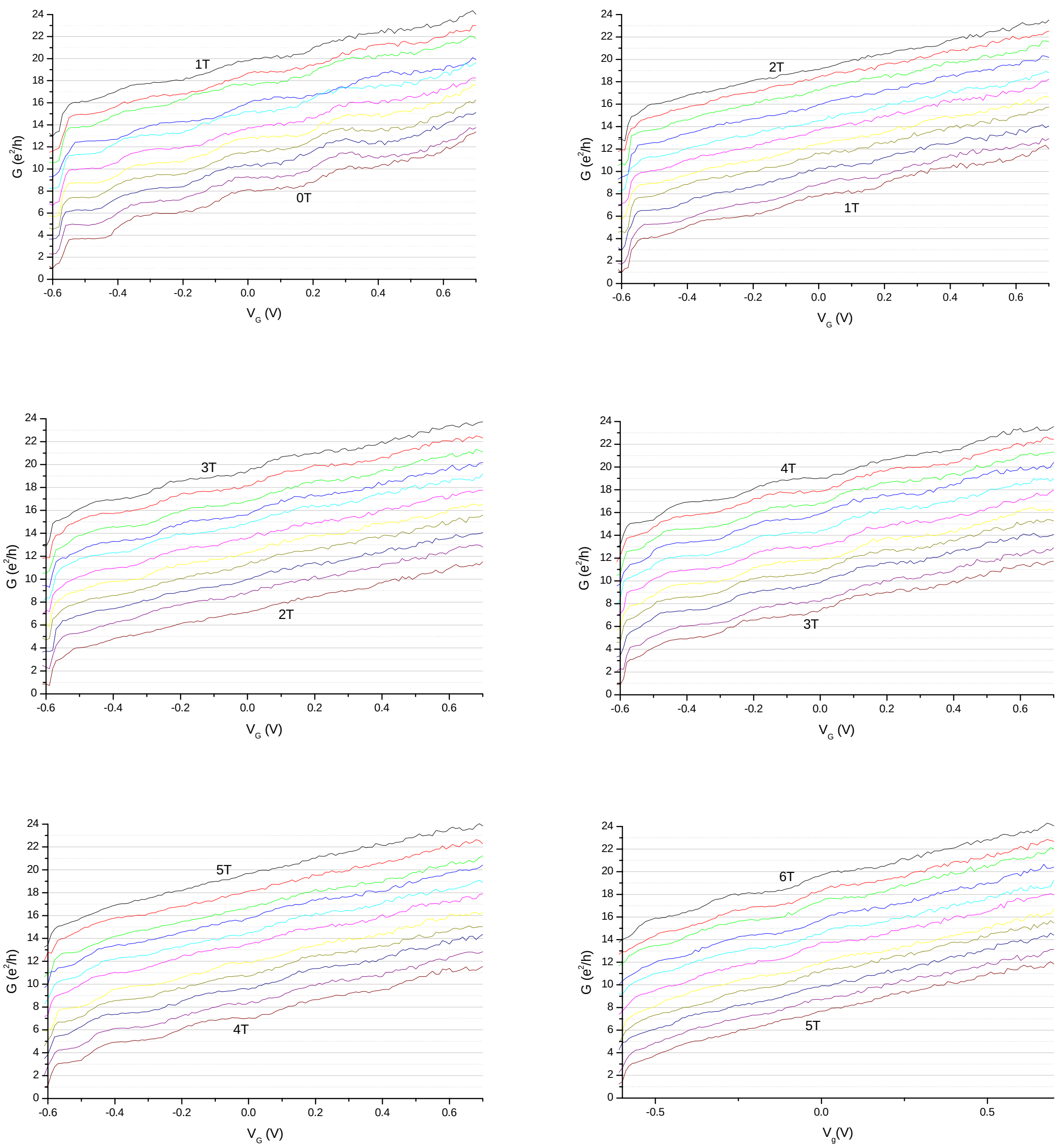

Figure 4.19: Conductance, *G*, for N0710G as a function of V_G for various values of parallel B-field (0 to 6 T). The plots are offset by 50% in G-axis direction. In each plot the B-field is increased in steps of 0.1 T.

The contour plot for the N0710 G device data for parallel B-field from 0 to 7 T after subtracting the series resistance is shown in Figure 4.20. The first derivative of conductance, dG/dV_G is plotted as a function of V_G and $B_{||}$. The number of occupied 1D-subbands is also labeled in the plot. It should be mentioned here that the data at 6.2 and 6.7 T is due to the experimental error and should be neglected. Large $B_{||}$ lifts the electron spin degeneracy causing conductance plateaus in units of e^2/h around 3 T. It also leads to neighboring subbands crossing when $g\mu_B B$ equals the zero magnetic field subband energy spacing. Level crossings are observed around 3 T. The subband spacing, taking the *g*-factor of bulk InSb, can be estimated roughly to be 10 meV (= $g\mu_B B$). After the crossing, the conductance is quantized in odd multiples of e^2/h. A further increase in $B_{||}$ causes the crossing of next nearest 1D subbands around 6 T. The conductance is then quantized back to even multiples of e^2/h.

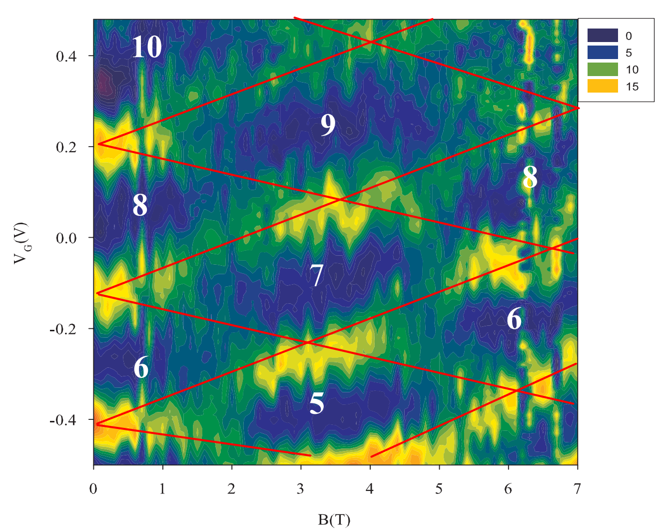

Figure 4.20: Contour plot of dG/dV_G as a function of $B_{||}$ and V_G. Level crossings are observed. Due to experimental errors the data for $B = 6.2$ *and* 6.7 *T* should be neglected. The lines are guide to eye.

4.7.6 Temperature Dependence

The temperature dependence for N0710G device was also measured, shown in Figure 4.21. Quantization can be seen up to 11 K above which due to thermal smearing the plateaus vanish. In GaAs, the plateaus are seen up to 30 K [47]. Even though the subband spacing in InSb is expected to be more compared to that in GaAs due to smaller m^*, the quantization in InSb based device persist up to a lower temperature comparatively. The subband energy level spacing can be estimated roughly from the temperature at which quantization disappears. A subband separation of nearly 4 kT is required to clearly observe the plateaus. This gives a subband spacing of nearly 3.8 meV for our device.

a) b)

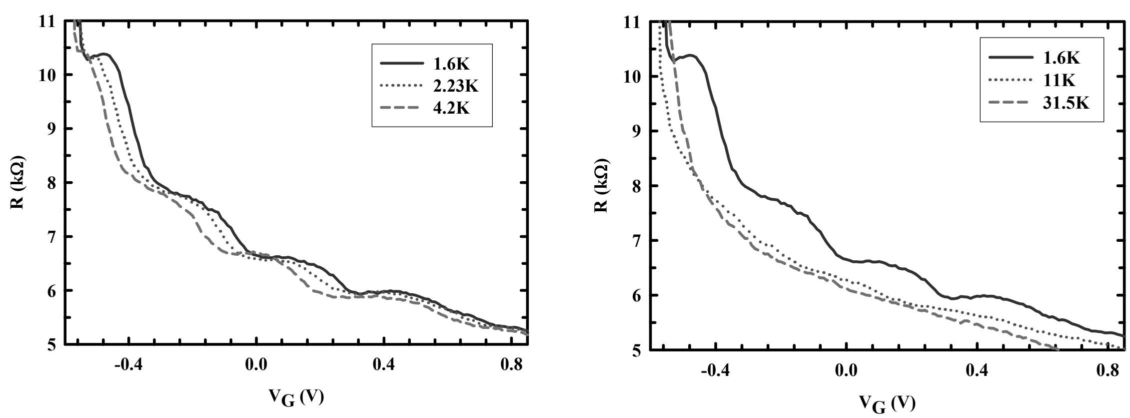

Figure 4.21: Raw data for QPC two terminal resistance is shown for N0710G at (a) 1.6 to 4.2 K and at (b) 1.6, 11, 31.5 K. Weak plateaus can still be seen at 11 K but they disappear at 31 K.

4.7.7 Dependence on Source Drain Current

The current through the source drain, I_{SD}, was also varied for N0710G. The raw data for resistance is shown in Figure 4.22 at various I_{SD} values.

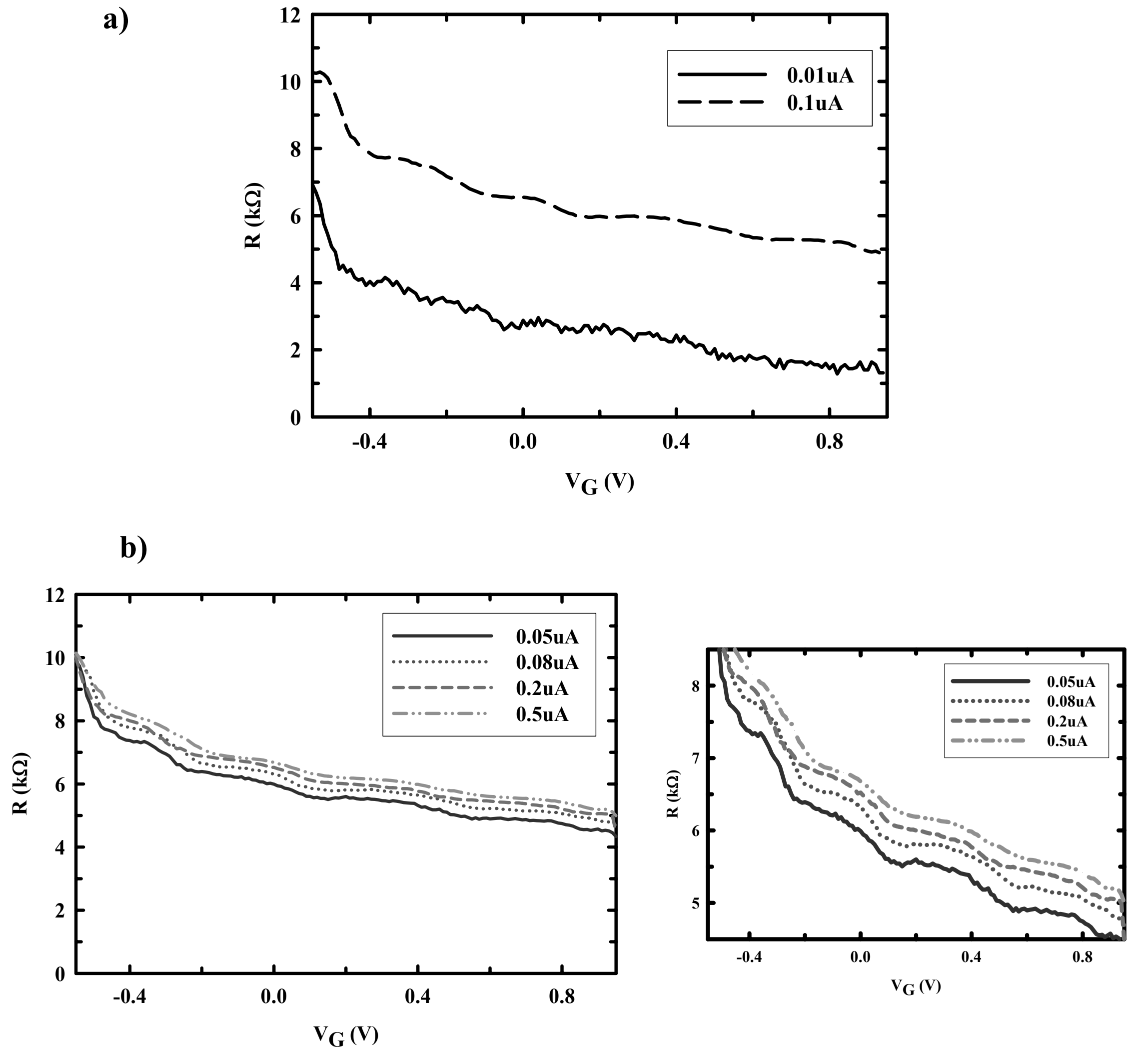

Figure 4.22: The raw data of source-drain resistance as a function of V_G for N0707J at (a) 0.01 and 0.1 μA and (b) 0.05 to 0.5 μA source drain current at T =1.65 K.

4.8 Measurements on Devices of Type 2

Similar transport measurements were performed on 0.2 and 0.3 μm-wide type 2 devices fabricated from structure s842 (for device geometry see Figure 4.1). First, the gate leakage was measured. Keeping the gate voltage within the range of no-gate-leakage the measurements were carried out in the absence and presence of perpendicular B-field. Figure 4.23 shows the quantization of conductance for a 0.3 μm device (N0220A) in perpendicular B-field. The depopulation of the plateaus can be seen with decreasing gate voltage at certain *B* and with increasing *B* respectively. The plateaus at odd integers start to appear around 1 T. Figure 4.23 also shows the conductance plateaus in the B-field range of 2 to 3 T. There is no sign of repopulation effect as observed in the sample N0710G. The quality of the device deteriorated considerably with the next cooling cycle. The gate leakage increased as well.

4.9 Yield

Table 4.1 shows the yield of devices fabricated in type 1 and 2 geometry. In the table, 'total' is the total number of samples fabricated with widths *L*. The data for these devices are then labeled in four categories. The 'depleted' devices were pinched off for all gate voltages even though there was no gate leakage. For bad devices, even though the devices were not pinched off, there was only one plateau or no plateau seen. A few plateaus were seen in 'OK' devices but it was hard to assign numbers to them. Even though further magnetotransport experiments could be performed during the first cool-down, it was extremely hard to guess the series resistance. The quality of these devices deteriorated significantly in the next thermal cycle. The 'good' device implies that the plateaus quality was reasonable and further experiments could be performed during more than one cool-down cycle. All the data shown earlier in this chapter is from these good devices.

From Table 4.1, it can be clearly seen that the yield of good devices is poor. This along with the fact that the quality of sample deteriorates with cooling cycle, hampers further experiments on these devices. The degree of flatness of plateaus and the sharpness of the steps varied among devices even of the same design. This suggests that any variation in the confining potential defining the shape of the constriction is very critical. This variation can be due to the doping inhomogenities in the heterostructure and gate geometry.

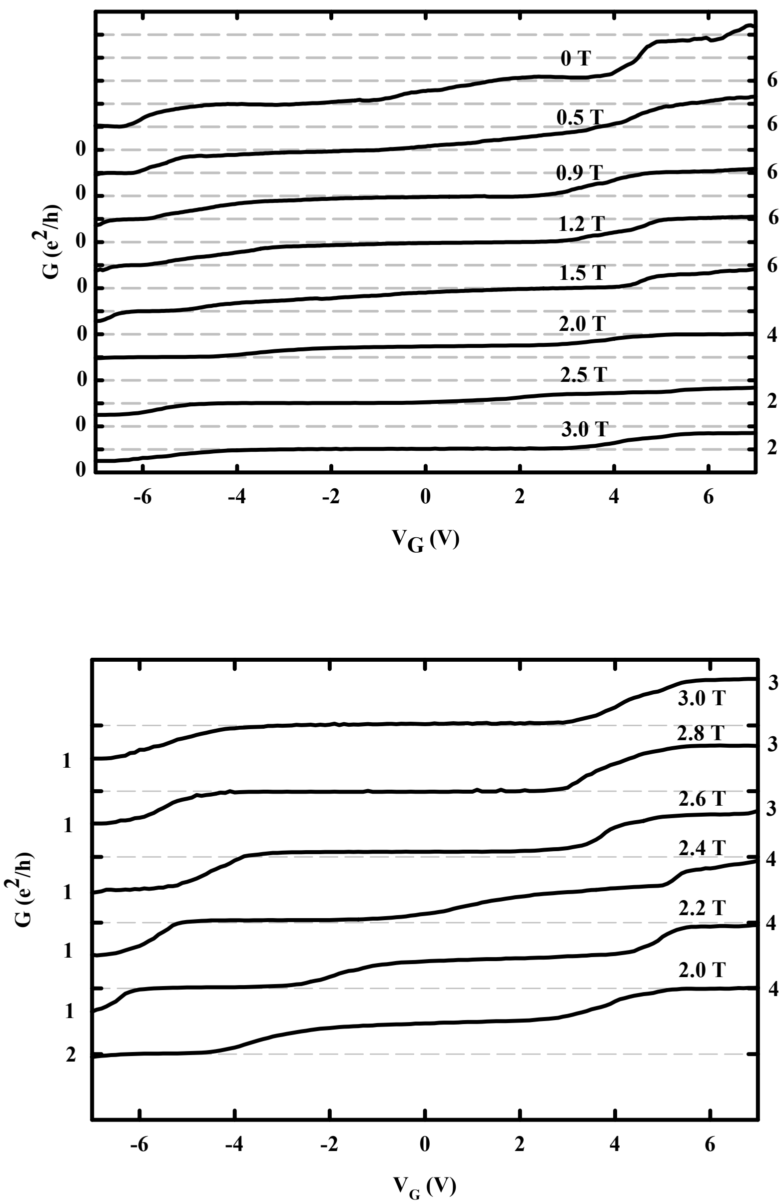

Figure 4.23: Conductance as a function of gate voltage at 4.2 K for N0220A (0.3 μm device) during second cooldown. The plateaus at odd integers start to appear around 1 T and can be clearly seen in the figure at 2 T.

Type 1 Devices

L (μm)	Total	Depleted	Bad	OK	Good
0.3	2	0	1	0	1
0.4	3	0	3	0	0
0.5	3	0	1	2	0

Type 2 Devices

L (μm)	Total	Depleted	Bad	OK	Good
0.2	6	5	1	0	0
0.3	12	4	5	2	1

Table 4.1: The yield of devices fabricated with type 1 and 2 geometries on s842.

Chapter 5
MESOSCOPIC MAGNETORESISTORS, SPIN EFFECTS IN InSb QUANTUM WELL

5.1 Introduction

The effort to increase the data storage capacity of hard disk drives has been ongoing for several decades [94] so that commercially available drives can now deliver areal densities of order 15 Gb/in.^{2} [95]. A critical component in such storage systems is the read-head sensor, the modern versions of which are based on giant magnetoresistance (GMR) [96] or tunneling magnetoresistance (TMR) [97]. Both GMR and TMR derive from spin-dependent effects in layered magnetic metals, and are therefore subject to the attendant pheonomenon of magnetic noise (mag-noise) [98] which appears to represent a fundamental challenge to the scalability of such magnetic MR sensors to areal densities much above 100 Gb/in.^{2}. The first part of this chapter shows that a read-head sensor based on the recently discovered extraordinary magnetoresistance (EMR) effect [4] in nonmagnetic narrow-gap semiconductors provides a viable route to ultra-high-density recording at areal densities of order Tb/in.^{2} [99]. For this study[1], InSb based structures were grown at OU and fabricated into read sensors at NEC Research Institiute and NEC Fundamental Research Laboratories. The magnetoresistance measurements on the device were also performed by researchers at NEC.

[1] This work has been published in S.A. Solin et al. IEEE Transactions on Magnetics 38, 89 (2002) and S.A. Solin et al. Applied Physics Letters 80, 4012 (2002).

Recently there has been growing interest in the study of spin phenomena in semiconductor heterostructures. A new field, "spintronics" has emerged for the purpose of developing devices combining both the charge and spin degrees of freedom. In particular, spin splitting in heterostructures caused by bulk inversion asymmetry and structural inversion asymmetry (SIA – often called Rashba splitting), has attracted much attention. Understanding the spin-orbit interaction caused by SIA in heterostructures, which leads to zero field spin splitting, is important for developing spin-based devices. It has been theoretically shown that lack of inversion symmetry and a small energy gap are the two mechanisms responsible for electric-dipole spin resonance.

Because of its large effective *g*-factor and large predicted Rashba splitting [100], InSb is potentially well-suited for use in spintronic devices. Furthermore, the spin and cyclotron resonances in this material occur at far infrared frequencies at an accessible range of magnetic fields, making InSb a good material for investigating certain spin phenomena. The second part of this chapter focuses on magneto-optical experiments[2] that are made possible by the large spin-splitting in InSb quantum wells: spin-resolved cyclotron resonance (SRCR), spin-resolved avoided-level crossings, and electron spin resonance (ESR).

5.2 Extraordinary Magnetoresistance (EMR)

The magnetoresistance (MR) of a material object contains a physical contribution from the magnetic field dependence of the material parameters and a geometric contribution from the dependence of the current path and output voltage on the sample shape and electrode configuration [101]. To date, only two classes of magnetic materials, artificially layered metals which exhibit either giant MR (GMR) or tunneling MR (TMR) and the manganite perovskites which exhibit colossal MR (CMR) have been considered serious candidates in the effort to improve the room temperature (RT) performance of MR sensors. For both of these classes, the physical MR dominates. In contrast, non-magnetic narrow-gap semiconductors containing patterned metallic inhomogeneities (shunts), exhibit RT geometric extraordinary MR (EMR) that can be larger than the physical MR of other (magnetic) materials [4, 102, 103].

The EMR effect results from orbital rather than the spin motion of the charge carriers and is due to the magnetic-field-induced deflection of current from a conducting metallic inhomogeneity or shunt embedded in the host semiconductor. Since the conducting inhomogeneity is effectively an equipotential surface, the electric field E is everywhere normal to the semiconductor-metal interface. At zero magnetic field current flows parallel to the electric field and the inhomogeneity acts as a short circuit thus lowering the resistance of the semiconductor-metal composite. However, as the component of the magnetic field that is normal to the current at the interface increases with increasing applied field, the Lorentz force on the carriers causes the Hall angle between the current and the electric field to increase thus reducing current flow into the inhomogeneity the effective conductance of which decreases. This transition in the conductance of the inhomogeneity with field amplifies the MR of the semiconductor-metal composite. In general, $EMR(\Delta B, B_{Bias}) = [R^{eff}(\Delta B+B_{Bias})-R^{eff}(B_{Bias})]/R^{eff}(B_{Bias})$, where $R^{eff}(B)$ is the effective field-dependent resistance measured in a four probe configuration [4], B_{Bias} is the bias field and ΔB is the applied or signal field. For small signals $EMR(\Delta B \rightarrow 0, B_{Bias}) =$

[2] This work has been published in G.A. Khodaparast et al. Physica E 20, 386 (2004).

$[1/R^{eff}(B_{Bias})][dR^{eff}(B)/dB]_{BBias}\ \Delta B$, where $[dR^{eff}(B)/dB]_{BBias}$ is the current sensitivity. In the zero-bias large signal but still low field limit, $\mu\Delta B<<1$,

$$EMR(\Delta B,0) = \frac{R^{eff}(\Delta B) - R_0^{eff}}{R_0^{eff}} = G(\Delta B)[\mu\Delta B]^2 \tag{5.1}$$

where μ is the mobility of the dominant carrier, $G(\Delta B)$ is a geometric factor that depends on the shape, location and physical properties of the conducting inhomogenity and contacts while $R^{eff}(0)=R_0^{eff}$. Clearly, materials with high mobility such as narrow-gap semiconductors are prime candidates for EMR devices.

Among the numerous magnetic sensor applications which might beneficially employ EMR materials one of the most interesting is the read-head sensor for high density magnetic recording. This application requires sensor devices of mesoscopic size. This chapter reports the measurements of EMR effects in mesoscopic structures.

5.2.1 Recording Geometry for Conventional and EMR Read-Heads

The sensing geometries for a conventional read-head sensor and an EMR read-head sensor are shown schematically in Figure 5.1 (a,b). The former uses a vertical plane geometry while the latter would employ a horizontal plane geometry. Because the field from the medium falls off very rapidly with height above the surface, the average field over the vertical surface of the conventional sensor is of order 0.005 T. This is the minimum/relevant field which the sensor must be able to access while producing an acceptable signal to noise ratio. In contrast, because it is very thin in the vertical direction and is therefore closer to the surface, the EMR sensor has a much higher relevant field of order 0.05 T. Since the EMR varies quadratically with field, the higher relevant field provides a significant advantage.

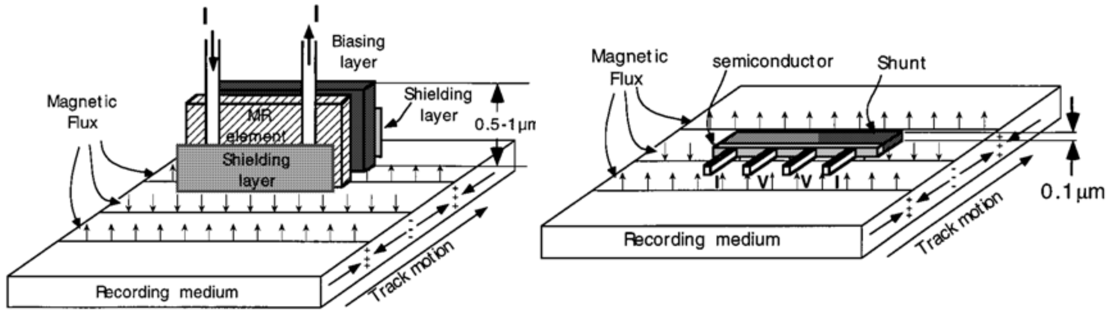

(a) **(b)**

Figure 5.1: a) A schematic representation of a conventional spin-valve GMR recording geometry. b) A schematic representation of an EMR read-head recording geometry. Shielding layers are not shown.

5.2.2 Preparation of Mesoscopic EMR Read Head Structures

5.2.2.1 InSb Quantum Well Structure

In order to selectively access the maximal signal field that is present at or near the surface of a magnetic recording disk it is desirable for the read-head sensor to fly as close as possible to that surface and to be as thin as possible in the direction normal to that surface. For this reason a quantum well heterostructure is used to fabricate EMR read head structures. The quantum well is grown closer to the surface of the heterostructures. Since EMR varies as μ^2 (see Eq. 5.1), higher room temperature mobility is desirable. As a result InSb is an attractive material for EMR device. Layer sequence of an InSb quantum well heterostructure used for fabricating the EMR device is shown in Figure 5.2. The room temperature density and mobility were measured to be $2.7 \times 10^{11}\ cm^{-2}$ and $2.3 \times 10^{4}\ cm^2/Vs$, respectively.

5.2.2.2 Four Contact Mesoscopic EMR Read-Head Structure

To achieve feature sizes of the EMR structures below 100 nm, a multistep electron beam lithography process was utilized by researchers at NEC Fundamental Research

Laboratories. First, a 30 nm thick insulating film of Si_3N_4 was deposited on the heterostructure as a cap layer and macroscopic Au strips for wire bonding were deposited in a pattern that radiated outward from the edges of an 80-μm-square area. Then, a 30-nm thick film of calixarene was spin coated on. Four, 30nm x 3μm, strips were delineated in the calixarene in the corners of the 80 μm square by e-beam lithography. This calixarene and Au strips serve as a mask for RIE of the Si_3N_4 layer [104]. Next, the quantum well structure was etched with a CH_4 + H_2 mixture using the residual Si_3N_4 and Au strips as a RIE mask. The high-aspect ratio of the mesa and its height were accurately controlled by manipulating the etching parameters. Such control was important to ensure that the mesa sidewalls were close to vertical and the etching depth exceeded the depth of the quantum well.

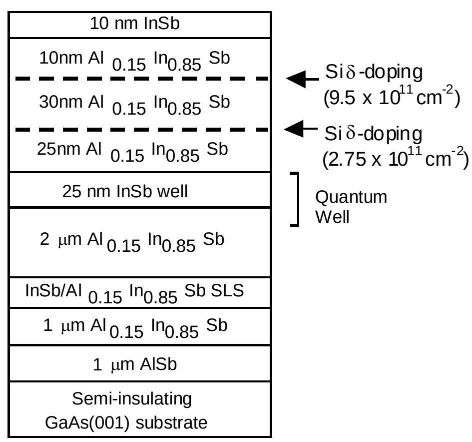

Figure 5.2: The quantum well structure used to prepare thin film, high mobility InSb. The active region of the structure is the 25 nm thick InSb well [Ref. 105].

Solin et al. [105] have recently attempted to minimize leakage current through the floor of the mesa by first preparing an insulating Al_2O_3 barrier and then oxidizing a layer of Al to within 50 nm of the mesa sidewall. The Au leads and shunt were deposited on Al_2O_3 barrier by two-angle shadow evaporation through a suspended Ge stencil mask [106]. The leads contacted the mesa sidewall, the $Al_{0.15}In_{0.85}Sb$ barrier/mesa floor (for a length of several μm) and the corresponding bonding pad lead. Besides the small feature size, extremely high alignment accuracy of about ±10 nm normal to the mesa sidewall is required for successful device fabrication.

Scanning electron micrographs of the four contact mesoscopic EMR read head structure are shown in Figure 5.3, Figure 5.4 and Figure 5.5. The structure for the device shown in these figures was derived from a bilinear conformal mapping of an internally shunted van der Pauw disk with an off center conducting inhomogenity [102]. Extensive studies of the magneto-transport properties of macroscopic EMR plate structures similar to that shown in Figure 5.3, Figure 5.4 and Figure 5.5 have facilitated the design of mesoscopic structure [102].

The 300 K magneto-transport properties of the mesoscopic EMR structure are shown in Figure 5.6. The corresponding low-field EMR is shown in the inset of that figure. The room temperature EMR reaches values as high as 35% at a signal field of 0.05 T. The raw areal density (not including shielding) of this device corresponding to the lateral dimensions of its sensing region is 595 $Gb/in.^2$ [105].

The room temperature mean free path of the carriers in the device is 200 nm. The transport is therefore, expected to be ballistic. As a result, expected EMR would be lower than what is observed in Figure 5.6. However, Solin et al. have suggested that the transport is still diffusive as a result of randomization of the carrier velocities due to scattering off the rough mesa sidewalls [107]. Given the assumption of diffusive transport, the EMR of the nanoscopic device is still lower than that obtained with a macroscopic vdP plate of the same geometry fabricated from thin film Te-doped InSb with a room temperature mobility of $4.5 \times 10^4\ cm^2/Vs$ [102]. The difference in mobility in the two structures may be one of the reason for the reduction in EMR value. The additional reduction derives from the residual current leakage through the mesa floor which results from unavoidable spillover of a portion of the Au leads beyond the Al_2O_3 insulating layers and on to the mesa floor [105].

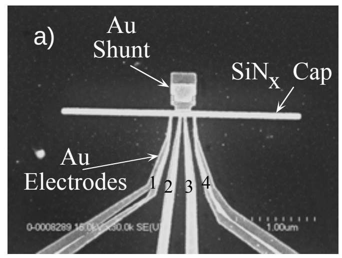

Figure 5.3: A top view low magnification SEM image of the EMR read-head etched into the quantum-well structure. The 4 Au electrodes have been deposited by the suspended mask technique.

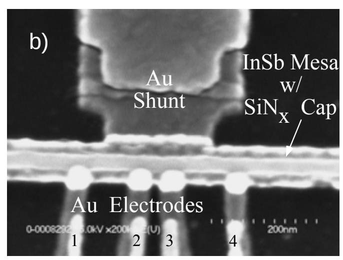

Figure 5.4: A top high resolution SEM image of the quantum-well mesa showing the SiNx cap.

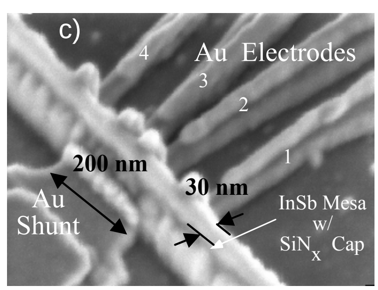

Figure 5.5: A SEM tilted view image (30^0 tilt angle) of the EMR read-head mesa. The height of the mesa is ~100 nm. The two layer composition of the shunt and electrodes results from the successive deposition used in the 2-angle shadow mask process.

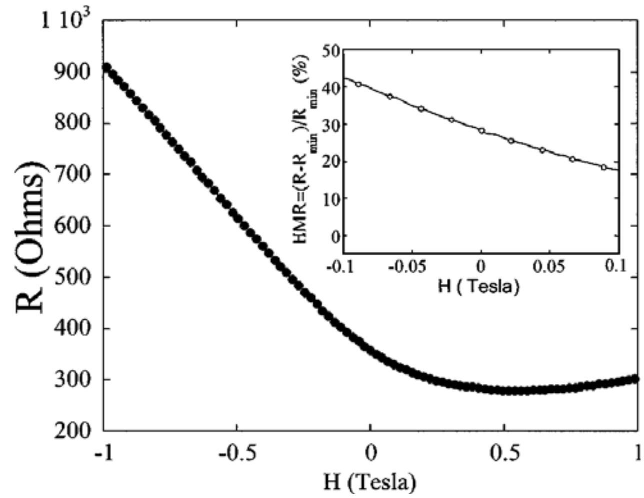

Figure 5.6: Field dependence of the resistance of the hybrid nanoscopic van der Pauw plate structure. (Inset) Extraordinary magnetoresistance [Ref. 105].

5.2.3 Advantages and Disadvantages of EMR Read-Heads

It is useful to compare the properties, in addition to MR, of EMR read-head sensors with conventional spin-valve (GMR) or spin tunneling (TMR) devices. Since EMR devices are non-magnetic, they do not suffer from demagnetizing effects [108]. Moreover, they are not mag-noise limited at ultra high recording densities as are conventional sensors [109]. This is a particularly important intrinsic advantage of EMR read-head sensors since mag-noise in GMR or TMR read-heads scales inversely with the volume of the free layer and is roughly equal to Johnson noise at an areal density of only 20 Gb/in^2 in GMR sensors [109, 110]. Asymmetric voltage lead placement not only provides optimal MR response but also renders the devices self-biasing. One of the most important potential advantages of EMR is response time which can be approximated by the inverse of the plasmon frequency, yielding a value in the sub-picosecond range [110]. This is significantly faster than the 10^{-9} - 10^{-10} *sec* switching times of metallic magnetic sensors that are limited by magnetization dynamics. Finally, through selective doping of the semiconductor, EMR sensors can in-principle be designed with a very low thermal coefficient of resistance without sacrificing other desirable performance features.

The most significant current disadvantage of EMR devices is that they represent a new and unproven technology. In addition, the EMR response is intrinsically nonlinear (e.g. quadratic) in field although a quasilinear response can be achieved. EMR devices require relatively low processing temperatures (< 300^0 C). Finally, the output voltages of EMR devices are somewhat lower than those of current conventional read-heads but this disadvantage may become less pronounced as the latter are fabricated in smaller sizes corresponding to areal densities of order 100 Gb/in^2.

5.3 Magneto-Optical Experiment

Due to the small m^* and large g-factor of electrons in InSb, far-infrared magneto-spectroscopy can be used to explore some aspects of electron spin in InSb quantum wells. The experiments described below were performed by collaborators using our InSb quantum wells.

5.3.1 InSb Quantum Well Structures

The samples studied in this work are InSb single quantum wells with widths of 20 to 30 nm, grown on GaAs (001) substrates [18]. The $Al_xIn_{1-x}Sb$ ($x = 0.09$ *and* 0.15) barrier layers are δ-doped with Si. The Si δ-layers are located either on one side of the quantum well (asymmetric samples) or equidistant on both sides of the quantum well (symmetric samples). The δ-doped layers within the barrier layers are typically located 70 nm from the well center. We expect the shape and symmetry of the wells to be determined only by the well/barrier mismatch (symmetric in all samples) and the mismatch in doping layers. The electron concentrations in the wells are in the range *(1-4)* x 10^{11} cm^{-2}, where only the ground-state subband is occupied. The mobility of the samples studied range from *70,000* cm^2/Vs to *130,000* cm^2/Vs. The energy-gap discontinuity [111] as well as the band offsets [112] in this strained-layer system has been determined earlier.

5.3.2 Experimental

The magneto-transmission experiments in this work were performed using two measurement systems. The SRCR measurements were carried out at the National High Magnetic Field Laboratory by X.H. Zhang, R.C. Meyer, T. Kasturiarachchi and Y.J. Wang. They used a Fourier Transform Infrared Spectrometer (100 to 700 cm^{-1}) and a superconducting magnet with magnetic field up to $B = 17.5$ T. Far infrared (FIR) radiation was emitted and detected by a glowbar and a Si bolometer, respectively. The sample normal was tilted at small angles (0^0 to 4^0) with respect to B. The propagation direction of the incident FIR radiation is the same as the direction of B. The ESR measurements were carried out by G.A. Khodaparast using a gas laser with wavelengths of 47 to 458 μm and B up to 7 T. The sample was tilted between 30^0 and 50^0. The laser beam was chopped mechanically at 150 Hz and a Ge:Ga photoconductor was used to detect the transmission signal. The sample temperature was 4.2 K in both measurement systems.

In addition to observing ESR through transmission measurements, we observed ESR through a change in the photoconductivity due to resonant absorption of the laser light. In this case, the sample itself functioned as a detector. An AC current of 1 μA (~130 Hz) is applied to the sample while the incident laser light is chopped at a frequency that is sufficiently small to ensure an adequate response time (~13 Hz). Features in the photoconductivity can be attributed to both non-resonant phenomena or to resonant mechanisms such as CR and ESR. As in the case of InSb inversion layers [113], the ESR signal is strongest when the sample is tilted. We have been unable to observe the ESR signal with no tilt. Detailed experimental [114, 115] and theoretical studies [116] on bulk InSb demonstrated the effect of magnetic field orientations on the *g*-factor anisotropy and magneto-optical selections rules in n-type zinc-blende semiconductors.

In our experiment, the tilt angle is varied to extend the range of *B* where ESR is observable for a given electron density. In this case, the spins (and ESR) respond to the total *B* but the two-dimensional Landau quantization (and thus the Shubnikov-de Haas oscillations and CR) depends only on the component of *B* along the sample normal.

5.3.3 Spin Resolved Cyclotron Resonance

SRCR first was observed in InAs quantum wells with AlSb barrier layers [117, 118]. The experimental observations were explained by using a modified Pidgeon and Brown bulk band structure model [119] that takes into account the non-parabolicity. In the modified model, the bulk energy gap is replaced by an effective energy gap in the 2D band structure equal to the energy spacing between the ground state valence- and conduction-subbands.

Figure 5.7 shows the calculated Landau level energies for a 25 nm-wide InSb quantum well with $Al_{0.12}In_{0.88}Sb$ barriers at zero tilt: $E_{mn} = E_m + (n+1/2)\hbar\omega_c \pm g\mu_B B/2$ where E_m is the subband energy *(m = 0,1), n=0,1,2,..* is the Landau level index, and μ_B is the Bohr magneton. The calculated Fermi energy is shown for an electron density of $n_s = 4.3 \times 10^{11}\ cm^{-2}$. In general, three spin-conserving transitions with $\Delta n = 1$ are possible at a given B, except for Landau level filling factors of $1 < \nu < 2$ where only two transitions are possible and $\nu < 1$ where only one transition is possible. The non-parabolicity of the conduction band makes the energies different for each transition at a given B.

Figure 5.8 is an example of SRCR. A normalized transmission spectra for sample S842 ($n_s \sim 4.3 \times 10^{11}\ cm^{-2}$) is shown at 13.25 T and a tilt angle of 0^0. The arrows indicate the SRCR features that correspond to the transition marked by arrows in Figure 5.7. The energies of these and other SRCR features (not shown) are well explained by the calculated fan diagram shown in Figure 5.7. The Landau level fan diagram also shows that Landau levels with the same and opposite spin intersect at several values of B. Four of those intersections are marked by circles in Figure 5.7. Subband Landau-level coupling in a two-dimensional electron gas (2DEG) was first observed in cyclotron resonance experiments performed twenty years ago [120]. The coupling causes an avoided level crossing between an excited state subband Landau level with index n and the ground state subband Landau level with index $n+1$. This was observed as a splitting in the cyclotron transition from level n to level $n+1$ in the ground state subband.

Electron spin effects were difficult to resolve since the experiments were made in a GaAs-based 2DEG. Spin splitting of the cyclotron resonance is small in GaAs due to weak band non-parabolicity and a small g-factor. In contrast, spin effects are evident in an InSb-based 2DEG due to a much larger g-factor (-51), stronger spin-orbit coupling, and strong band non-parabolicity. These characteristics allow us to study avoided level crossings for both the spin-up and spin-down cyclotron transitions. We observe the excited state subband Landau level with index n, spin-up, anticrossing with the ground state subband Landau level with index $n+1$, spin-up, as well as the corresponding spin-down anticrossing.

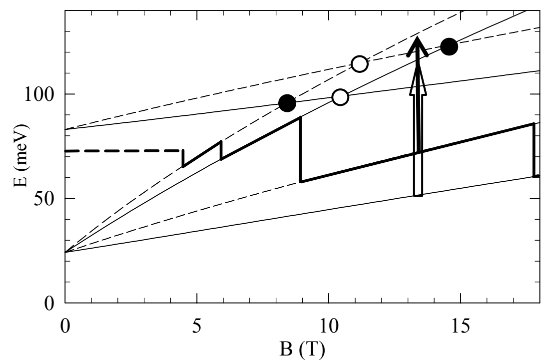

Figure 5.7: Landau level fan diagram showing spin up (down) energies for two subbands are shown by solid (dashed) lines. The Fermi level is indicated by the bold line. Crossings between Landau levels of opposite (same) spin are shown by solid (open) circles. The spin-conserving cyclotron resonance transitions that probe these crossings are shown by arrows.

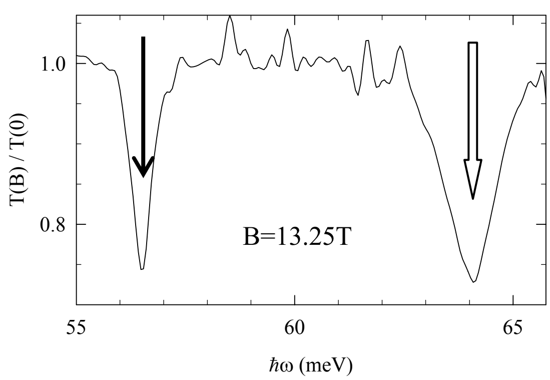

Figure 5.8: Measured cyclotron resonance energies as functions of applied magnetic field. The data points correspond to the transitions indicated by arrows in Figure 5.7. Splittings are observed at the four crossings labeled in Figure 5.7.

These two "same spin" anticrossings are analogous to those observed in GaAs. Surprisingly, we also observe anticrossings of states with opposite spin. The behavior of these "spin-flip" avoided level crossings as the magnetic field B is rotated away from the sample normal suggests that they are mediated by a spin-spin interaction. However, neither the Dresselhaus (crystal asymmetry) nor Rashba (structural asymmetry) interactions predict the observed anticrossings, according to first order perturbation theory [121]. Understanding spin-spin interactions may contribute to the ability to manipulate spins and to the identification of spin relaxation mechanisms.

5.3.4 Electron Spin Resonance

An asymmetry in the confinement potential for 2DES, has been predicted by Rashba and co-workers [122], to lead to a lifting of the spin degeneracy even in the absence of an applied magnetic field *B*. Most of the experimental evidences for Rashba spin splitting have been concluded from the beating of Shubnikov-de Haas (SdH) oscillations [123] and has been used to obtain a measure of the Rashba parameter, characterizing the strength of the $B = 0$ spin splitting. In GaAs quantum wells, zero-field spin splitting has also been inferred from Raman-scattering spectra [124]. We reported spin resonance spectroscopy in 20 nm-wide InSb quantum wells with $Al_{0.09}In_{0.91}Sb$ barrier layers, which confirm our earlier observations in 30 nm-wide wells [16].

Figure 5.9 shows the observed ESR for an asymmetric sample at low *B*. The resonance is very narrow, on the order of 40 mT. In this work, by using samples with different electron densities, wedges with different tilt, and six laser lines producing a sufficient signal to noise ratio, we are able to follow the ESR over a range of magnetic field and Landau-level index. We determine the Landau-level index for a given spin resonance from the filling factor of the Shubnikov-de Haas oscillation at the (total) *B* value at which the resonance occurs. The observed spin splittings for the samples is plotted in Figure 5.10. Also plotted in Figure 5.10 is the spin splitting $\Delta_s(B)$ expected in the absence of Rashba splitting from the modified (Pidgeon and Brown) bulk band structure which takes into account the non-parabolicity of the InSb band structure. This effective energy gap depends on well width, as does the momentum matrix element that we use as the lone fitting parameter (within its accepted range of values [125]). All the other band parameters are fixed at their accepted values. We conclude that our symmetric samples behave as expected for wells with no zero-field spin splitting based on one-electron energy levels. We find also that the CR positions in both symmetric and asymmetric wells are correctly predicted by the Pidgeon-Brown model. Similar results have been reported for GaAs quantum wells [126, 127].

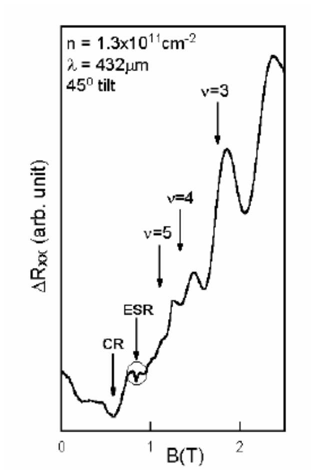

Figure 5.9: Change in resistance of sample S356 due to illumination by far infrared radiation. Non-resonant features are seen near integer Landau level filling factors ν. Resonant absorption features due to cyclotron resonance and electron spin resonance are marked.

The asymmetric samples show quite different behavior, especially at low *B*, as can be seen in Figure 5.10. The spin splitting is observed to deviate from those values expected for a symmetric well to values even beyond those calculated using the band-edge *g*-factor of -48. For the asymmetric samples the spin splitting is determined by the applied field (the

Zeeman term) plus an effective field from the Rashba splitting. We estimate a Rashba contribution of ~ 3 meV by taking the difference between the measured $\Delta_s(B)$ in a given sample and the $\Delta_s(B)$ value predicted for a symmetric sample at the same *n* by the Pidgeon-Brown calculation. For the electron densities used in this study ($1.1\text{-}2.2 \times 10^{11}\ cm^{-2}$), this corresponds to α value ~ $1.4 \times 10^{9}\ eVcm$ for the Rashba parameter. This value is comparable to the values determined in gated InAs quantum wells [128], even though the electric field in our un-gated asymmetric samples is much smaller.

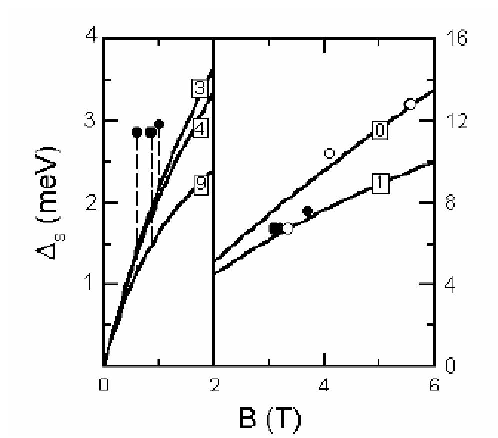

Figure 5.10: Measured (symbols) and calculated (solid lines) spin splittings as functions of magnetic field. Filled (open) circles represent asymmetric (symmetric) structures. The calculation includes only the Zeeman effect. The Landau level indices for the calculated splittings are labeled.

The ability to probe Rashba splitting with spin resonance suggests interesting future work. We are extending our spin resonance studies to gated samples. These should give us the ability to study the spin resonance in the absence of any applied magnetic field. We also plan to study samples in which the asymmetry is due to differing Al concentrations in the barriers on either side of the quantum well rather than to asymmetric doping as in the present samples. This, together with the ability to vary the electron density, should allow us to distinguish the effect of an asymmetric electric field from the role of the barrier asymmetry [100, 129] in causing the spin-orbit splitting. In the results we have presented here, both mechanisms may contribute.

Chapter 6
GROWTH OF InSb ON GaAs (111) SUBSTRATES

6.1 Introduction

Due to the ~14.6% lattice mismatch between InSb and GaAs, it is very difficult to grow a high quality thin film of InSb on a GaAs substrate. The lattice mismatch results in misfit strain and dislocations. The growth of InSb on a GaAs (001) substrate begins in the Volmer-Weber Mode, Sec. 2.1. Instead of a wetting layer, 3D islands are formed as the growth of InSb initiates. On the other hand, growth in the {111} orientation has been reported to prevent 3D island growth and better confined dislocations to the heterointerface [130, 131]. It has also been reported that the electrical properties of InAs layers grown on GaAs substrates are improved by growth on higher index substrates [132]. For the substrate orientation of {111}, a maximum piezoelectric field is obtained along the growth axis [133]. Devices with strong piezoelectrically generated electric fields for applications in optoelectronic can be developed on (111) substrates [133, 134]. Quantum wells grown on (111) surfaces are expected to have enhanced optical transition and a laser based on this has exhibited a low threshold voltage [135].

On a GaAs (111) wafer, one side is (111)A and the reverse side is (111)B. On GaAs(111)A the surface As and Ga atoms are back bonded to bulk GaAs by one and three bonds, respectively. On the other hand, in GaAs (111)B case, the Ga and As are bonded to the bulk by one and three back-bonds, respectively. The growth on (111)A substrates has been shown to be very sensitive to growth parameters [136]. It has also been shown that the growth on (111)B substrate compared to that on (001) substrate is critical but less sensitive to growth parameters compared to the growth on (111)A surface [137]. Homoepitaxial growth of GaAs (111)A shows only one surface reconstruction (2x2) at any sample temperature [138]. The sticking coefficient of extra As on this surface is very low during the growth. On the other hand for GaAs (111)B, four surface reconstructions are known to exist. As the substrate temperature is increased these reconstructions are (2x2) [139], $(1x1)_{LT}$ [140], $(\sqrt{19}x\sqrt{19})$ [139] and $(1x1)_{HT}$ [141]. (2x2) is an As-rich, $(\sqrt{19}x\sqrt{19})$ is Ga stabilized and $(1x1)_{HT}$ is Ga rich surface reconstruction. It has been shown that the As-stabilized GaAs (111)B (2x2) reconstruction has As trimers bonded to the underlying As plane [142]. The As-stabilized reconstruction (2x2) of GaAs (111)A has been theoretically predicted to have As-trimer bonded to underlying Ga plane [143].

It was recently reported that the initial growth of InSb is two-dimensional on GaAs(111)A substrates, but three dimensional on GaAs (001) substrates [144]. Because interface roughness at the substrate interface may affect the mobility of electrons in quantum wells, GaAs(111)A substrates are potentially the better choice for growth of InSb/AlInSb heterostructures. Si-doped GaAs grown on (111)A substrates produces p-type material while n-type material results on (111)B substrates [145]. Si bonds to the surface Ga atoms taking up sites in the As sublattice on a GaAs (111)A surface.

Since a high doping efficiency is required for many types of structures, we have performed a few preliminary experiments to check the doping efficiency of Si in InSb epilayers grown on GaAs (111)A substrates [146]. In these experiments at OU, Si-doped

InSb was grown on both orientations of GaAs (111) substrates and Hall measurements (298 to 7 K) were performed on the samples. This preliminary data is compared to the Si doped InSb grown on GaAs (001) substrates.

6.2 Experimental

Two substrates, GaAs (111) and GaAs(001), were mounted side by side using Indium on a moly-block. The GaAs (001) substrate was mounted to monitor the substrate temperature based on the oxide desorption temperature (T_{OD}). The oxide desorption on GaAs(111) substrates typically occurred at substrate temperatures ~35 ^{0}C below $T_{O.D}$. First the oxide layer is desorbed from both substrates. The temperature of the substrates is increased to 20 ^{0}C above the oxide desorption temperature of the GaAs (001) substrate. The substrates are annealed at this temperature for nearly 20 m. The GaAs layer is then grown at a rate of 0.55 ML/s for 10 to 12 m with the Ga:As growth rate at 1:2.14 and a substrate temperature of T_{OD} - 40 ^{0}C. If facets appeared during the growth, the substrate temperature was reduced by 20 ^{0}C and growth was resumed.

After growth of the GaAs layer, the substrate is decreased to nearly T_{OD} – 300 ^{0}C. The As shutter is kept open while the temperature of As cell is ramped down to 130 ^{0}C. After the substrate temperature reaches the new substrate set point, the As shutter is closed and the Sb shutter is opened. The InSb growth is started at a rate of 0.8 ML/s with the growth rate ratio of In:Sb at 1:1.12. When the In shutter is opened, the RHEED shows spots for the (001) substrate, whereas the (111) substrates have a streaked pattern. After 12 s of growth, while keeping In shutter open, the substrate temperature is increased to nearly 60 ^{0}C above the set point (at the rate of 0.5 ^{0}C/s). When the new substrate temperature is reached, growth is paused. Sample grown on the (001) orientation shows a c(4x4) or '1x3' reconstruction whereas growth on a (111) substrate exhibits a (2x2) pattern. This indicates that the growth of InSb on (001) GaAs initiates by 3D growth followed by 2D growth as observed by in-situ RHEED. In contrast, two dimensional growth of InSb on (111) GaAs is observed by RHEED from the onset. For the InSb/GaAs (001) sample, the surface reconstruction transition temperature (T_{tr}) from '1x3' to c(4x4) is recorded.

Further growth of InSb on both the substrates is carried out at T_{tr}. During the growth, the sample on a (001) substrate shows a '1x3' reconstruction whereas the (111)A sample shows a (2x2) pattern. In between the growth, the T_{tr} is re-recorded and the growth is resumed at the new T_{tr}. A total thickness of 2 μm of InSb layer is grown. T_{tr} (~390 ^{0}C) is re-recorded after the growth finishes.

The substrate temperature was then varied from T_{tr}-40 ^{0}C to T_{tr}+40 ^{0}C (in intervals of 20 ^{0}C) in five sets of such samples grown on GaAs (111)A substrates. One sample was grown at T_{tr}-40 ^{0}C on a GaAs (111)B substrate. The samples were delta doped with Si (~100 s) in an Sb flux. Finally, the samples are capped with a 0.31 μm thick layer of InSb. Samples for this experiment are listed in Appendix 2.

6.3 Results

Hall measurements were performed on Si-δ-InSb/GaAs (111)A and Si-δ-InSb/GaAs (111)B samples. The results of mobility and density at 77 K as function of Si-doping temperature are given in Figure 6.1. The Si-δ-InSb/GaAs (111)A sample is n-type when Si doping is at T_{tr} or below whereas the doping efficiency is p-type at growth temperatures greater than T_{tr}. For comparison, the Si-δ-InSb/GaAs (001) samples are n-type at all growth temperatures. The mobility and density increased as the growth temperature was decreased below T_{tr}. At growth temperatures below ~380 ^{0}C, the doping efficiency is highest. The resulting layers have electron densities that are ~70% of the densities in layers grown on GaAs(001) substrates under similar conditions. Above ~380 ^{0}C, the doping efficiency is much lower. The Si-δ-InSb/GaAs (111)B sample is n-type when Si is doped at T_{tr} – 40 ^{0}C. The doping efficiency is better than in the simultaneously grown Si-δ-InSb/GaAs (001) sample but the mobility is far lower. The surface of the sample on (111)B substrate looked cloudy, implying a deficiency of Sb on the surface. Since this was a preliminary sample, further growth optimization is required before the mobilities can be compared in the two samples.

The room temperature results for mobility and density are given in Figure 6.2. The doping efficiency for the sample grown on GaAs(111)B is higher than that grown on GaAs(001) substrate or GaAs(111)A at T_{tr}-40 ^{0}C. The doping efficiency and mobility on both GaAs (001) substrates at this temperature are comparable. The doping efficiency for samples grown on GaAs (111)A is higher than those grown on GaAs(001) substrates for growth temperatures less than the T_{tr}, reaching a maximum at T_{tr}-20 ^{0}C. However, the mobility is lower comparatively at all growth temperatures.

The surface of the sample on (111)B orientation after the growth looked Sb deficient. This may be responsible for low mobility in that sample. Since these are a few preliminary results, the growth conditions need to be optimized for higher mobilities on GaAs (111) substrates. Moreover, the experiments on the GaAs (111)B substrate need to be extended to other growth temperatures too.

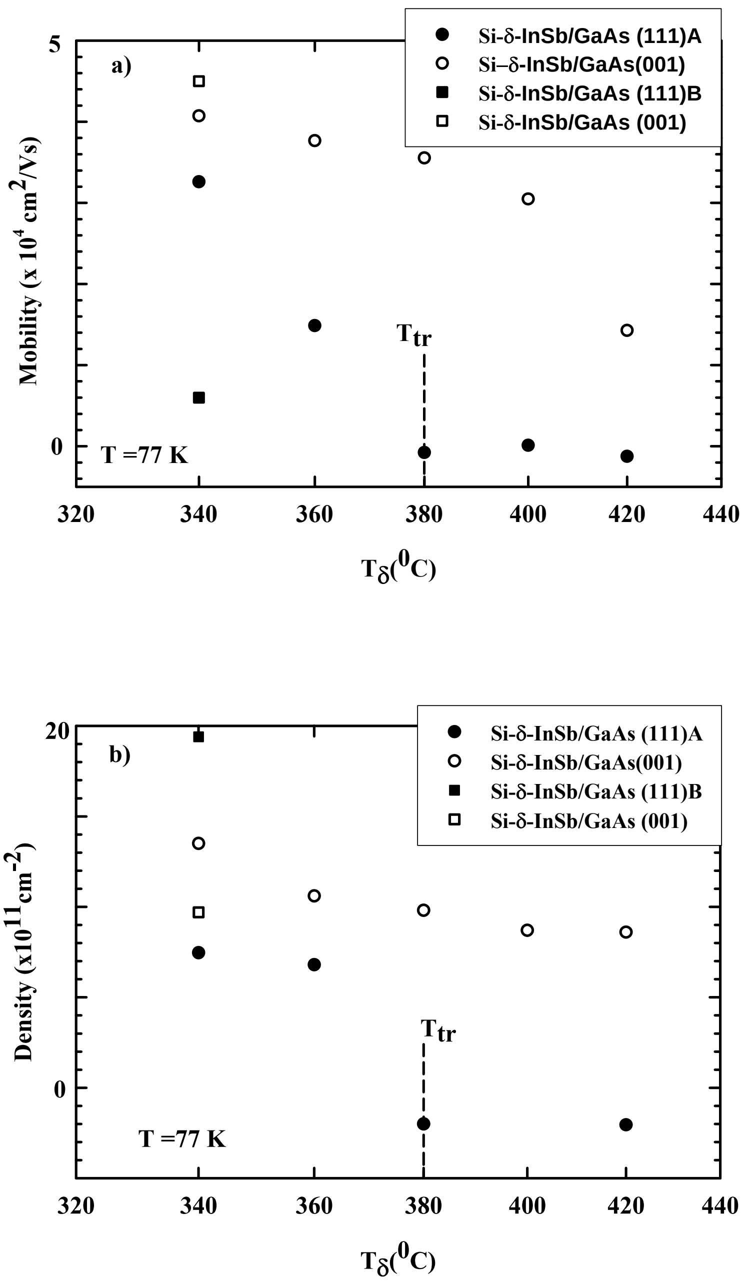

Figure 6.1: Mobility and density at 77 K as functions of sample temperature during doping for Si-doped InSb grown on GaAs substrates. The results are compared for the simultaneously grown (111)A (filled circle) and (001) samples (open circle). The comparison for simultaneously grown sample on (111)B (filled square) and (001) (open square) is also shown. T_{tr} is the temperature of transition of RHEED pattern from '1x3' to c(4x4) in sample grown on GaAs(001) substrates. T_{δ} is the sample temperature during delta doping. The p-type conduction is observed for samples grown on (111)A substrates doped at and below substrate temperature T_{tr}.

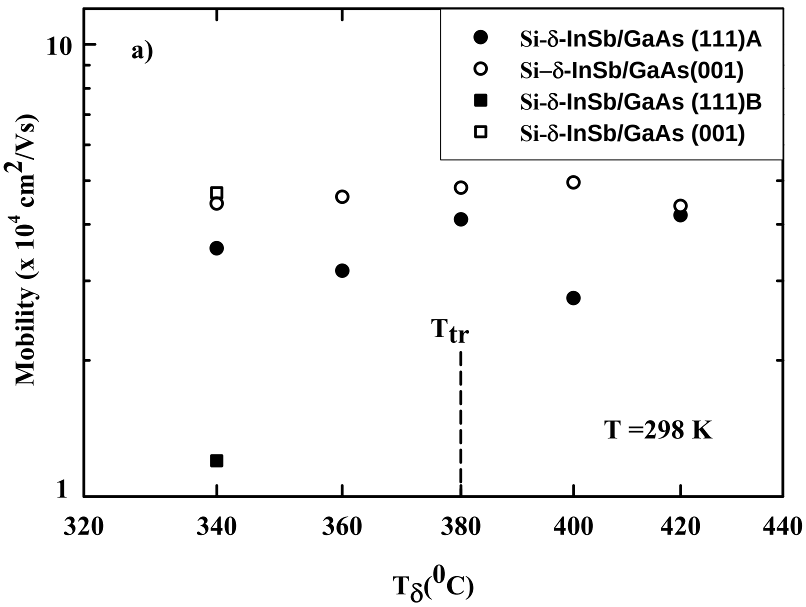

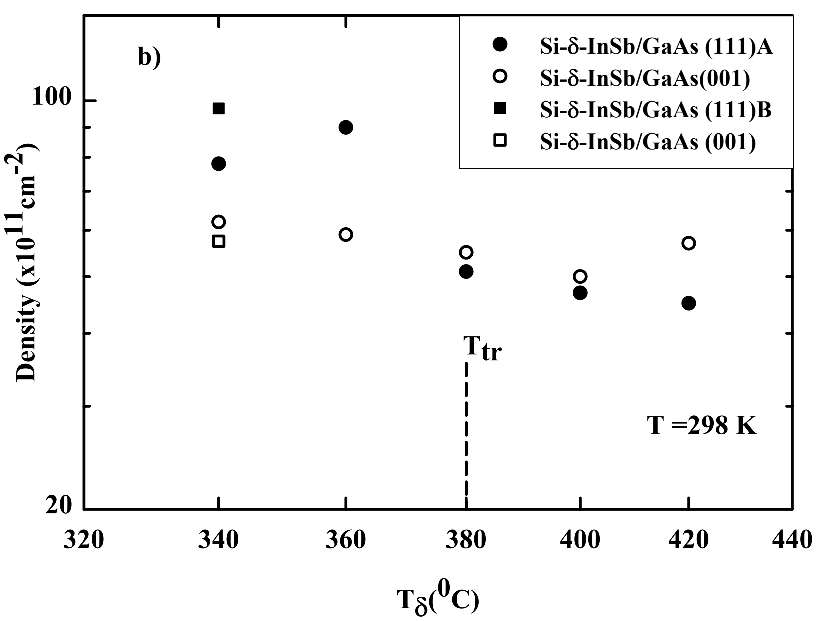

Figure 6.2: Mobility and density at 298 K as functions of sample temperature during doping for Si-doped InSb grown on GaAs substrates. The results are compared for the simultaneously grown (111)A (filled circle) and (001) samples (open circle). The comparison for simultaneously grown sample on (111)B (filled square) and (001) (open square) is also shown.

6.4 AFM Observations

Ex-situ planar AFM measurements were performed on InSb grown on GaAs (001) and (111)A substrates [147]. These observations reveal shallow hillocks and abrupt steps associated with threading dislocations and stacking faults in (001) substrates. The samples grown on (111) oriented substrates do not show same shallow hillocks but stacking faults can be seen. These stacking faults mainly initiate at the interface of GaAs and InSb. The density of threading dislocations in (111)A oriented substrate is very low. Figure 6.3 shows the AFM images of the surface on the samples with (001) and (111)A oriented substrates respectively.

The triangular/pyramidal features seen in Figure 6.3 (b) are the stacking faults. The density of threading dislocation in sample with (001) oriented substrate was seen to be nearly $1.2 \times 10^{7}\ cm^{-2}$ whereas in the one grown on (111) oriented substrate was less than $6 \times 10^{6}\ cm^{-2}$. The stacking fault density in the sample with higher index oriented substrate was nearly $10^{7}\ cm^{-2}$. A decrease in threading dislocation density is seen in the samples grown on higher index substrates. But defects like stacking faults are still present. These stacking faults can compromise electron mobility in these structures and hence need to be minimized by optimization of the growth conditions.

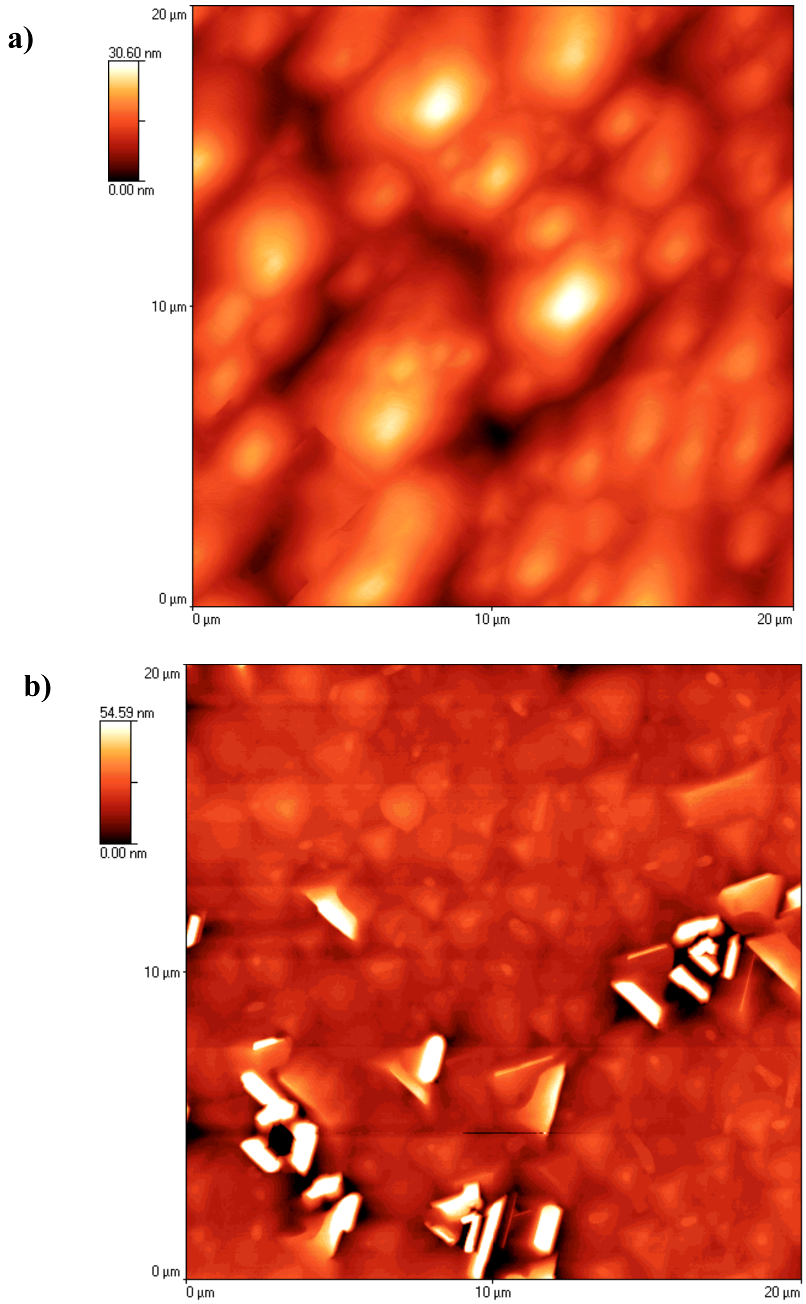

Figure 6.3: AFM images of 20 x 20 μm^2 wide area of surface of InSb grown on GaAs a) (001) and b) (111)A substrates respectively.

Chapter 7
CONCLUSIONS AND RECOMMENDATIONS FOR FUTURE WORK

This thesis work reports the first observations of ballistic transport in InSb-based mesoscopic structures, which were enabled by the high electron mobility and density of the underlying quantum wells. The results of these and other experiments are summarized here, along with suggestions for future work. Because of the unique qualities of InSb, like a small effective mass, high room temperature mobility and large *g*-factor, this material system is an attractive candidate for realization of magnetic sensors, spin FETs and other novel devices.

7.1 InSb Quantum Wells

In this thesis work, low temperature mobility of $200{,}000\ cm^2/Vs$ in InSb / $Al_xIn_{1-x}Sb$ single quantum wells have been obtained. Single subband densities as high as $4.3 \times 10^{11}\ cm^{-2}$ at 4.2 K were achieved. The quantum wells have been successfully realized with AlInSb barriers where the maximum Al concentration in the alloy is 15%.

Quantum wells with little or no parallel conduction at room temperature may have been realized in s945 and s946. Average room temperature mobility of $36{,}000\ cm^2/Vs$ has been observed. Although to confirm the presence of parallel conduction, further QMSA analysis at higher temperatures is necessary. Since the anisotropic behavior in room temperature resistivity was observed in a van der Pauw piece of a sample with higher Al concentration in $Al_xIn_{1-x}Sb$ interlayer, it would make sense to fabricate Hall bars such that channel is aligned along [110], $[\bar{1}10]$ and [001]. The results obtained on square pieces can therefore be confirmed. Moreover, QMSA analysis using the resistivity data of these directional Hall bars will help in estimating the parallel conduction in respective directions. The results at room temperature should indicate the best direction for the channel from the point of view of reduced parallel conduction and higher mobility.

The ohmic contacts to the quantum well samples were made using Indium, AuGeNi or In-Sn alloy. The van der Pauw samples had In or In-Sn alloy contacts. The Hall bars and mesoscopic devices fabricated on structures with 9% Al concentration in the alloy layer and with higher Al concentration (> 9%), had evaporated In and AuGeNi contacts respectively. It was easier to wire bond to 3000 Å thick contact metal than to a 1000 Å thick layer. Further experiments may include optimizing the thickness of the evaporated contact, annealing conditions and experimenting with the evaporated In-Sn alloy.

TEM measurements on these samples will give us insight into the defect density.

7.2 Bend Resistance Measurements

Classical ballistic phenomenon like negative bend resistance and quenching and suppression of the Hall effect were observed in InSb based four terminal structures at 1.5 K. The NBR peak amplitude persists up to 200 K for $x = 0.15$ and up to 185 K for $x = 0.09$.

At still higher temperature, the diffusive component to the transport dominates over ballistic part. The increasing contribution to the transport by the parallel low mobility conducting layers at high temperature can decrease the average mean free path of carriers through these devices. The intrinsic carriers in the $Al_xIn_{1-x}Sb$ layer and the carriers in the delta doped alloy layer at high temperature can be possible sources of parallel conduction. Using QMSA conduction through the intended active channel and the unintentional parallel channel are estimated. The conduction through the InSb quantum well at low temperature agreed with the results obtained from the Hall effect.

The density of carriers was measured through and not through the constriction of the same four-terminal device. The density through the constriction was always lower, which may indicate effects of etching on the sample.

The negative bend resistance amplitude as a function of device width, temperature and magnetic field can be estimated theoretically by the Landauer-Büttiker formula. Comparison with experimental values can provide us with information on depletion spreading and the ballistic mean free path. In the future, working devices can be fabricated with these known considerations.

Improvements to the underlying quantum wells could result in better four terminal devices. Quantum well samples with higher Al concentration in the alloy layer may reduce the intrinsic carriers in the alloy at high temperature. Moreover, the density of electrons in the quantum well is expected to be higher, increasing the electron mean free path. Higher mobility at lower and higher temperature will increase the mean free path in these devices. Reduction of parallel conduction at higher temperature may facilitate the observation of ballistic transport up to room temperature.

7.3 Point Contact Measurements

Quantized conductance is observed for the first time in InSb based in-plane gate devices. A maximum of five plateaus was seen in all the devices under study. Although it is difficult to get an accurate value for the series resistance, guessing a value of 3.4 kΩ in a device gives the conductance quantization in units of $2e^2/h$ at 0 T. This indicates the levels are possibly spin-degenerate and each subband contributes $2e^2/h$ to the conduction. Subtracting a series resistance of 1.6 kΩ, on the other hand, indicates spin splitting at zero magnetic field and a contribution of e^2/h from each spin split level.

As the magnetic field is increased in the perpendicular direction, depopulation of subbands occurs. The quality and flatness of plateaus improve due to the reduction of backscattering. Zeeman splitting is seen around 0.9 T which is much less than for InAs-based (~ 2.5 T) or GaAs-based (~ 6 T) QPCs. This is favorable as it suggests that lower B-fields are required to observe interesting spin-related features in InSb. At higher perpendicular magnetic field, a repopulation effect was observed in one device, which could be due to the large *g*-factor of InSb. This effect has not been reported in any material system.

When the magnetic field is applied parallel to the plane of the quantum well and to the direction of the current, Zeeman splitting occurs. As the magnetic field is further increased, crossing of subband levels is observed in one device. Assuming the bulk *g*-factor, the crossing around 3 T suggests subband spacing of nearly ~10 meV at 0 T. Similar experiments on more than one such device can confirm these observations. A few groups working on GaAs, InGaAs etc. have observed an enhancement in the 1D *g*-factor compared to the *g*-factor of the bulk sample. In order to estimate the g-factor, these groups employed a technique discussed in Sec. 4.2.4. Knowledge of this 1D value for our system may help us in explaining the repopulation effect and in estimating the subband spacing.

The 0.7 anomaly was not observed in any of these devices. This could be due to the onset of gate leakage. The quantization was observed to persist up to 11 K. Although it should be mentioned that the temperature dependence data was taken after the device had already been through various cooling cycles. The quantization may actually persist to higher temperature for an optimized good working device.

The preliminary data on quantum point contacts as seen in this thesis work are promising. The quality of the quantization was seen to deteriorate and the gate leakage increased with each cooling cycle. This made it hard to carry out all the required experiments with one device. Also, the yield of good devices was poor. The repopulation effect was observed in only one device. In the future, the gate leakage through the device should be reduced. This may require the optimization of the layer structure. Also if possible, major experiments on a good working device should be performed entirely during the first cooling cycle. Repeating experiments at 0 T on a better device may help in estimating the series resistance more precisely.

Two different voltages can be applied on the two gates. While sweeping gate voltages, this difference can be maintained throughout the measurements. Any inhomogenity or trapped charge in the channel at a certain location can therefore be avoided.

7.4 Collaborators' Experiments

Mesoscopic magnetoresistors based on our InSb quantum well samples have been successfully realized by our collaborators. These samples have also been successfully used for magneto-optical, quantum Hall ferromagnetism and other ballistic transport experiments by various collaborators. Already an improvement in the mobility has been seen in InSb quantum well structures, Sec. 2.7. Although with further optimization of the layer structure, which includes but is not limited to varying the layer thicknesses and the delta doping density, a further increase in the mobility is plausible. One then expects a corresponding improvement in the many experiments that utilize InSb quantum wells.

Appendix 1

HALL COEFFICIENT AND MAGNETORESISTANCE

Magnetoresistance is given as

$$\rho = \begin{pmatrix} \rho & R_H \\ R_H & \rho \end{pmatrix} \tag{A1.1}$$

For the two carriers, magnetoresistance and Hall coefficient using Eq. (1.7)

$$\rho = \frac{1}{\frac{1}{\rho_1} + \frac{1}{\rho_2}} \tag{A1.2}$$

$$\frac{1}{\rho_1} = \frac{\text{Adj } \rho_1}{|\rho_1|} \tag{A1.3}$$

Solving for ρ and R_H gives

$$\rho = \frac{\rho_1 \rho_2 (\rho_1 + \rho_2) + (\rho_1 R_{H2}^2 + \rho_2 R_{H1}^2) B^2}{(\rho_1 + \rho_2)^2 + (R_{H1} + R_{H2})^2 B^2} \tag{A1.4}$$

$$R_H = \frac{R_{H1}\rho_2^2 + \rho_1^2 R_{H2} + R_{H1} R_{H2} (R_{H1} + R_{H2}) B^2}{(\rho_1 + \rho_2)^2 + (R_{H1} + R_{H2})^2 B^2} \tag{A1.5}$$

Case 1: In case of low magnetic field i.e. $B \ll 1/\mu_1$ for $n_2 \gg n_1$ and $B \ll 1/\mu_2$ for $n_2 \ll n_1$

$$\rho \approx \frac{\rho_1 \rho_2}{(\rho_1 + \rho_2)} \tag{A1.6}$$

$$R_H \approx \frac{R_{H1}\rho_2^2 + \rho_1^2 R_{H2}}{(\rho_1 + \rho_2)^2} \tag{A1.7}$$

For two types of carriers, electrons and holes

$$\rho_1 = \frac{1}{n_1 e \mu_1} \tag{A1.8}$$

$$\rho_2 = \frac{1}{n_2 e \mu_2} \tag{A1.9}$$

$$R_{H1} = -\frac{1}{n_1 e} \tag{A1.10}$$

$$R_{H2} = \frac{1}{n_2 e} \tag{A1.11}$$

Therefore, Hall coefficient and magnetoresistance in the low magnetic field are

$$\rho = \frac{1}{e(n_1\mu_1 + n_2\mu_2)} \tag{A1.12}$$

$$R_H = \frac{n_2\mu_2^2 - n_1\mu_1^2}{e(n_1\mu_1 + n_2\mu_2)^2} \tag{A1.13}$$

Case 2: In the high magnetic field limit i.e. B » $1/\mu_1$ for n_2 » n_1 and B » $1/\mu_2$ for n_2 « n_1.

$$\rho = \frac{n_1\mu_2 + n_2\mu_1}{\mu_1\mu_2(n_2 - n_1)^2} \tag{A1.14}$$

$$R_H = \frac{1}{e(n_2 - n_1)} \tag{A1.15}$$

Appendix 2

SAMPLE LAYER STRUCTURE AND TRANSPORT PARAMETERS

Table A2.1: Single quantum wells (InSb / $Al_xIn_{1-x}Sb$).

d: Doping (S: symmetric, A: Asymmetric)
x: Al_x Concentration
w: well width
b: barrier width
sp: spacer layer thickness
c: cap layers thickness
d1: doping density near well
d2: doping density near surface
n: density
μ: mobility
Dp.: Depleted

	d[3]	x	w	b	sp	c	d1	d2	n 300 K	n 4.2 K	μ 300K	μ 4.2K
		%	nm				x 10^{11} cm^{-2}				x $10^4 cm^2/Vs$	
S696	S	9	30	60	100	20	1.5	20	7	1.9	2.4	12.4
S697	S	9	20	30	100	20	1.5	20	7	2.7	2.6	16.8
S702	S	9	20	30	100	20	1.5	9.5	5	2.4	2.9	18.6
S704	S	9	20	30	100	20	0.55	9.5	3	1.3	2.5	17.0
S705	S	9	20	15.7	40	20	1.85	9.5	6.6	3.3	2.8	6.8
S707	A	9	20	15.7	40	20	2.75	9.5	5.6	2.1	2.3	9.2
S708	S	15	20	27.5	28.2	20	3.6	12.2	10.7	1.6	2.2	17.1
S710	S	9	30	90	100	20	0.65	10.3	4.8	0.8	1.9	8.0
S715	A	9	20	15.7	40	20	2.75	9.5	5	2.1	2.3	10.5
S716	S	9	30	70	100	20	0.7	10.3		1.4		12.0
S718	A	15	20	27.5	28.2	20	3.6	12.2	2.8	2	2.0	4.0
S719	S	15	20	55.8	28.2	20	1.8	15		2.1		3.0
S760	S	15	25	25	30	20	2.8	15				
S761	S	15	25	25	30	20	2.8	15				
S768	S	9	30	60	100	20	1.5	10		1.7		8.5
S769	S	9	30	60	100	20	1.5	9		2		9.7

[3] If the delta-doped layer is on either side of the well then the structure is symmetric (S). If the delta layer is on one side of the well (towards surface side) then it is asymmetric (A). There is another delta doped layer near the surface.

	d	x	w	b	s	c	d1	d2	n 300 K	n 4.2 K	μ 300K	μ 4.2K
		%	**nm**				**$x10^{11}$ cm^{-2}**				**x 10^4 cm^2/Vs**	
S770	S	9	30	60	100	20	1.5	7.5	5.2	1.2	2	6.0
S777	S	15	20	25	20	20	2.8	15	6.7	3.6	1.3	2.2
S778	S	15	25	25	30	20	2.8	15	4	1.9	1.8	3.3
S780	A	15	20	27.5	28.2	20	3.6	15	4.9	1.7	1.5	3.7
S839	S	15	25	40	100	23	4.3	13.5	6.9	3.9	2.7	8
S842	S	15	25	40	100	23	4.3	12.5	7.2	4.1	2.7	8
S901	S	10.5	25	38	95	22.5	6.3	30	7	4	2	4.3
S902	S	10.5	25	38	95	22.5	6.3	35	5.7	4.4	2.5	5
S906	S	9	30	60	100	23	2	21	7.4	1.4	2.2	
S912	S		23	30	100	23	7.2	35	10	5.3	2.8	8.4
S927	S	12	25	50	100	23	4	11	Similar to S942			
S928	S	25	14	9	100	23	9	19	10	6.5	0.9	1.2
S936	S	12	25	39	97	22.7	5	11	9.7	4.1	2.7	20
S937	S	12	25	39	97	22.7	4	8	5.9	4	3.5	16
S938	S	12	36	10	97	22.7	5	11	14.4	3.9	1.3	
S939	S	15	11.5	29.5	100	2.3	4.5	14	10	4.4	1.8	9.6
S940	S	12	25	39	97	22.7	5	11	10	3.3 4	2.3	18 8
S941	S	15	18	43	100	23	3.5	14	5.2	3.5	2.9	12.4
S942	S	12	25	50	100	23	4	11	7.8	3.5	2.5	11.6 (12K)
S943	S	12	25	39	97	22.7	5	11	9.7	3.9	2.6	13.9 (12K)
S944	S	12	25	39	97	22.7	2	11	11.7	Dp.	1.89	Dp.
S945	S	12	25	39	97	22.7	4	4	5.7	3.5	3.4	9.3
S946	S	12	25	39	97	22.7	3	2	4.2	2.5	3.6	9
S951	S	15	18	43	100	23	3.5	17	4.9	2.3	2.9	7.8
S955	S	15	18	43	100	23	3.5	17	Similar to S951			
S956	S	15	18	43	100	23	3.5	17	Similar to S951			

For ballistic transport study: s697, s842

For EMR (read-head sensors) study: s715, s760, s761,

For magneto-optical study: s702, s704, s707, s716, s769, s842, s912, s928, s936, s938, s939, s941

For Hitachi's experiment: s927 (whole wafer), s956 (whole wafer)

For Ohio University's experiment: s769, s780, s912

Table A2.2: Multi-quantum well samples

	Doping	x %	w	b	Repeat
			nm		
S781	None	9	2.5 10 20	30 30 30	11 11 11
S784	None	9	5 10 15 25	30 30 30 30	11 11 11 11
S809	None	8	10	50	40
S810	None	12	10	50	40
S812	None	16	10	50	40
S813	None	20	10	50	40
S948	None	5	20	50	40
S949	None	8	20	50	40
S953	None	11	20	50	40
S954	None	14	20	50	40

Table A2.3: Bulk samples

	x	W_1 (alloy)	W_2 (InSb)	n at 300K	μ at 300K	Comments
	%	μm		x 10^{11} cm^{-2}	x 10^4 cm^2/Vs	
S785	9	4	-	4.6	1.05	AlInSb
S786	9	1	3	65.2	4.63	InSb/AlInSb
S789	15	4	-	1.75	0.35	AlInSb
S816	-	-	5	13	4.84	InSb

Table A2.4: For GaAs (111) experiment

Sample Type	T_{tr}–40 ^{0}C	T_{tr}–20 ^{0}C	T_{tr}	T_{tr}+20 ^{0}C	T_{tr}+40 ^{0}C
Si-δ-InSb/GaAs(111)A	S739	S738	S747	S740	S742
Si-δ-InSb/GaAs(001)	S736	S737	S746	S741	S743
Si-δ-InSb/GaAs(111)B	S751	-	-	-	-
Si-δ-InSb/GaAs(001)	S749	-	-	-	-

Additional samples (Al concentration in the alloy is 9%)

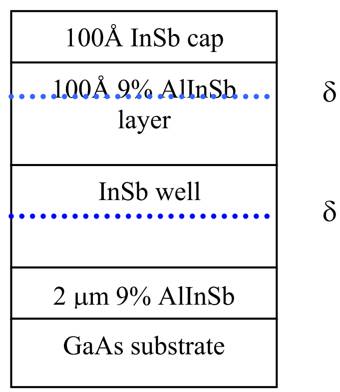

Fig. a: Center δ-doped

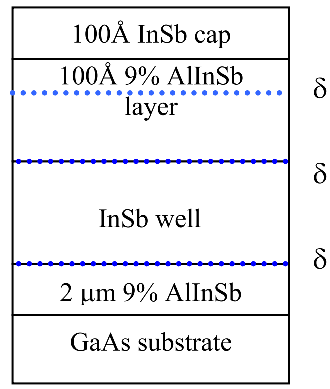

Fig. b

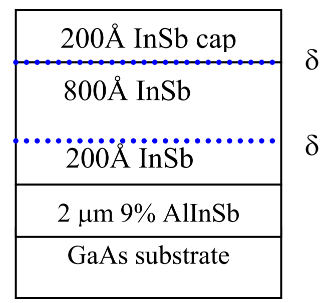

Fig. c

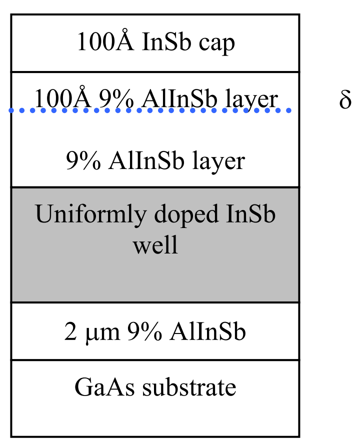

Fig. d

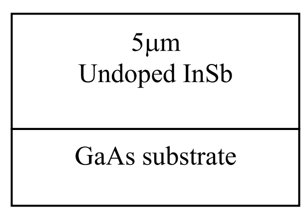

Fig. e: Undoped InSb

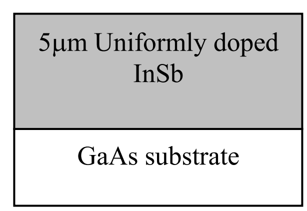

Fig. f: Si-δ-doped InSb

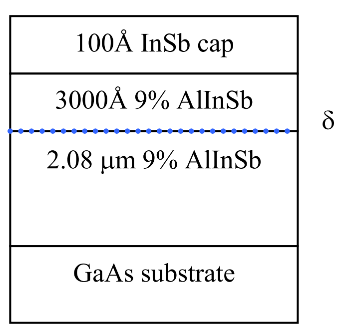

Fig. g: Uniformly doped AlInSb

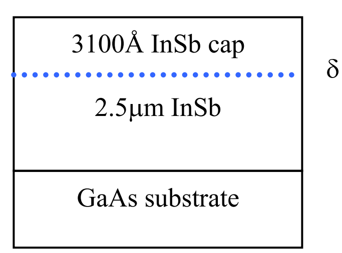

Fig. h: Si-δ-doped InSb

Layer structure i: 2-δ-InSb / 9%AlInSb / GaAs (not shown)

Table A2.5: Samples for room temperature mobility analysis

	Fig.	T_{δ}	T_{Si}	b	w	d1	d2	μ_{300K}	μ_{7K}	n_{300K}	n_{7K}
		^{0}C		nm		x $10^{11} cm^{-2}$		x $10^{4} cm^{2}/Vs$		x $10^{11} cm^{-2}$	
s814	a	Ttr-25	1120	100	30	20	20	1.6	1.5 not linear	22.9	14.8
s815	d	Ttr-25	1141	100	30	20	20	1.3	1.3 not linear	35.5	30.5
s816	e	Ttr+40				-	-	4.8	0.4 not linear	131	9.7
s817	a	Ttr-25	1184	100	30	20	20	1.8	1 not linear	9.2	9
s818	f	Ttr-25	1023		-			5.6	6.6 (10K)	142	71.7
s819	g	Ttr-20	1120		-		37	1	1.2 (10K)	30	22.5
s821	i	Ttr-25	1120	30	30	20 near sub.	6.6	1.2	1.07	2.36	1.9
s822	h	Ttr-25	1135	-	-			5.2	2.8	60.8	8.4
s823	a	Ttr-25	1120	-	30	10	20				

Appendix 3

LITHOGRAPHY OF InSb STRUCTURES

To define the first level of lithography to define Hall Bar

1. Clean in Isopropanol for 3 min twice, rinse, blow dry.
2. Bake at 120 ^{0}C for 5 min.
3. Spin on AZ-27 photoresist[4] at 500 rpm for 3 s and 4000 rpm for 40 s.
4. Pre-bake at 90 ^{0}C for 20 min.
5. Align and expose[5] for 13 s (mask HIRA 991).
6. Develop for 40 s, rinse, blow dry.
7. Post-bake for 30 min at 120^{0}C.

Chemical etching to define Hall bar

1. Make lactic-acid based etchant (see next page).
2. Etch for 1.5 min (~3 μm).
3. Measure etch depth plus resist thickness with Tencor.
4. Strip resist with acetone.
5. Measure etch depth with Tencor.

Second level of lithography to define contact pads

1. Bake at 120^{0}C for 5 min.

---

[4] Spin Coater 1H-DX, Mikasa spinner.
[5] Mask exposer, Nikon 82210

2. Spin on AZ 37 photoresist at 500 rpm for 3 s and 4000 rpm for 40 s.
3. Pre-bake at 90^0C for 20 min.
4. Align and expose for 25 s.
5. Develop for 40 s.
6. Repeat steps 4 and 5, if residual photoresist remains (10 s exposure, 15 s develop).

Evaporate[6] contacts (either Indium or AuGeNi)

Electron beam lithography and Reactive Ion Etching (to define four-terminal structures on Hall bar)

Anneal[7] contacts

The In contacts are annealed at 225^0C for 5 min in H_2 (20%) / N_2 (80%) forming gas. The AuGeNi (0.8:0.1:0.1) contacts do not require annealing.

Etchant for InSb / AlInSb

1. Add 3 ml of 30% H_2O_2 to 27 ml of H_2O, then save 18 ml of the mixture.
2. Add 3 ml of lactic acid to the 18 ml of the H_2O_2 /H_2O mixture.
3. Add 3 ml of 50% HF to 57 ml of H_2O, then save 9 ml of this mixture.
4. Add the 9 ml of the HF/ H_2O mixture to the 21 ml of the lactic acid / H_2O_2 /H_2O mixture.

The composition of the final mixture is 3% H_2O_2, 2.5% HF, 85% lactic acid in the proportion 6:3:1. The etch rate is approximately 2 μm/min.

---

[6] EM-500T vacuum evaporator
[7] ULVAC SINKU-RIKO infrared image furnace, thermal program controller HPC-7000.

Appendix 4

LIST OF PUBLICATIONS

[1] "Observation of spin-mediated subband Landau-level coupling in a two-dimensional electron gas", X.H. Zhang, R.C. Meyer, T. Kasturiarachchi, **N. Goel**, R.E. Doezema, S.J. Chung and M.B. Santos and Y-J. Wang, submitted to Phys. Rev. Lett.

[2] "Spin polarized and ballistic transport in InSb/InAlSb heterostructures", H. Chen, J.A. Peters, J.J. Heremans", **N. Goel**, S.J. Chung and M.B. Santos, submitted to Proceedings of the 27th ICPS (2004).

[3] "Quantum Hall ferromagnetism in InSb heterostructures", J.C. Chokomakoua, **N. Goel**, S.J. Chung, M.B. Santos, M.B. Johnson and S. Q. Murphy, submitted to Proceedings of the 27th ICPS (2004).

[4] "Spin-flip subband-Landau-level coupling in InSb heterostructures", X.H. Zhang, R.C. Meyer, T. Kasturiarachchi, **N. Goel**, R. Doezema, S.J. Chung, M.B. Santos and Y-J. Wang, submitted to Proceedings of the 27th ICPS (2004).

[5] "Ballistic transport in InSb mesoscopic structures", **N. Goel**, K. Suzuki, S. Miyashita, S.J. Chung, M.B. Santos and Y. Hirayama, accepted Physica E.

[6] "Ballistic transport in InSb/AlInSb antidot lattices", H. Chen, J.J. Heremans, J.A. Peters, **N. Goel**, S.J. Chung and M.B. Santos, Appl. Phys. Lett. 84, 5380 (2004).

[7] "Ising quantum Hall ferromagnetism in InSb based two dimensional electronic systems", J.C. Chokomakoua, **N. Goel**, S.J. Chung, M.B. Santos, J.L. Hicks, M.B Johnson and S.Q. Murphy, Phys. Rev. B 69, 235315 (2004).

[8] "Spin-Polarized reflection of electrons in a two-dimensional electron system", H. Chen, J.J. Heremans, J.A. Peters, J.P. Dulka, A.V. Govorov, S.J. Chung, **N. Goel** and M.B. Santos, submitted to Appl. Phys. Lett.

[9] "Effect of temperature on ballistic transport in InSb quantum wells", **N. Goel**, S.J. Chung, M.B. Santos, K. Suzuki, S. Miyashita and Y. Hirayama, Physica E 21, 2-4, 761 (2004).

[10] "Structural defects in $Al_xIn_{1-x}Sb$/InSb quantum wells grown on GaAs (001) substrates", T.D. Mishima, J.C. Keay, **N. Goel**, M.A. Ball, S.J. Chung, M.B. Johnson and M.B. Santos, Physica E 21, 2-4, 770 (2004).

[11] "Ballistic transport in InSb quantum wells at high temperature", **N. Goel**, S.J. Chung, M.B. Santos, K. Suzuki, S. Miyashita, Y. Hirayama, Physica E 20, 3-4, 251 (2004).

[12] "Spin effects in InSb quantum wells", G.A. Khodaparast, R.C. Meyer, X.H. Zhang, T. Kasturiarachchi, R.E. Doezema, S.J. Chung, **N. Goel**, and M. B. Santos and Y.J. Wang, Physica E 20, 3-4, 386 (2004).

[13] "Effect of structural defects in InSb/$Al_xIn_{1-x}Sb$ quantum wells grown on GaAs (001) substrates", T.D. Mishima, J.C. Keay, **N. Goel**, M.A. Ball, S.J. Chung, M.B. Johnson and M.B. Santos, Physica E 20, 3-4, 260 (2004).

[14] "Anisotropic structural and electronic properties of InSb/$Al_xIn_{1-x}Sb$ quantum wells grown on GaAs (001) substrates", T.D. Mishima, J.C. Keay, **N. Goel**, M.B. Johnson and M.B. Santos, J. Cryst. Growth 251, 551 (2003).

[15] "Nonmagnetic semiconductors as read-head sensors for ultra-high density magnetic recording", S.A. Solin, D.R. Hines, A.C.H. Rowe, D.S. Tsai, Y.A. Pashkin, S.J. Chung, **N. Goel** and M.B. Santos, Appl. Phys. Lett. 80, 4012 (2002).

[16] "Room temperature extraordinary magnetoresistance of non-magnetic narrow gap semiconductor/metal composites: Applications to read-head sensors for ultra-high density magnetic recording", S.A. Solin, D.R. Hines, D.S. Tsai, Y.A. Pashkin, S.J. Chung, **N. Goel** and M.B. Santos, IEEE Trans. on Magnetics 38, 89 (2002).

BIBLIOGRAPHY

[1] Ashcroft and Mermin, Solid State Physics, College Edition (1976).

[2] L.J. van der Pauw, Phil. Tech. Rev. 13, 1 (1958).

[3] J. Heremans, J. Phys. D: Appl. Phys. 26, 1149 (1993); J. Heremans, D.L. Partin, C.M. Thrush and L. Green, Semicond. Sci. Technol. 8, 424 (1993).

[4] S.A. Solin, T. Thio, D.R. Hines and J.J. Heremans, Science 289, 1530 (2000).

[5] C. Kittel, Introduction to Solid State Physics, John Wiley and Sons, (1968).

[6] J. Davies, The Physics of Low Dimensional Semiconductors, Cambridge University Press (1998).

[7] E.O. Kane, J. Phys. Chem. Solids 1, 249 (1957).

[8] W.A. Beck and J.R. Anderson, J. Appl. Phys. 62, 541 (1987).

[9] Z. Dziuba and M. Górska, J. Phys. III France 2, 99 (1992).

[10] J. Antoszewski, D.J. Seymour, L. Faraone, J.R. Meyer and C.A. Hoffman, J. Elect. Mater. 24, 1255 (1995).

[11] J.R. Meyer, C.A. Hoffman, J. Antoszewski, L. Faraone, J. Appl. Phys. 81, 709 (1997).

[12] T.D. Mishima and M.B. Santos, J. Vac. Sci. Technol. B 22, 1472 (2004).

[13] A.G. de Oliveira, S.D. Parker, R. Droopad, B.A. Joyce, Surf. Sci. 227, 150 (1990).

[14] W.K. Liu and M.B. Santos, Surface Sci. 319, 172 (1994).

[15] S.A. Solin, D.R. Hines, A.C.H. Rowe, J.S. Tsai, Yu.A. Pashkin, S.J. Chung, N. Goel and M.B. Santos, Appl. Phys. Lett. 80, 4012 (2002).

[16] G.A. Khodaparast, R.E. Doezema, S.J. Chung, K.J. Goldammer and M.B. Santos, IPAP Conf. Series 2, 245 (2001); G.A. Khodaparast, R.C. Meyer, X.H. Zhang, T.D. Kasturiarachi, R.E. Doezema, S.J. Chung, N. Goel and M.B. Santos, Physica E 20, 386 (2004).

[17] N. Goel, S.J. Chung, M.B. Santos, K. Suzuki, S. Miyashita and Y. Hirayama, Bull. Am. Phys. Soc. 47, 269 (2002); Physica E 20, 251 (2004).

[18] For a discussion of the layer structure, S.J. Chung, K.J. Goldammer, S.C. Lindstrom, M.B. Johnson and M.B. Santos, J. Vac. Sci. Technol. B 17, 1151 (1999).

[19] W.K. Liu, K.J. Goldammer and M.B. Santos, J. Appl. Phys. 84, 205 (1998).

[20] Critical thicknesses were calculated using the criteria discussed in J.W. Matthews and A.E. Blakeslee, J. Cryst. Growth 27, 118 (1974).

[21] W.K. Liu, Xuemei Zhang, Weiluan Ma, J. Winesett and M.B. Santos, J. Vac. Sci. Technol. B 14, 2339 (1996).

[22] M.A. Ball, J.C. Keay, S.J. Chung, M.B. Santos and M.B. Johnson, Appl. Phys. Lett. 80, 2138 (2002).

[23] S.J. Chung, M.A. Ball, S.C. Lindstrom, M.B. Johnson and M.B. Santos, J. Vac. Sci. Technol. B 18, 1583 (2000).

[24] T.D. Mishima, J.C. Keay, N. Goel, M.A. Ball, S.J. Chung, M.B. Johnson and M.B. Santos, J. Cryst. Growth 251, 551 (2003).

[25] T.D. Mishima, J.C. Keay, N. Goel, M.A. Ball, S.J. Chung, M.B. Johnson and M.B. Santos, Physica E 20, 260 (2004).

[26] P. Humble, Phys. Stat. Sol. 30, 183 (1968).

[27] T. Schweizer, K. Köher, W. Rothemund and P. Ganser, Appl. Phys. Lett. 59, 2736 (1991).

[28] Y. Tokura, T. Saku and Y. Horikoshi, Phys. Rev. B 53, R10528 (1996).

[29] Y. Tokura, T. Saku, S. Tarucha and Y. Horikoshi, Phys. Rev. B 46, 15558 (1992).

[30] S. Datta and B. Das, Appl. Phys. Lett. 56, 665 (1990).

[31] J.M. Kikkawa and D.D. Awschalom, Phys. Rev. Lett. 80, 4313 (1998).

[32] D. Hagele, M. Oestreich, W.W. Rühle, N. Nestle and K. Eberl, Appl. Phys. Lett. 73, 1580 (1990).

[33] Y. Takagaki, K. Gamo, S. Namba, S. Takaoka, K. Murase and S. Ishida, Solid State Commun. 71, 809 (1989).

[34] T.J. Thornton, S. Yamada, M. Yamamoto and K. Aihara, Electron. Lett. 27, 1177 (1991).

[35] Y. Hirayama and S. Tarucha, Appl. Phys. Lett. 63, 2366 (1993).

[36] M.L. Roukes, A. Scherer, S.J. Allen, Jr., H.G Craighead, R.M. Ruthen, E.D. Beebe and J.P. Harbison, Phys. Rev. Lett. 59, 3011 (1987).

[37] C.J.B. Ford, S. Washburn, M. Büttiker, C.M. Knoedler and J.M. Hong, Phys. Rev. Lett. 62, 2724 (1989).

[38] G. Timp, A.M. Chang, P. Mankiewich, R. Behringer, J.E. Cunningham, T.Y. Chang and R.E. Howard, Phys. Rev. Lett. 59, 732 (1987).

[39] C.J.B. Ford, T.J. Thornton, R. Newbury, M. Pepper, H. Ahmed, D.C. Peacock, D.A. Ritchie, J.E.F. Frost and G.A.C. Jones, Phys. Rev. B 38, 8518 (1988).

[40] Y. Takagaki, Solid State Commun. 68, 1051 (1988).

[41] G. Timp, H.U. Baranger, P. deVegvar, J.E. Cunningham, R.E. Howard, R. Behringer and M. Mankiewich, Phys. Rev. Lett. 60, 2081 (1988).

[42] "Solid State Physics: Semiconductor Heterostructures and Nanostructures", ed. H. Ehrenreich and D. Turnbull, vol. 44, Academic Press 1991.

[43] C.W.J. Beenakker and H. van Houten, Phys. Rev. B 39, 10445 (1989).

[44] C.W.J. Beenakker and H. van Houten, Phys. Rev. Lett. 63, 1857 (1989).

[45] G. Kirczenow, Solid State Comm. 71, 469 (1989).

[46] H. Akera and T. Ando, Phys. Rev. B 41, 11967 (1990).

[47] G.L. Snider, M.S. Miller, M.J. Rooks and E.L. Hu, Appl. Phys. Lett. 59, 2727 (1991).

[48] M. Büttiker, Phys. Rev. Lett. 57, 1761 (1986).

[49] Y. Takagaki, T. Sakamoto, K. Gamo, S. Namba, S. Takaoka and K. Murase, Superlatt. Microstruct. 8, 97 (1990).

[50] T. Saku, Y. Hirayama and Y. Horikoshi, Jpn. J. Appl. Phys. 30, 902 (1991).

[51] Y. Hirayama, T. Saku, S. Tarucha, Y. Horikoshi, Appl. Phys. Lett. 58, 2672 (1991).

[52] S. Tarucha, T. Saku, Y. Hirayama and Y. Horikoshi, Phys. Rev. B 45, 13465 (1992).

[53] N. Goel S.J. Chung, M.B. Santos, K. Suzuki, S. Miyashita and Y. Hirayama, Physica E 21, 761 (2004).

[54] B.J. van Wees, H. van Houten, C.W.J. Beenaker, J.G. Williamson, L.P. Kouwenhoven, D. van der Marel and C.T. Foxon, Phys. Rev. Lett. 60, 848 (1988).

[55] D.A. Wharam, T.J. Thornton, R. Newbury, M. Pepper, H. Ahmed, J.E.F. Frost, D.G. Hasko, D.C. Peacock, D.A. Ritchie and G.A.C. Jones, J. Phys. C 21, L209 (1988).

[56] T. Bever, Y. Hirayama and S. Tarucha, Jpn. J. App. Phys. Part 2, 33, L800 (1994).

[57] J.-O. Wesström, K. Hieke, B. Stalnacke, Th. Palm and B. Stoltz, App. Phys. Lett. 70, 1302 (1997).

[58] M.F. Tietze, Th. Schäpers, J. Appenzeller, G. Engels, M. Hollfelder, B. Lengeler and H. Luth, J. App. Phys. 79, 871 (1996).

[59] S.J. Koester, C.R. Bolognesi, E.L. Hu, H. Kroemer, M.J. Rooks and G.L. Snider, J. Vac. Sci. Technol. B 11, 2528 (1993).

[60] S.J. Koester, C.R. Bolognesi, M.J. Rooks, E.L. Hu and H. Kroemer, Appl. Phys. Lett. 62, 1373 (1993).

[61] D. Többen, D.A. Wharam, G. Abstreiter, J.P. Kotthaus and F. Schäfler, Semicond. Sci. Technol. 711, 10 (1995).

[62] G. Grabecki, J. Wróbel, T. Dieh, K. Byczuk, E. Papis, E. Kaminska, A. Piotrowska, G. Springholz, M. Pinczolits and G. Bauer, Phys. Rev. B 60, R5133 (1999).

[63] N.J. Curson, R. Nemutudi, N.J. Appleyard, M. Pepper, D.A. Ritchie and G.A.C. Jones, App. Phys. Lett. 78, 3466 (2001).

[64] J. Regul, U.F. Keyser, F. Hobb, U. Zeitla, R.J. Haug, A. Malave, E. Oesterschulze, D. Reuter and A.D. Wieck, App. Phys. Lett. 75, 1107 (1999).

[65] S.J. Koester, C.R. Bolognesi, M. Thomas, E.L. Hu, H. Kroemer and M.J. Rooks, Phys. Rev. B 50, 5710 (1994).

[66] C.W.J. Beenakker, H. van Houten and B.J. van Wees, Superlatt. and Microstruct. 5, 127 (1989).

[67] K.F. Berggren and D.J. Newson, Semicond. Sci. Technol. 1, 327 (1986).

[68] A.S. Plaut, H. Large, P. Grambow, D. Heitmann, K. von Klitzing and K. Ploog, Phy. Rev. Lett. 67, 1642 (1991).

[69] K.F. Bergrenn, T.J. Thornton, D.J. Newson and M. Pepper, Phys. Rev. Lett. 57, 1769 (1986).

[70] Q.P. Li and Sarma S. Das, Phys, Rev. B 44, 6277 (1991).

[71] T. Ando, A.B. Fowler and F. Stern, Rev. Mod. Phys. 54, 437 (1982).

[72] R.J. Nicholas, R.J. Haug, K. von Klitzing and G. Weimann, Phys. Rev. B 37, 1294 (1988).

[73] N.K. Patel, J.T. Nicholls, L. Martín-Moreno, M. Pepper, J.E.F. Frost, D.A. Ritchie and G.A.C. Jones, Phys. Rev. B 44, 10973 (1991).

[74] N.K. Patel, J.T. Nicholls, L. Martín-Moreno, M. Pepper, J.E.F. Frost, D.A. Ritchie and G.A.C. Jones, Phys. Rev. B 44, 13549 (1991).

[75] K.J. Thomas, J.T. Nicholls, N.J. Appleyard, M.Y. Simmons, M. Pepper, D.R. Mace, W.R. Tribe and D.A. Ritchie, Phys. Rev. B 58, 4846 (1998).

[76] K.J. Thomas, J.T. Nicholls, M.Y. Simmons, M. Pepper, D.R. Mace and D.A. Ritchie, Phys. Rev. Lett. 77, 135 (1996).

[77] A. Kristensen, P.E. Lindelof, J.B. Jensen, M. Zaffalon, J. Hollingbery, S.W. Pedersen, J. Nygård, H. Bruus, S.M. Reimann, C.B. Sørensen, M. Michel and A. Forchel, Physica B 251, 180 (1998).

[78] D.J. Reilly, G.R. Facer, A.S. Dzurak, B.E. Kane, R.G. Clark, P.J. Stiles, R.G. Clark, A.R. Hamilton, J.L. O'Brien, N.E. Lumpkin, L.N. Pfeiffer and K.W. West, Phys. Rev. B 63, 121311 (2001).

[79] N.T. Bagraev, A.D. Buravlev, L.E. Klyachkin, A.M. Malyarenko, W. Gehlhoff, V.K. Ivanov and I.A. Shelykh, Semicond. 36, 439 (2002).

[80] K.J. Thomas, J.T. Nicholls, M. Pepper, W.R. Tribe, M.Y. Simmons and D.A. Ritchie, Phys. Rev. B 61, R13365 (2000).

[81] C.-K. Wang and K.-F. Berggren, Phys. Rev. B 54, 14257 (1996).

[82] K.J. Thomas, J.T. Nicholls, M. Pepper, M.Y. Simmons, D.R. Mace and D.A. Ritchie, Physica E 12, 708 (2002).

[83] A. Kristensen, H. Bruus, A. Forchel, J.B. Jensen, P.E. Lindelof, M. Michel, J. Nygard and C.B. Sørensen, Proc. ICPS24 Jerusamlem, Aug 2-7 (1998).

[84] B. Spivak and F. Zhou, Phys. Rev. B 61, 16730 (2000).

[85] H. Bruus, V.V. Cheianov and K. Flensberg, Physica E 10, 97 (2001).

[86] A.A. Starikov, I.I. Yakimenko and K.-F. Berggren, Phys. Rev. B 67 235319 (2003).

[87] S.M. Reimann, M. Koshinen and M. Manninen, Phys. Rev. B 59, 1613 (1999).

[88] V.V. Flambaum and M.Y. Kuchiev, Phys. Rev. B 61, 7869 (2000).

[89] T. Rejec, A. Ramsak and J.H. Jefferson, Phys. Rev. B 62, 12985 (2000).

[90] Y. Meir, K. Hirose and N.S. Wingreen, Phys. Rev. Lett. 89, 196802 (2002).

[91] S.M. Cronenwett, H.J. Lynch, D. Goldhaber-Gordon, L.P. Kouwenhoven, C.M Marcus, K. Hirose, N.S. Wingreen and V. Umansky, Phys. Rev. Lett. 88, 226805 (2002).

[92] G. Seelig and K.A Matveev, Phys. Rev. Lett. 90, 176804 (2003).

[93] A.C. Graham, K.J. Thomas, M. Pepper, N.R. Cooper, M.Y. Simmons and D.A. Ritchie, Phys. Rev. Lett. 91, 136404 (2003).

[94] R.E. Jones Jr., C. Dennis Mee and C. Tsang, in Magnetic Recording Technology, 2nd edition, Ed. by C. Dennis Mee Eric D. Daniel, (McGraw-Hill, New York, 1996) pp. 6.1 – 6.102.

[95] IBM Techfax #7107, http://www.storage.ibm.com/hdd/micro/datasheet.pdf.

[96] P.M. Levy, Solid State Phys. 47, 367 (1994).

[97] J.S. Moodera, L.R. Kinder, T.M.Wong and R. Meservey, Phys Rev. Lett. 74, 3273 (1995).

[98] N. Smith and P. Arnett, Appl. Phys. Lett. 78, 1448 (2001).

[99] Collateral improvements in recording media and write heads will also be required in order to achieve such high areal densities.

[100] S. Lamari, J. Appl. Phys. 91, 1698 (2002).

[101] R.S. Popovic, "Hall Effect Devices", Bristol, U.K.: Adam Hilger, 1991, pp. 137-142.

[102] T. Zhou, D.R. Hines and S.A. Solin, Appl. Phys. Lett., 78, 667 (2001).

[103] S.A. Solin, T. Thio, D.R. Hines, T. Zhou and J.J. Heremans, presented at the Proc. 25th Int. Conf. Physics of Semiconductors, Osaka, Japan, Sept. 2000.

[104] M. Sugawara, "Plasma Etching", NewYork; Oxford Univ. Press, pp 69-98 (1998).

[105] S.A. Solin, D.R. Hines, A.C.H. Rowe, J.S. Tsai and Yu A. Pashkin, J. Vac. Sci. Technol. B 21, 3002 (2003).

[106] Y. Nakamura, C.D. Chen and J.S. Tsai, Jpn. J. Appl. Phys. 35, L1465 (1996).

[107] S.A. Solin, D.R. Hines, J.S. Tsai, Yu A. Pashkin, S.J. Chung, N. Goel and M.B. Santos, Appl. Phys. Lett. 80, 4012 (2002).

[108] H. N. Bertram, "Theory of Magnetic Recording", Cambridge, U.K.: Cambridge Univ. Press, pp 169-171 (1994).

[109] "Thermal magnetization fluctuations in GMR heads", in Proceedings of the Magnetic Recording Conf. B. Gurney, Ed., Minneapolis, MN (2001).

[110] M.F. Hoyaux, Solid State Plasmas. London, U.K.: Pion Ltd., pp. 102-107 (1970).

[111] N. Dai, F. Brown, R.E. Doezema, S.J. Chung, K.J. Goldammer and M.B. Santos, Appl. Phys. Lett. 73, 3132 (1998).

[112] N. Dai, G.A. Khodaparast, F. Brown, R.E. Doezema, S.J. Chung and M.B. Santos, Appl. Phys. Lett. 76, 3905 (2000).

[113] A. Därr, J.P. Kotthaus and T. Ando, "Physics of Semiconductors", ed. F.G. Fumi (North-Holland, Amsterdam, 1976), pp. 774-777; A. Därr, doctoral dissertation, Technische Universitt Munchen, 1978 (unpublished).

[114] Y.-F Chen, M. Dobrowolska, J. K. Furdyna and S. Rodriguez, Phys. Rev. B 32, 890 (1985).

[115] Y.-F Chen, M. Dobrowolska and J. K. Furdyna, Phys. Rev. B 31, 7989 (1985).

[116] Sudha Gopalan, J. K. Furdyna and S. Rodriguez, Phys. Rev. B 32, 903 (1985).

[117] J. Scriba, A. Wixforth, J.P. Kotthaus, C.R. Bolognesi, C. Nguyen, G. Tuttle, J.H. English and H. Kroemer, Semicond. Sci. Technol. 8, S133 (1993).

[118] M.J. Yang, R.J. Wagner, B.V. Shanabrook, J.R. Waterman and W.J. Moore, Phys. Rev. B 47, 6807 (1992).

[119] C. R. Pidgeon and R. N. Brown, Phys. Rev. 146, 575 (1966).

[120] Z. Schlesinger, J.C.M. Hwang and S.J. Allen, Jr., Phys. Rev. Lett. 50**,** 2098 (1983).

[T121] X.H. Zhang, R.C. Meyer, T. Kasturiarachchi, N. Goel, R.E. Doezema, S.J. Chung, M.B. Santos and Y-J. Wang, submitted to Phys. Rev. Lett.

[122] Y.A. Bychkov and E.I. Rashba, J. Phys. C 17, 6039 (1984); Y.A. Bychkov and E. E. Rashba, Pis'ma Zh. Eksp. Teor. Fiz. 39, 66 (1984) [JETP Lett. 39, 78 (1984)].

[123] See, for example, Th. Schôapers, G. Engels, J. Lange, Th. Klocke, M. Hollfelder and H. Lüth, J. Appl. Phys. 83, 4324 (1998), and references therein.

[124] B. Jusserand, D. Richards, H. Peric and B. Etienne, Phys. Rev. Lett. 69, 848 (1992); B. Jusserand, D. Richards, G. Allan, C. Priester and B. Etienne, Phys. Rev. B 51, 4707 (1995).

[125] Landolt-Börnstein, "Numerical Data and Functional Relationships in Science and Technology", (O. Madelung, ed.), Group III, vol. 22 (Springer-Verlag Berlin) 1987.

[126] M. Dobers, K. v. Klitzing and G. Weimann, Phys. Rev. B 38, 5453 (1988).

[127] R. Meisels, I. Kulac, F. Kuchar and M. Kriechbaum, Phys. Rev. B 61, 5637 (2000).

[128] D. Grundler, Phys. Rev. Lett. 84, 6074 (2000).

[129] P. Pfeffer and W. Zawadzki, J. Supercond. 16, 351 (2003).

[130] P.O. Hansson, F. Ernst and E. Bauer, J. Appl. Phys. 72, 2083 (1992).

[131] H. Yamaguchi, M.R. Fahy and B.A. Joyce, Appl. Phys Lett. 69, 776 (1996).

[132] H. Yamaguchi and Y. Hirayama, Jpn. J. Appl. Phys. Part 1 37, 1599 (1998).

[133] D.L. Smith, Solid State Commun. 57, 919 (1986).

[134] E.A. Caridi, T.Y. Chang, K.W. Goossen and L.F. Eastman, Appl. Phys. Lett. 56, 660 (1990).

[135] T. Hayakawa, M. Kondo, T. Suyama, K. Takahashi, S. Yamamoto and T. Hijikata, Jpn. J. Appl. Phys. 26, L302 (1987).

[136] M.R. Fahy, K. Sato and B.A. Joyce, Appl. Phys. Lett. 64, 190 (1994).

[137] B.J. Garcia, C. Fontaine and A. Muñoz-Yagüe, Appl. Phys. Lett. 66, 610 (1995).

[138] A.Y. Cho, M.B. Panish and I. Hayashi, Proceedings of the Third International Symposium on GaAs and Related Compounds, Ed. K. Paulus, Institute of Physics, London 1970.

[139] A.Y. Cho, J. Appl. Phys. 41, 2780 (1970).

[140] P. Chen, K.C. Rajkumar and A. Madhukar, J. Vac. Sci. Technol. B 9, 2312 (1991).

[141] D.A. Woolf, Z. Sobiesierski, D.I. Westwood and R.H. Williams, J. Appl. Phys. 71, 4908 (1992).

[142] D.K. Biegelsen, R.D. Bringans, J.E. Northrup and L.-E. Swartz, Phys. Rev. Lett. 65, 452 (1990).

[143] E. Kaxiras, K.C. Pandey, Y. Bar-Yam and J.D. Joannopoulos, Phys. Rev. Lett. 56, 2819 (1986).

[144] K. Kanisawa, H. Yamaguchi and Y. Hirayama, Appl. Phys. Lett. 76, 589 (2000).

[145] W.I. Wang, E.E. Mendez, T.S. Kaun and L. Esaki, Appl. Phys. Lett. 47, 826 (1985).

[146] N. Goel, S.J. Chung and M.B. Santos, Bull. Am. Phys. Soc. 46, 1188 (2001).

[147] J.C. Keay, N. Goel, S.J. Chung, M.B. Santos and M.B. Johnson, Bull. Am. Phys. Soc. 46, 1188 (2001).